

**TRANSIENT TEMPERATURE DISTRIBUTION AND THERMO-  
ELASTIC STRESS IN GUN TUBES**

by

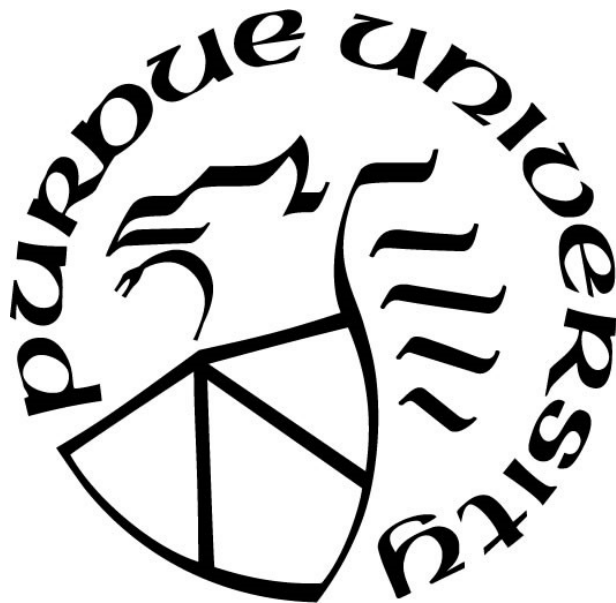
Alexander Robert Cooper

**A Thesis**

*Submitted to the Faculty of Purdue University*

*In Partial Fulfillment of the Requirements for the degree of*

**Master of Science in Engineering**



Department of Civil and Mechanical Engineering

Fort Wayne, Indiana

May 2023

**THE PURDUE UNIVERSITY GRADUATE SCHOOL**  
**STATEMENT OF COMMITTEE APPROVAL**

**Dr. Donald Mueller**

Department of Civil and Mechanical Engineering

**Dr. Hosni Abu-Mulaweh**

Department of Civil and Mechanical Engineering

**Dr. Zhuming Bi**

Department of Civil and Mechanical Engineering

**Approved by:**

Dr. Hosni Abu-Mulaweh

*In dedication to my family, friends, professors, and coworkers.*

## **ACKNOWLEDGEMENTS**

I would like to acknowledge Dr. Donald Mueller, Dr. Hosni Abu-Mulaweh, and Dr. Zhuming Bi for their assistance and patience in the completion of this thesis. I would like to thank my grandparents, family, and friends for their support and encouragement. Further thanks to Ohio Ordnance Works for the software and facilities used for this thesis.

# TABLE OF CONTENTS

LIST OF FIGURES .....	8
LIST OF TABLES .....	11
NOMENCLATURE .....	12
SUBSCRIPTS .....	15
ABSTRACT.....	17
1 INTRODUCTION .....	18
1.1 Background .....	18
1.1.1 Regions of a Gun Tube .....	18
1.1.2 Functional Requirements of a Gun Tube .....	20
1.1.3 Firing Phenomena .....	21
1.2 The M16, M4 Carbine, and AR-15 Family of Weapons.....	27
1.2.1 Barrel Overheating.....	27
1.3 Thesis Organization.....	31
1.3.1 Chapter 1: Introduction .....	31
1.3.2 Chapter 2: Modeling and Simulation Method .....	32
1.3.3 Chapter 3: Experiment Apparatus and Procedure.....	34
1.3.4 Chapter 4: Simulation Results .....	34
1.3.5 Chapter 5: Conclusion.....	35
1.3.6 Chapter 6: Recommendations .....	35
2 MODELING AND SIMULATION METHOD.....	36
2.1 Basic Assumptions .....	36
2.2 Model Development for use in ANSYS.....	36
2.2.1 Barrel Geometry.....	36
2.2.2 Determination of Propellant and Ballistic Parameters.....	40
2.2.3 Transient and Axial Discretization .....	44
2.2.4 Calculation of Internal and External Heat Transfer Coefficients .....	45
2.2.5 Specification of Firing Schedule, Initial Barrel Temperature, and Ambient Conditions .....	48
2.2.6 Barrel Geometry Implementation in ANSYS .....	49
2.2.7 Application of Governing Equations in ANSYS .....	51

3	EXPERIMENT APPARATUS AND PROCEDURE .....	58
3.1	Apparatus and Procedure .....	59
3.1.1	Apparatus .....	59
3.1.2	Procedure .....	60
3.2	Experiments.....	61
3.2.1	Measurement and Data Collection.....	61
3.2.2	Experiment 1 .....	62
3.2.3	Experiment 2.....	63
3.2.4	Experiment 3.....	65
3.2.5	Experiment 4.....	67
3.3	Data Reduction and Sample Results .....	68
3.3.1	Data Reduction.....	68
3.3.2	Sample Results.....	68
3.4	Repeatability.....	70
4	SIMULATION RESULTS .....	72
4.1	Verification.....	72
4.1.1	Mesh Independence and Simulation Stability.....	72
4.1.2	Heat Transfer Coefficient Sensitivity .....	76
4.1.3	Transient Thermal Analysis Verification.....	79
4.1.4	Static Structural Analysis Verification .....	82
4.2	Validation.....	85
4.2.1	Validation of Temperature Distribution.....	85
4.2.2	Validation of Thermo-elastic Stress.....	89
4.3	Effects of Firing Schedule Parameters on Gun Tube Temperatures.....	94
4.3.1	Cyclic Rate of Fire .....	94
4.3.2	Cooling Time Between Bursts .....	96
5	CONCLUSION.....	99
6	RECOMMENDATIONS.....	101
	LIST OF REFERENCES.....	102
	APPENDIX A. DETERMINATION OF THE POWDER, AND SIMULATION OF THE PRESSURE AND VELOCITY CURVES OF THE PROJECTILE .....	105
	APPENDIX B. DETERMINATION OF PROPELLANT COMPOSITION AND COMBUSTION PRODUCTS .....	107

APPENDIX C. SPECIFICATION OF MATERIAL PROPERTIES ..... 112  
APPENDIX D. EXTERNAL AND INTERNAL HEAT TRANSFER COEFFICIENTS ..... 115  
APPENDIX E. DRAWINGS OF BARREL ACCESSORIES ..... 120  
APPENDIX F. DATA FROM EXPERIMENTS PERFORMED BY JEFF WINDHAM ..... 121  
APPENDIX G. THERMAL CAMERA DATA ..... 127  
APPENDIX H. VERIFICATION RESULTS..... 134  
APPENDIX I. 30 AND 60 ROUND VALIDATION..... 138  
APPENDIX J. EFFECTS OF COOLING TIME BETWEEN BURSTS RESULTS ..... 161

## LIST OF FIGURES

Figure 1.1: Typical Gun Tube Regions.....	19
Figure 1.2: Boundary layer thickness and internal heat transfer coefficient (Shelton, et al., pg.103).....	23
Figure 1.3: Bore erosion in the gun tube of an AR-15 rifle.....	26
Figure 1.4: M4 carbine, no handguards, external barrel temperature (Windham, 1994, pg. 13). 29	
Figure 1.5: Axial temperature profile of the M4 carbine barrel (Windham, 1994, pg. 18). .....	29
Figure 1.6: M4 carbine, fire to destruction test #1, external barrel temperature (Windham, 1996, pg. 20).....	30
Figure 1.7: M4 carbine, fire to destruction test #2, external barrel temperature (Windham, 1996, pg. 26).....	31
Figure 1.8: Simulation flow chart. ....	32
Figure 2.1: Example medium profile barrel geometry used simulations.....	37
Figure 2.2: AR-15 Barrel Profile. ....	38
Figure 2.3: M4A1 Profile Barrel.....	39
Figure 2.4: QuickLOAD Quickstart interface. ....	40
Figure 2.5: Pressure – velocity vs barrel length curves for 5.56 x 45 mm. ....	41
Figure 2.6: Pressure – velocity vs time curves for 5.56 x 45 mm.....	41
Figure 2.7: Mean gas pressure and temperature curves.....	43
Figure 2.8: Maximum pressure and temperature at respective barrel lengths for all times.....	44
Figure 2.9: Analysis setup in ANSYS Workbench.....	49
Figure 2.10: Mesh details.....	50
Figure 2.11: Generated axial and radial mesh distribution. ....	50
Figure 2.12:ANSYS Workbench transient thermal analysis. ....	51
Figure 2.13: Transient thermal analysis setup. ....	51
Figure 2.14: Analysis Settings and Time Steps. ....	52
Figure 2.15: External convection and radiation boundary condition.....	52
Figure 2.16: Barrel with internal and sectioning boundary conditions applied. ....	53
Figure 2.17: Transient Thermal Analysis simulation loads.....	53

Figure 2.18: Various Boundary Condition Settings.....	54
Figure 2.19: Workbench setup for coupling Transient Thermal and Static Structural Analysis..	54
Figure 2.20: Analysis settings and imported body temperature interface. ....	55
Figure 2.21: Static Structural Analysis loads and boundary conditions. ....	55
Figure 2.22: Applied loads and boundaries for Static Structural Analysis.....	56
Figure 2.23: Static Structural loads and boundaries applied to barrel geometry. ....	56
Figure 2.24: Static Structural Analysis solutions tab.....	57
Figure 2.25: User defined material strength function. ....	57
Figure 3.1: Experiment apparatus. ....	60
Figure 3.2: Input parameters for the FLIR E8-XT thermal camera.....	61
Figure 3.3: Barrel type 1 used in experiment 1.....	62
Figure 3.4: Barrel type 2 used in experiments 2 – 4. ....	62
Figure 3.5: Experiment #1, first shot. ....	63
Figure 3.6: Experiment #1, external barrel temperature at 19.605 seconds. ....	63
Figure 3.7: Experiment #2 Error, weapon laid on its side during cooling.....	64
Figure 3.8: Experiment #2, weapon orientation corrected.....	65
Figure 3.9: Experiment #3 error, thermal camera set to incorrect temperature range. ....	66
Figure 3.10: Experiment #4, thermal camera set to correct temperature range.....	66
Figure 3.11: Experiment #4, first shot. ....	67
Figure 3.12: Experiment #4, external barrel temperature at 30.173 seconds. ....	68
Figure 3.13: Axial Temperature Distribution at 10, 20, and 30 Rounds Fired for Barrel Type 1.	69
Figure 3.14: Axial Temperature Distribution at 15 and 45 Rounds Fired for Barrel Type 2. ....	69
Figure 3.15: Axial Temperature Distribution at 30 and 60 Rounds Fired for Barrel Type 2. ....	70
Figure 3.16: Sample results for temperature vs cartridges fired.....	71
Figure 3.17: Experiment standard deviations. ....	71
Figure 4.1: ANSYS Failure to Converge Warning.....	72
Figure 4.2: Percent change from 200 time-steps per shot.....	75
Figure 4.3: Percent change from 200 time-steps per shot.....	75
Figure 4.4: Relationship between relative change in temperature and relative change in internal heat transfer coefficient. ....	77

Figure 4.5: Verification of ANSYS Transient Thermal Analysis.....	81
Figure 4.6: ANSYS Workbench setup for thermo-elastic stress verification.....	82
Figure 4.7: Boundary conditions for transient thermal portion of thermo-elastic stress verification.....	83
Figure 4.8: Mechanical boundary conditions for thermo-elastic stress verification.....	83
Figure 4.9: Verification of ANSYS Mechanical Output. ....	84
Figure 4.10: Temperature distribution after 30 rounds fired. ....	86
Figure 4.11: Temperature distribution after 60 rounds fired. ....	86
Figure 4.12: Temperature distribution after 90 rounds fired. ....	87
Figure 4.13: Percent error from experiment. ....	88
Figure 4.14: Comparison of ANSYS results to data collected by Windham (1994 and 1996). ...	90
Figure 4.15: Bore and external temperatures for 600 round simulation.....	91
Figure 4.16: Safety factor for maximum local pressure at 270 rounds.....	91
Figure 4.17: Safety factor for maximum local pressure at 450 rounds.....	92
Figure 4.18: Safety factor for maximum local pressure at 548 rounds.....	92
Figure 4.19: Equivalent stress at the time of barrel failure.....	93
Figure 4.20: Initiation of barrel failure at 548 rounds. ....	93
Figure 4.21: Temperature distribution at time of failure. ....	94
Figure 4.22: Material strength at time of failure.....	94
Figure 4.23: Temperature vs. time at various cyclic rates of fire. ....	96
Figure 4.24: External temperature vs. time for various cooling time between bursts. ....	97
Figure 4.25: Relative change in external temperature for different times between bursts. ....	98

## LIST OF TABLES

Table 2.1: Example layout of firing schedule tables.....	49
Table 3.1: Experiment 1 information and ambient conditions. ....	62
Table 3.2: Experiment 2 information and ambient conditions .....	64
Table 3.3: Experiment 3 information and ambient conditions. ....	65
Table 3.4: Experiment 4 information and ambient conditions. ....	67
Table 4.1: Verification firing schedule. ....	73
Table 4.2: Percent Change in Maximum Temperature from an Element Size of 6.35E-4. ....	74
Table 4.3: Percent Change in Maximum Temperature from 64 Axial Steps.....	76
Table 4.4: Sensitivity of maximum external barrel temperature for various internal heat transfer coefficients.....	77
Table 4.5: Sensitivity of external barrel temperatures during firing for various external heat transfer coefficients.....	78
Table 4.6: Sensitivity of maximum external barrel temperatures for various external heat transfer coefficients.....	79
Table 4.7: Firing Schedule for Transient Thermal Verification. ....	79
Table 4.8: Analytical lumped cooling inputs.....	80
Table 4.9: Analytical lumped cooling outputs.....	81
Table 4.10: Final Cooling Times to 300 K. ....	82
Table 4.11: Analytical thermo-elastic stress inputs. ....	84
Table 4.12: Experiment 4 simulation inputs.....	85
Table 4.13: Firing schedule for M4A1 carbine barrel rupture simulation.....	89
Table 4.14: ANSYS simulation results of the M4 Carbine barrel failure.....	94
Table 4.15: Inputs for the effects of cyclic rate of fire simulations.....	95
Table 4.16: External barrel temperature at the end of the firing schedule.....	96
Table 4.17: Inputs for the effects of cooling time between bursts simulations. ....	97

## NOMENCLATURE

Symbol	Description	Units
$P$	Pressure	$Pa$
$V$	Volume	$m^3$
$n$	Number of Moles	$kmoles$
$R$	Specific Gas Constant	$kJ/kg - K$
$T$	Temperature	$K$
$\bar{T}$	Linearized Temperature	$K$
$b$	Covolume	$m^3/kg$
$B$	Covolume Function	$cm^3/g mol$
$C$	Covolume Function	$(cm^3/g mol)^2$
$\Delta B$	Constituent Constant	$cm^3/g mol$
$\Delta C$	Constituent Constant	$(cm^3/g mol)^2$
$K(T)$	Constituent Equilibrium Constant	$ul$
$U$	Internal Energy	$kJ$
$HF$	Heat of Formation	$kJ/kg$
$HE$	Heat of Explosion	$kJ/kg$
$\Delta F$	Change in Free Energies between first and second groups	$kJ/kg$
$f$	Mass Fraction	$kg/kg$
$y$	Molar Fraction	$kmoles/kmoles$
$w$	Charge Weight	$kg$
$m$	Mass	$kg$
$\Delta V$	Differential Volume Element	$m^3$
$D$	Hydraulic Diameter	$m$
$k$	Thermal Conductivity	$W/m - K$
$\rho$	Density	$kg/m^3$
$C_p$	Specific Heat	$kJ/kg - K$
$\alpha$	Thermal Diffusivity	$m^2/s$
$\gamma$	Ratio of Specific Heats	$ul$

$x$	Axial Position of Point of Interest	$m, in$
$L$	Barrel Length	$m, in$
$X$	Axial Position of Projectile	$m, in$
$u$	Velocity	$m/s$
$t$	Time	<i>seconds</i>
$Re$	Reynolds Number	<i>ul</i>
$Nu$	Nusselt Number	<i>ul</i>
$Gr$	Grashof Number	<i>ul</i>
$Ra$	Rayleigh Number	<i>ul</i>
$Pr$	Prandtl Number	<i>ul</i>
$Bi$	Biot Number	<i>ul</i>
$\varsigma$	Stephan – Boltzmann Constant	$W/m^2 - K^4$
$\omega$	Emissivity	<i>ul</i>
$h$	Heat Transfer Coefficient	$W/m^2 - K$
$\bar{h}$	Linearized Heat Transfer Coefficient	$W/m^2 - K$
$\varphi(\eta)$	Velocity Function	<i>ul</i>
$\eta$	Velocity Variable	<i>ul</i>
$\Psi(t)$	Non-dimensional Boundary Layer Momentum integral	<i>ul</i>
$\tau_w$	Boundary Layer Friction at Bore Surface	$Pa$
$\phi$	Boundary Layer Variable Coefficient	<i>ul</i>
$\psi$	Boundary Layer Variable Exponent Constant	<i>ul</i>
$\delta$	Boundary Layer Thickness	$m$
$\mu$	Dynamic Viscosity	$kg/m - s$
$\nu$	Kinematic Viscosity	$m^2/s$
$\beta$	Coefficient of Thermal Expansion for Natural Convection	$1/K$
$\xi$	Kirchoff Constant	$1/K$
$g$	Gravitational Constant	$m/s^2$
$A$	Area	$m^2$

$Per$	Perimeter	$m$
$\dot{Q}_i$	Heat Flux to Face $i$	$kJ$
$\dot{Q}_{i+\Delta i}$	Heat Flux from Face $i + \Delta i$	$kJ$
$W_{friction}$	Frictional Work done by Projectile	$kJ$
$HG$	Internal Heat Generation	$kJ/m^3$
$E$	Young's Modulus	$Pa$
$\sigma$	Stress	$Pa$
$\varepsilon$	Strain	$m/m$
$\ell$	Deformation	$m$
$\mathcal{L}$	Coefficient of Linear Thermal Expansion	$1/K$
$\zeta$	Poisson's Ratio	$ul$
$Z$	Axial Strain Constant	$m/m$
$S$	Strength	$Pa$
$SF$	Safety Factor	$ul$
$\Phi$	Lumped Cooling Time Constant	$1/s$

## SUBSCRIPTS

<b>Symbol</b>	<b>Description</b>
<i>propellant</i>	Solid Propellant
<i>products</i>	Products of Combustion
<i>projectile</i>	Projectile
0, 1, 2, 3, ...	Level of Constant
<i>inner</i>	Internal Surface
<i>outer</i>	External Surface
<i>ex</i>	Explosion
<i>BBL</i>	Barrel
<i>ult</i>	Ultimate
<i>yld</i>	Yield
<i>avg</i>	Average
<i>mean</i>	Mean
<i>surf</i>	Surface
<i>cross</i>	Cross Section
<i>char</i>	Characteristic
<i>Base</i>	Projectile Base
<i>Chamber</i>	Chamber
<i>Muzzle</i>	Muzzle
<i>gas</i>	Main Stream Combusted Gas
<i>res</i>	Residual
<i>x</i>	Axial Position
<i>r</i>	Radial Position
$\theta$	Angular Position
<i>i</i>	Item, Surface, or Constituent identifier
<i>s</i>	Nitrogen Content of Nitrocellulose
<i>L</i>	Length of Barrel
<i>air</i>	Ambient Air

<i>forced</i>	Forced Convection
<i>natural</i>	Natural Convection
<i>rad</i>	Radiation
<i>mixed</i>	Mixed Convection
<i>vm</i>	Von Mises
<i>initial</i>	Initial

## ABSTRACT

The objective of this thesis is to predict the transient temperature distribution and thermo-elastic stress in gun tubes. Necessary background about the design of gun tubes and the corresponding constraints and physical phenomena is discussed; general theories of heat transfer in gun tubes and test reports on the specific weapon systems are considered in this thesis. A modeling and simulation method is developed and implemented using commercially available ballistics software and ANSYS FEA simulation software. The capability of predicting the transient temperature distribution of an AR-15 rifle is validated by four experiments with different firing schedules. For these experiments, an FLIR E8-XT thermal camera is used to record temperatures. The predicted model is validated by comparing simulated thermo-elastic stresses in an M4A1 Carbine barrel with the tested data published in the literature. Overall, the percent error of experimented and simulated temperatures is less than 10%; while the error increases as the number of cartridges fired increases. The maximum percent error occurring to the AR-15 barrel is 12.3% at 0.2032 meters. This suggests that the effect of heat transferred from the gas port should not be neglected. The simulated rupture of the M4A1 Carbine barrel occurs at 548 rounds, 0.092 meters from the breech, at a temperature of 1090 K. The resulting percent errors from published experiments are 7.4% in the number of rounds until failure and 9.7% in location and temperature at failure. Additional simulations have been performed to provide insight into the effects of cyclic rate of fire and cooling time between bursts on the temperature distribution of an M4A1 Carbine barrel. The simulation results suggest that the cooling time between bursts has a greater impact on the barrel's temperature distribution.

# 1 INTRODUCTION

The main objectives of this work are to predict the transient temperature distribution and thermo-elastic stress in gun barrels. The AR-15 and M4A1 Carbine platforms are used in this thesis to validate the transient temperature distribution and thermo-elastic stress predicted by simulations. The modeling and simulation approach combines calculations performed in Excel with FEA simulations performed in ANSYS. Sensitivity studies provide insight into the effects of problem discretization, heat transfer coefficients, and firing schedules. Accurately predicting the phenomena of gun tube heating and failure will allow for more informed decisions to be made in barrel design.

## 1.1 Background

In designing a system, it is desirable to specify a set of functional requirements to initialize the design process. For a weapon system, the key functional requirements are often specified by government agencies or a product-design team for targeted users. These requirements define the purpose and scope of the weapon system's use. Common functional requirements are system weight, physical dimensions, effective range, cyclic rate of fire, fire modes, firing schedules, ammunition, ammunition capacity, accuracy and precision, component lives, and maintenance schedules.

A critical component of a successful weapon system is the gun tube or barrel. The gun tube is the component that discharges the projectile toward a target at a specified velocity. The gun tube is a tubular pressure vessel that restrains the propellant gas in all directions except that of projectile travel, thus directing the impetus of the gas against the projectile (AMCP 706-252, pg. 1).

### 1.1.1 Regions of a Gun Tube

The primary regions of a generic gun tube consist of the breech, chamber, bore, and muzzle as shown in Figure 1.1, and are often standardized for a specified cartridge. These regions and the outer profile of the gun tube must be designed to withstand the firing phenomena. This section provides a brief description of the breech, chamber, bore, and muzzle.

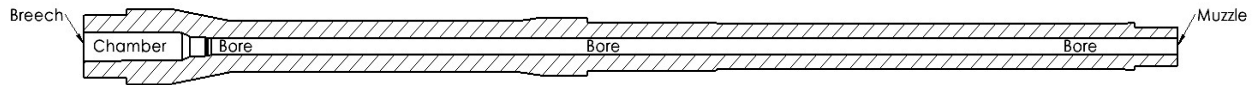


Figure 1.1: Typical Gun Tube Regions.

#### 1.1.1.1 The Breech

The breech is the interface between gun tube and the mechanism that seals the chamber. The breech and barrel assembly act as a unit in transmitting the resultant force of firing to the structure supporting the tube.

#### 1.1.1.2 The Bore

The bore is the inner surface of the cylinder and the interface with the projectile. The bore can either be smooth or contoured. Smooth bores simply consist of a circular cross-section, approximately the diameter of the projectile. A contoured bore uses a geometric pattern to control the projectile's motion. Normally, contoured bores are rifled. Rifled contour bores have grooves with a specified twist rate formed into the bore along its axis. The rifling pattern is engraved into the projectile shortly after ignition and imparts spin to the projectile. Some bores may be choked, or tapered, to a smaller diameter near the muzzle. Bore dimensions are commonly standardized for the specified cartridge. However, the rifling method and contour may not be specified.

#### 1.1.1.3 The Muzzle

The muzzle is the open end of the gun tube, the exterior of which is often threaded to allow for the attachment of blast deflectors, flash hiders, muzzle breaks, and suppressors. The muzzle may also act as a gas piston for recoil operated weapons by the inclusion of a muzzle booster. This region of the gun tube is the least standardized, which allows for greater freedom in muzzle design.

## 1.1.2 Functional Requirements of a Gun Tube

### 1.1.2.1 Weight and Dimensions

Weight requirements depend on the caliber and intended use of the weapon. Sufficient history of firearms development exists such that reasonable weight requirements for a weapon system can be set before a design is started. In many small arms, the gun tube is a large fraction of the total system weight. Common constraints that impact the weight of a gun tube include cartridge dimensions and impulse, propellant properties, projectile muzzle velocity, accuracy and precision requirements, weapon operating system, barrel mounting and barrel changing mechanism.

### 1.1.2.2 Fire Rate and Fire Mode

A fire rate is the commonly described in terms of rounds per minute (rpm). Fire rate is independent of fire mode; fire mode relates to the number of cartridges fired per trigger pull. A fire mode commonly consists of single shot, repetition pull, repetition pull and release, multi-shot burst, and fully automatic.

Depending on the weapon and firing schedule, fire rate can have a significant impact on barrel temperature. Generally, fire rate is divided into three categories: sustained rate of fire, rapid rate of fire, and cyclic rate of fire. Cyclic rate of fire is dependent on the mass-spring-damper system of the weapon's operating mechanism and is the maximum achievable fire rate. Rapid rate of fire is generally defined as the rate at which the weapon can be fired for two minutes before cooling is required to prevent overheating. Sustained rate of fire is rate at which a weapon can continuously fire for an indefinite amount of time without overheating.

### 1.1.2.3 Firing Schedule

The firing schedule refers to a sequence of firings according to a defined time frame. The firing schedule consists of several distinct time periods: the firing time, time between consecutive shots, burst time, and cooling time between bursts. The firing time is the time of combustion and exhaust for a single cartridge. The firing time is very short, on the order of single digit milliseconds. The firing time is followed by the time between consecutive shots, which is characterized by the time needed to load, and fire, the next cartridge. The time between consecutive shots is calculated

using the cyclic rate of fire. The burst time is calculated using the cyclic rate of fire and the number of shots specified for a burst. Finally, the cooling time between bursts is a pause in firing for a specified time.

Firing schedule defines the thermo-elastic stress a gun tube must endure. Firing schedules specified in operator's manuals are often broad and generic, usually being defined as a fire rate for a given amount of time. These firing schedules are often provided for rapid and sustained rate of fire. For design purposes, firing schedules often specify the minimum number of continuously fired cartridges at maximum cyclic rate of fire. To meet a firing schedule, the designer has the most freedom in specifying the material used and designing the outer profile of the gun tube.

### **1.1.3 Firing Phenomena**

The firing phenomena consists of thermal, mechanical, and chemical effects, which are tightly coupled, that act together to erode the gun tube. There are many publicly available studies that investigate the internal ballistics cycle on the gun tube.

#### **1.1.3.1 Thermal Effects**

The issue of overheating the gun barrel is as old as the advent of firearms itself. The primary effect of gun barrel overheating is the decrease of gun tube structural integrity. However, other issues arise sooner that affect the performance of the firearm and can have lasting effects, such as excessive erosion, loss of accuracy, and seizing of the operating mechanism. An increased temperature can also negatively impact accuracy by exciting unrelieved stresses caused during the manufacturing processes. In machine guns, the barrel temperature often limits the number of continuously fired shots. The strength of the barrel material decreases with the increase in temperature, which increases the risk of barrel rupture.

In the simplest sense, the cartridge and barrel can be modeled as a piston in a cylinder with one closed end. The flow in the cylinder can be characterized as forced internal developing compressible flow with the effects of skin friction and heat transfer. The combustion of solid propellants produces a large amount of heat and the temperature difference between the bore surface and the gas is always large. Due to the velocity and pressure of the gas flow during the firing process, the boundary layer along the bore surface is very thin. This causes a large

temperature gradient between the gas and the bore. This results in a high rate of heat transfer to the barrel. Though the firing time is very short, the high rate of heat transfer significantly increases the barrel temperature (Hunt, 1951, pg. 272). Temperatures of the combusting gas can be over 3000 K, while the melting point for steel is between 1644 K to 1813 K.

There are various forms for the internal forced convection heat transfer coefficient ( $h_{gas}$ ) in the literature. Feng et al. (2019, pg. 6) and Evci (2018, pg. 2128) use an equation for  $h_{gas}$  in the form

$$h_{gas} = 0.023 \left( \frac{k_{gas}}{D_{inner}} \right) Re_{gas}^{0.8} Pr_{gas}^Y . \quad 1.2.1$$

Feng et al. (2019, pg. 6) use  $Y = 0.4$ , and Evci (2018, pg. 2128) uses  $Y = 0.3$ . This is the common form for fully-developed turbulent internal forced convection. Conroy (1991, pg. 3) uses an equation for  $h_{gas}$  analogous to fully-developed turbulent flow over an isothermal flat plate.

$$h_{gas} = 0.037 \left( \frac{\mu_{gas}}{\chi} \right) Re_{gas}^{0.8} \left( \frac{C_t}{C_{tl}} \right) C_{p_{gas}} . \quad 1.2.2$$

Corner (1950), Hunt (1951), and Shelton et al. (1973) use equations for  $h_{gas}$  derived from the governing equations for continuity, energy, and momentum transfer. The equation for  $h_{gas}$  Corner (1950) and Hunt (1951) use is derived from the boundary layer momentum integral and will be provided in section 2.2.4. Shelton et al. (1973, pg. 40) use an equation for  $h_{gas}$  in the form

$$h_{gas} = \rho_{gas} u_{gas} C_{p_{gas}} \left( \frac{C_f}{2} \right) / Pr_{gas}^{2/3} , \quad 1.2.3$$

$$C_f = 2A \left( \frac{1}{Re_{\theta}^{0.268}} \right) , \quad 1.2.4$$

$$A = \frac{0.123}{10^{0.678H}} , \quad 1.2.5$$

$$Re_{\theta} = \frac{\rho_{gas} u_{gas} \theta}{\mu_{gas}} . \quad 1.2.6$$

Where  $\theta$  is the momentum thickness of the boundary layer along the length of the barrel to the base of the projectile,  $H$  is the profile shape factor, which is the ratio between the displacement thickness of the boundary layer and the momentum thickness of the boundary layer,  $C_f$  is the local wall friction coefficient, and  $A$  is a coefficient in the wall shear stress expression. Figure 1.2

provides a comparison of the axially varying heat transfer coefficient and boundary layer thickness for various profile shape factors at a specific time during the firing time.

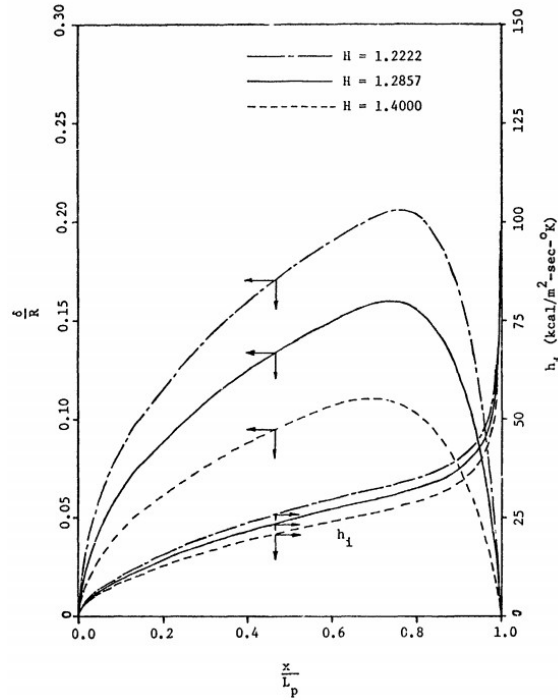


Figure 1.2: Boundary layer thickness and internal heat transfer coefficient (Shelton, et al., pg.103).

The heat loss to the barrel up to the time of ejection of the shot is between 4% and 9% of the total energy liberated and additional heat transfer occurs between the exhausting propellant gas and the barrel after shot ejection (Hunt, 1951, pg. 271). Due to the magnitude of heat transfer, the bore surface can experience phase changes, softening and melting, and cracking due to expansion and contraction associated with thermal cycling (Johnston, 2005, pg. 3). Research into barrel materials, barrel liners, propellant composition, barrel geometry (fins, barrel thickness, increased surface area, etc.), external coolants, quick change or replaceable barrels, and multiple barrels is ongoing to mitigate this problem.

In 1975, L.H. Russel evaluated the effects of additives in the propellant charge on reducing the internal heat transfer coefficient. The additives in the propellant charge are assumed to leave an insulating residue along the bore after firing for the next shot. Russel (1975) proposes a semi-empirical equation for the internal heat transfer coefficient, requiring  $T_{gas}$  and  $T_{r,inner}$  be explicitly known, while  $A_0$  and  $c$  are time-dependent parameters.

$$h_{gas} = \frac{A_o e^{-ct}}{(T_{gas} - T_{r,inner})} \quad 1.2.7$$

Russel (1975) shows that the bore temperature with an uncoated propellant can reach upwards of 1321 K, while the bore temperature with an insulative coating on the propellant can reach between 940 and 1049 K.

Gedalla et al. (2019) performed finite element simulations to predict the radial temperature distribution of different barrel cross-sections resulting from continuous fully automatic fire. Circular, hexagonal, triangular, and rounded triangular cross-sections were evaluated using four different materials, i.e., AISI 4130 steel, Tantalum, Titanium, and STK 4 ceramic. The simulations have shown that 4130 steel has the lowest bore temperature, 627 K, and the second lowest external wall temperature, 489 K, at the end of a 125 round firing schedule (Gadalla et al, 2019, pg. 5). The STK4 has the lowest external temperature, 382 K, but the highest bore temperature, 758 K (Gadalla et al., 2019, pg. 5). Tantalum and titanium are in between these two extremes. In addition, the titanium barrels would have a weight decrease of 41% while the overall barrel's temperature increases by 49%. Gadalla et al. (2019) showed the typical circular cross-section provided better thermal management over non-circular geometries with constrained size, though these non-circular cross-sections reduced barrel weight. However, non-circular geometries with constrained cross-sectional areas equal to that of the circular cross-section improved thermal management, the best of which is the hexagonal geometry (Gadalla et al., 2019, pg. 5).

### 1.1.3.2 Mechanical Effects

This section presents some standards with regards to gun tube design. The fundamental data used for the design of gun tubes and breech closure are given by the pressure-travel curve of the propellant gases calculated from the ballistic equations (AMCP 706-252, pg. 38). To ensure uniformity among gun tube designers, agreement on the design data definition, compilation, and usage is needed (AMCP 706-252, pg. 38). The standards with regards to the pressure-travel curve are Computed Maximum Pressure (CMP), Rated Maximum Pressure (RMP), Permissible Mean Maximum Pressure (PMMP), and Permissible Individual Maximum Pressure (PIMP). Thick-walled pressure vessel equations are used in accordance with these standards. It should be noted that these standards provide a minimum requirement for gun tube strength, as operation temperatures for material strength are assumed to be at 294.3 K.

Though pressure stress is significant, the gun tube is subjected to thermal stress, shrink fitting stress, stress concentrations from rifling and other internal features, and rotational stress from imparting spin on the projectile during firing. These stresses, as well as barrel harmonics, must be considered when designing a gun tube. Cheng et al. (2014) show the axial stress is primarily comprised of thermal stress and is a dominant component in coupled Von Mises stress. Between the three components of coupling stress, the axial component is most dominant, while the radial component is least dominant (Cheng et al. 2014, pg. 5).

Other mechanical effects of the firing phenomena include erosion from direct gas and solid particulate impingement along the bore, shearing action of the turbulent flow, removal of material by projectiles due to frictional forces, and crack propagation due to ballistic pressure cycles (Johnston, 2005, pg. 3). It is also possible that the number of firing cycles reaches the fatigue life of the barrel before the bore has eroded past acceptable limits. Thermal and chemical effects on fatigue life of the barrel material must also be considered.

#### 1.1.3.3 Chemical Effects

The combustion typically produces carbon monoxide, carbon dioxide, hydrogen, water vapor, nitrogen, and other dissociated products. Empirical correlations have been derived to calculate the chemical erosion of bores in gun tubes. One empirical equation for bore erosion was produced by Lawton and is described in *Understanding and Predicting Gun Barrel Erosion* (Johnston, 2005).

The chemically affected zone of the bore is on the order of one to tens of microns deep. Thermal effects penetrate much deeper and have a bearing on the formation of the chemically affected zone, as heating this zone drives phase changes, crack formation, melting, and chemical species diffusion and reaction rates in the barrel material. Figure 1.3 shows the condition of the AR-15 medium profile barrel after the experiments, the number of cartridges fired through the barrel is unknown.

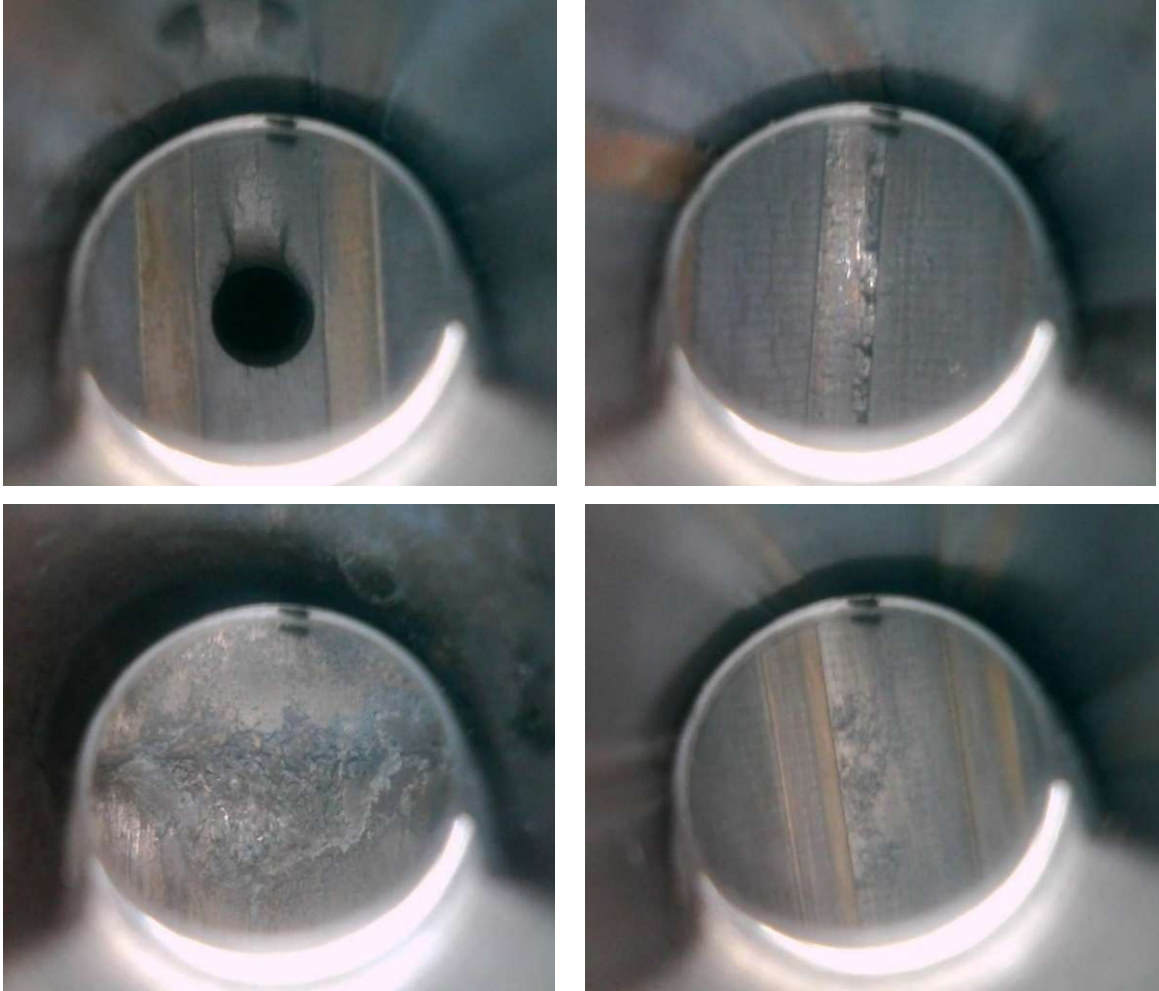


Figure 1.3: Bore erosion in the gun tube of an AR-15 rifle.

Propellant gas species cause erosion by two different processes—surface reactions and thermal diffusion (Johnston, 2005, pg. 4). Surface reactions between the hot gas species and the bore material produce weaker, lower melting point compounds, which are easily removed by thermal and mechanical processes. Thermal diffusion of gas species from the bore surface into the barrel material results in interstitial atoms in the lattice of the bore metal, which alter the structure, physical properties, and melting point of the barrel material resulting in reduced strength and increased brittleness, which is more susceptible to erosion (Johnston, 2005, pg. 4). Carburization, oxidation, and hydrogen embrittlement are some of the chemical effects that propellants can have on barrels. Russel (1975) suggests titanium dioxide, hydrated magnesium silicate, and a highly viscous silicone oil are successful in reducing bore temperatures and slowing down the rate of bore

erosion. Refractory metal bore liners have shown significant reduction in bore erosion, and consequently have greatly improved barrel life.

## **1.2 The M16, M4 Carbine, and AR-15 Family of Weapons**

The M16 family of weapon systems are classified as air cooled, gas operated, and shoulder fired weapons. The gas operation is achieved by venting propellant gas from the bore, through a duct, into a cavity in the bolt group. The cavity is between the bolt and the bolt carrier. The bolt carrier acts as a piston. The energy imparted to the bolt carrier is enough to perform the necessary functions of unlocking the bolt, extracting the cartridge, cocking the hammer, ejecting the used cartridge casing, feeding the next cartridge, and locking the bolt.

### **1.2.1 Barrel Overheating**

The service life of M16 weapons has been plagued with controversies. Many books cover these controversies in depth. However, this study will summarize the concerns with M4A1 Carbine barrels overheating. There are three publicly available studies, one by Elbe (1975) and two by Windham (1994 and 1996), that investigate overheating of M16 and M4A1 Carbine barrels.

Short barreled M16s, adopted as M4 Carbines, have been used commercially and by military services since the 1960's. Incidents of M4A1 carbine barrels rupturing have been reported by special forces units and concerns have been expressed that the M4A1 is more susceptible to barrel rupture than the M16 (Windham, 1996, pg. 1). Complaints of handguards overheating during severe firing schedules in early carbines preceded the barrel ruptures. Due to the complaints, development of new handguards to mitigate this problem began. The new handguard design adopted consists of a large diameter polymer grip with double aluminum liners. However, by insulating the operator's hand from the barrel temperature, the handguard also insulates the barrel from heat transfer to the environment. This insulation raised concerns about excessive barrel temperatures being reached with a fewer number of cartridges fired (Windham, 1994, pg. 2).

Elbe (1975) provides some context about the M16 barrel temperatures. Elbe (1975) shows the external barrel temperature was highest approximately 101.6 mm to 152.4 mm from the breech. The location of this region varies based on the firing schedule. The region starts approximately 152.4 mm from the breech at lower fire rates between 10 and 60 rounds per minute. However, at

120 and 240 rounds per minute, the location moves to approximately 152.4 mm. Elbe (1975) notes that thermo-couples on the upper surface of barrel are slightly higher than on the lower surface. Elbe (1975) notes that there were two areas of relatively lower temperatures. Those areas are the chamber and the front sight block, or gas block. Elbe (1975) explores the effect of fire mode and different ammunition on external barrel temperatures and concludes that changing only the mode of fire has no effect on heat input to the barrel per round fired; therefore, given a rate of fire the average heat input per unit time must also be independent of mode of fire (Elbe, pg. 5). Elbe's (1975) experiments also show that propellant burning characteristics and temperatures have a significant impact in the temperature response of the barrel.

In 1994 and 1996, Windham compares the barrel temperatures for both the M16 and the M4A1 Carbine. Figures 1.4 and 1.5 show the experiment results obtained by Windham (1994) for an M4A1 Carbine barrel. Windham's results for the location of maximum external temperature correlate well with the results obtained by Elbe in 1975. The results showed the maximum temperature for a barrel with no handguards is less than the barrels with handguards. The rate of cooling for a barrel with no handguards is also greater than the barrels with handguards. The difference between the bare barrel and barrels with handguards with regards to heating and cooling is considered small given the advantages of having handguards. The results obtained by Windham (1994) suggest there was no significant difference between the small and large handguards.

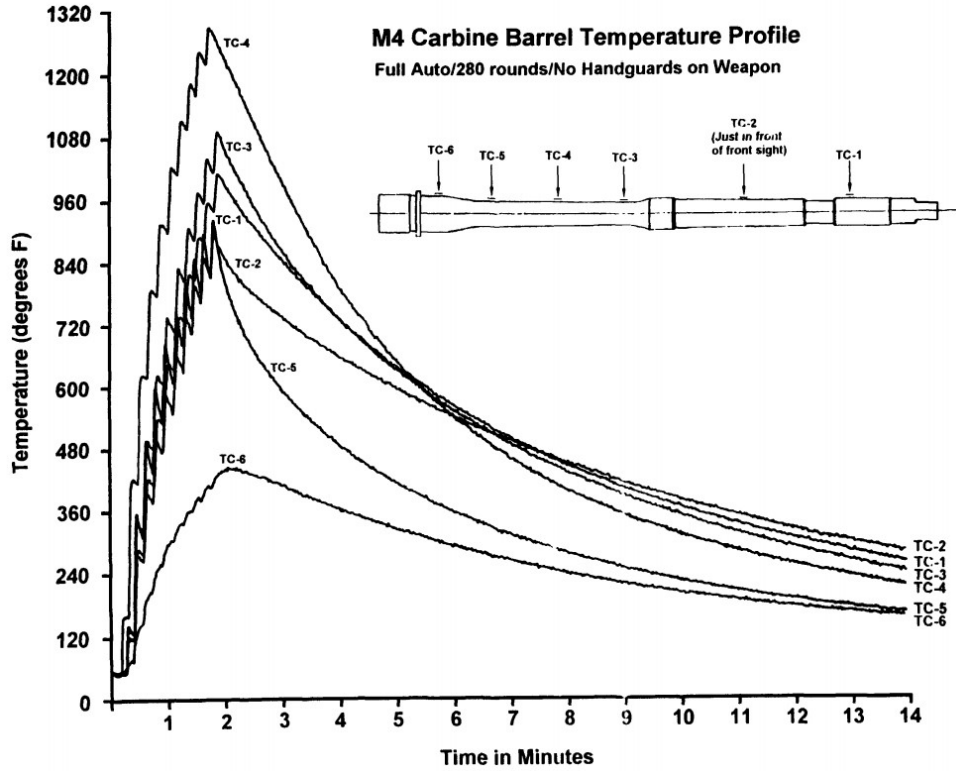


Figure 1.4: M4 carbine, no handguards, external barrel temperature (Windham, 1994, pg. 13).

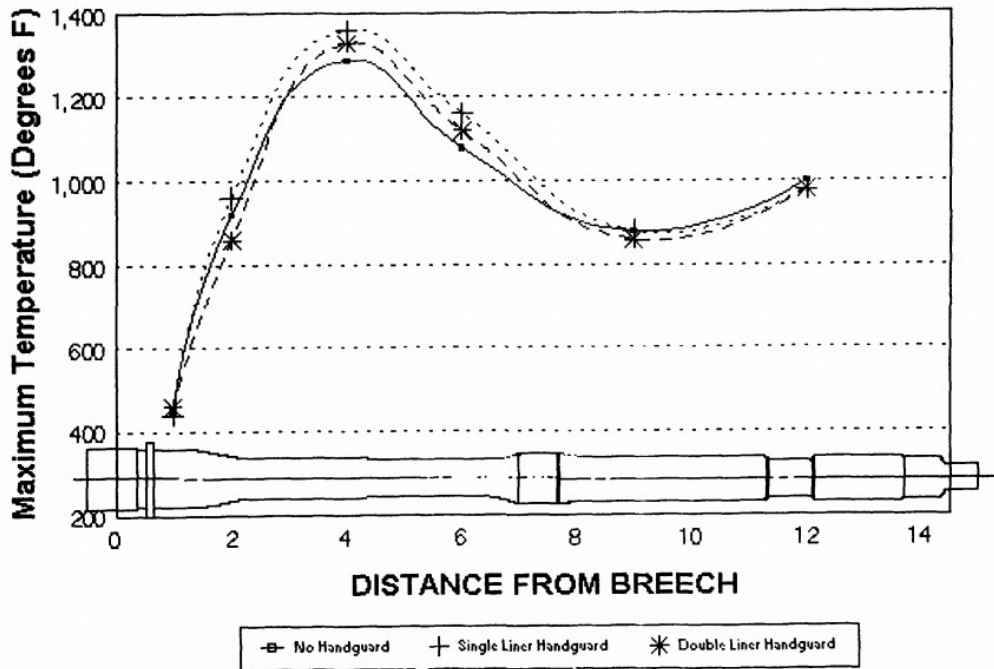


Figure 1.5: Axial temperature profile of the M4 carbine barrel (Windham, 1994, pg. 18).

In 1996, Windham performs experiments to address the concerns of barrel rupture. Windham (1996, pg. 1) finds that the M16A2 rifle barrel ruptures at 491 rounds. The rupture is a hole, 6.35 mm in length, in the top of the barrel about 203.2 mm from the chamber. Along with the rupture, the M16A2 barrel is bulged at several locations along its length and bent approximately 5 degrees. The first M4 Carbine successfully fired 540 rounds, at which point the test halted due to no more ammunition. Figure 1.6 shows the data from the first M4 Carbine experiment Windham (1996) performs. The second test for the M4A1, shown in Figure 1.7, resulted in barrel rupture at 596 rounds (Windham, 1996, pg. 2). However, an additional 30 seconds of cooling at approximately 360 rounds may have increased the number of rounds required to rupture the barrel. Failure occurs approximately 101.6 mm from the breech. The rupture is a hole, 31.75 mm by 15.9 mm at the top of the barrel. All weapons tested experience an increase in muzzle flash, and a distinct change in the sound of firing, approximately 30 rounds before the barrel ruptures. The conclusion of the report is that the M4A1 Carbine performs well with respect to the number of rounds and firing schedules required to produce a barrel rupture and a different firing pattern may reduce the probability of a ruptured barrel (Windham, 1996, pg. 3).

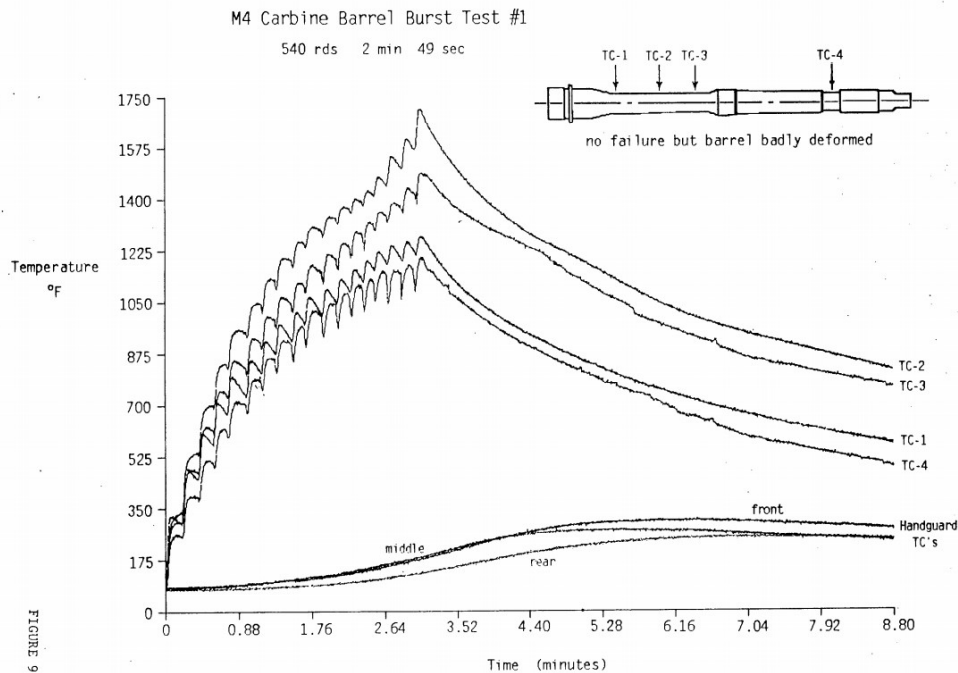


Figure 1.6: M4 carbine, fire to destruction test #1, external barrel temperature (Windham, 1996, pg. 20).

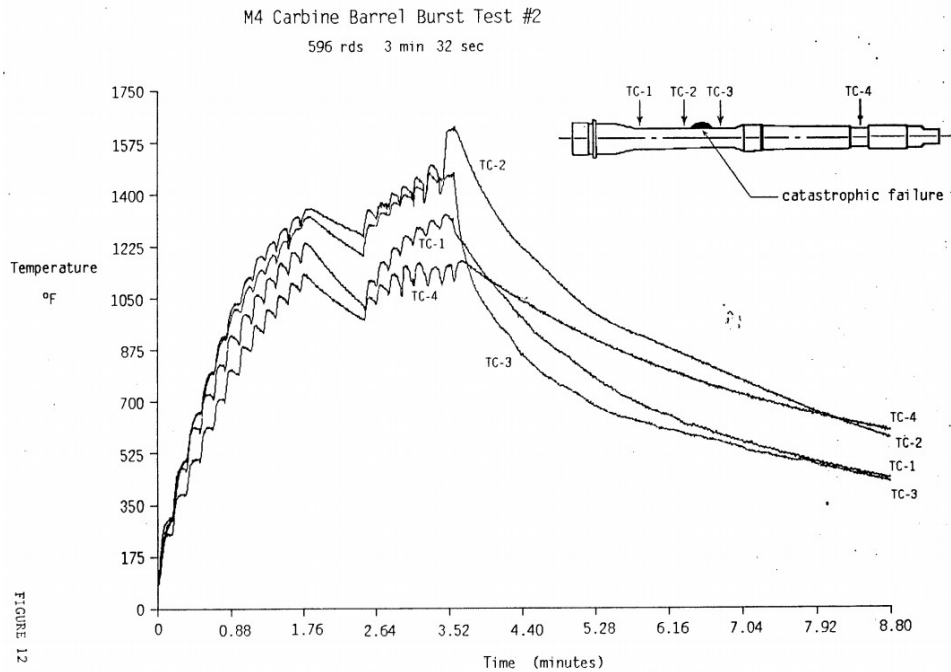


Figure 1.7: M4 carbine, fire to destruction test #2, external barrel temperature (Windham, 1996, pg. 26).

### 1.3 Thesis Organization

This thesis consists of six chapters—the content of which is summarized below.

#### 1.3.1 Chapter 1: Introduction

Chapter 1 establishes the premise for the work performed in the following chapters and includes the background on basic gun tube terminology and corresponding functions. Basic functional requirements and engineering considerations when designing gun tubes are summarized. The effects of functional requirements and the firing phenomena on gun tubes are discussed. Prior research into barrel overheating for the M16 family of weapon systems is summarized. Finally, this chapter introduces the organization of the thesis.

### 1.3.2 Chapter 2: Modeling and Simulation Method

Chapter 2 provides understanding of the physical phenomena occurring inside the gun tube, and setup a framework, Figure 1.8, for modeling and simulating the effects of the physical phenomena on the gun tube.

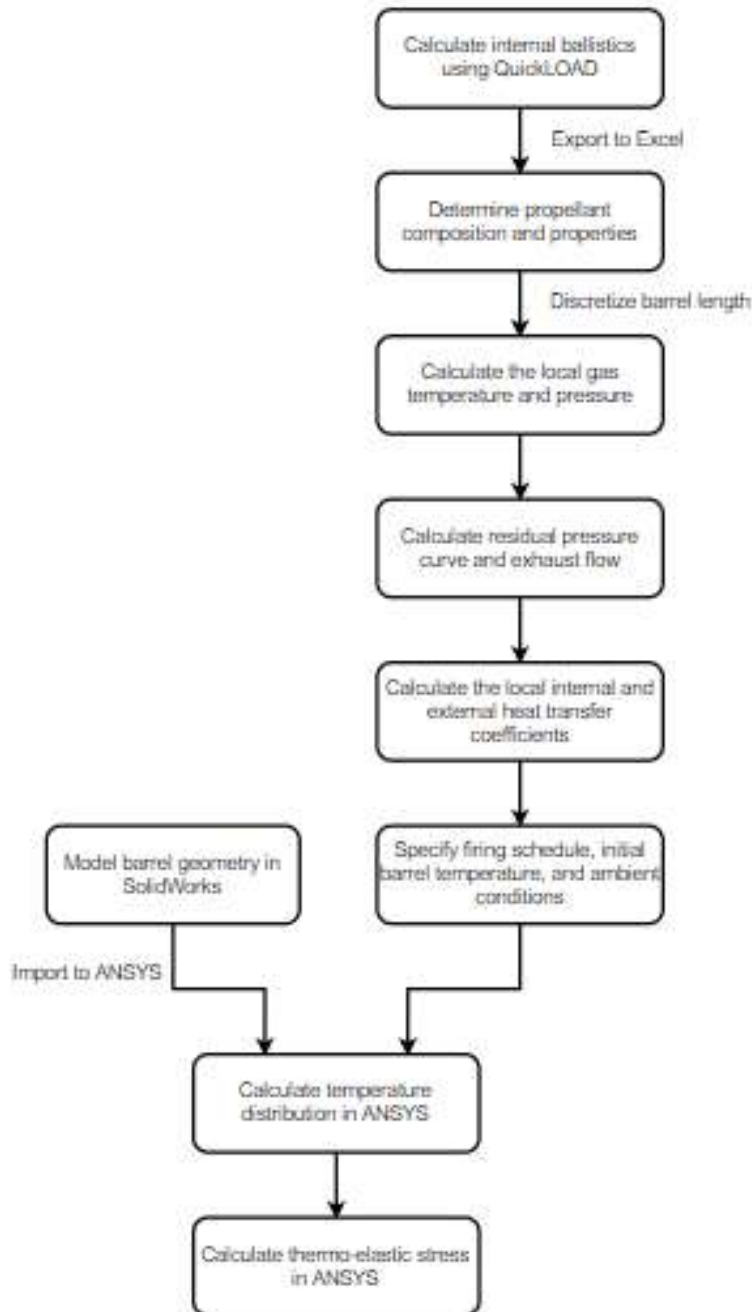


Figure 1.8: Simulation flow chart.

The chapter begins with the simplifying assumptions used for this thesis. These are the same assumptions used in *The Study of Gun Barrel's Two - Dimensional Nonlinear Thermal Conduction*. The assumptions simplify meshes and internal ballistics calculations. The following section, 2.2, discusses the model development for use with ANSYS to predict barrel temperatures during the initial design process. Therefore, the model is not intended to be a substitute for testing. The model should be compatible with commercially available ballistics software, and not require any special mathematical solving software, to allow more access for design refinement.

Section 2.2 begins with creating the barrel geometry and applying the simplifying assumptions from section 2.1. The internal ballistics can then be determined based on the weapon chosen. Often, the cartridge, bore, operating mechanism, and other barrel parameters are known. Propellant, charge weight, and projectile weight are commonly available on the ammunition manufacturer's website. QuickLOAD has a large database of powders that contains propellant thermophysical properties. For the input barrel length and cartridge, QuickLOAD calculates the shot time, projectile travel and velocity curves, breech pressure curve, and fraction of propellant burnt. It is relevant to determine the composition of the combusting gas for the physical properties of kinematic viscosity, thermal conductivity, and Prandtl Number. Naturally, the combustion constituents are based on the composition of the solid propellant.

Transient and axial discretization of the model must be iteratively found and verified using stability, sensitivity, and mesh independence studies. Sufficient transient discretization to produce stable results is a crucial initial step. Stability criteria and effects on simulations will be covered in further detail in section 4.1.1. Based on the discretization of the barrel, local pressures, temperatures, and heat transfer coefficients can be calculated from the ballistics curves.

ANSYS Transient Thermal analysis was used to apply the thermal loads and boundary conditions. Each convective load requires a heat transfer coefficient and fluid temperature. Insulated boundary conditions are applied to radially symmetric cuts and locations where the barrel is in contact with the receiver, bolt, or other non-barrel components of the weapon. Radiative loads are also applied.

ANSYS Static Structural analysis is attached to the Transient Thermal simulation to allow for an imported body temperature load. The body temperature load allows the user to select a temperature distribution within a specific time range, or the complete transient temperature distribution. With the body temperature load applied, frictionless supports are attached to the

breech face and radially symmetric cuts. The transient local pressures are applied at each internal discretized face. The material strength is calculated using the temperature distribution and a user defined result, which will allow for the calculation of the barrel's safety factor.

### **1.3.3 Chapter 3: Experiment Apparatus and Procedure**

Chapter 3 discusses data and provides figures from experiments performed to validate the transient temperature distribution of a test barrel. Figures of the apparatus and equipment used in measuring the barrel temperature of the AR-15 rifle are provided in section 3.1. The process for calibration, experiment setup, experiment execution, and data collection is provided in section 3.2. This chapter also provides the details on ambient temperature, emissivity, initial barrel temperature, distance from the thermal camera, and any issues that arose during the experiments. The collected data is exported to an Excel file for statistical analysis and plotting. Figures are provided in three-dimensions with temperature and barrel length on the y and x axis, respectively, and time denoted by different curves within the figure. Statistical analysis of the measured data is performed to find the average barrel temperatures and standard deviations. Finally, the uncertainty of the thermal camera measurements is discussed.

### **1.3.4 Chapter 4: Simulation Results**

Chapter 4 aims to verify and validate the developed modeling and simulation approach. Stability and mesh dependency studies, and input parameter sensitivity studies, are performed to ensure reliable simulation results. Simulation results are then compared to the results of a simplified analytical problem. Validation is performed by comparing simulated and experimented results. Validation of the transient temperature distribution is performed by comparing simulation results with thermal camera data. Validation of the coupled thermo-elastic stress is performed using literature references with experiment data, as destruction of the weapon was deemed too dangerous for the testing environment available. Finally, the effects of different cyclic rates of fire and cooling time between bursts are on the transient temperature distribution are discussed.

### **1.3.5 Chapter 5: Conclusion**

Chapter 5 summarizes the experiment and simulation results. This chapter also provides remarks on the practicality of the modeling and simulation process. The remarks focus on the accuracy in predicting the transient temperature distribution measured during the experiments.

### **1.3.6 Chapter 6: Recommendations**

Chapter 6 provides recommendations for future work. Also, alternate equipment and software is provided.

## 2 MODELING AND SIMULATION METHOD

A system model is a mathematical representation of a physical system used to make predictions. A simulation is the execution of the system model to produce a prediction. The modeling and simulation method is the process used to produce the prediction. This chapter describes the modeling and simulation processes by outlining the simplifying assumptions, barrel geometry, ballistics cycle, discretization, and the final implementation in ANSYS.

### 2.1 Basic Assumptions

The same assumptions from *The Study of Gun Barrel's Two-Dimensional Nonlinear Thermal Conduction* have been used to simplify the model for this project. These basic assumptions are:

- 1.) The internal and external surfaces are smooth, and irregular structures such as rifling is ignored.
- 2.) The internal ballistics parameters for each shot are independent and identical.
- 3.) The heat transfer caused by friction between the bore surface and the projectile is ignored.
- 4.) There is no internal heat generation.

### 2.2 Model Development for use in ANSYS

#### 2.2.1 Barrel Geometry

Two profiles are studied in this project. The barrel geometry used to validate the temperature distribution is a 406.4 mm barrel, with a carbine length gas system and medium profile, see Figures 2.1 and 2.2. The second barrel profile is a 406.4 mm government profile barrel, see Figure 2.3. This barrel is used to validate the thermo-elastic stress by comparing the simulated barrel failure to empirical data found by Windham (1996). It should be noted that the standard issue M4A1 Carbine barrel is 373.4 mm. However, 406.4 mm length barrel variants do exist and there is no difference in the barrel profile until 280 mm, which is past the failure point of the tested barrels. The difference is an extension of the 19 mm diameter at 280 mm.

Measurements of both barrel profiles were found using micrometers and a digital height-stand. Internal measurements were found from CIP data. Measurements for the barrel attachments are found using micrometers, calipers, the digital height-stand, and existing drawings. Barrel attachments such as flash hidens, barrel extensions, and gas blocks can be found in Appendix E.

SolidWorks is used to create the barrel and accessory geometries. To create the barrel geometry, a sketch of the internal and external profile of the barrel is created and rotationally extruded. To simplify the barrel in polar coordinates, a fractional boss revolve can be used, or a cut extrusion can be used after the barrel and accessories are assembled.

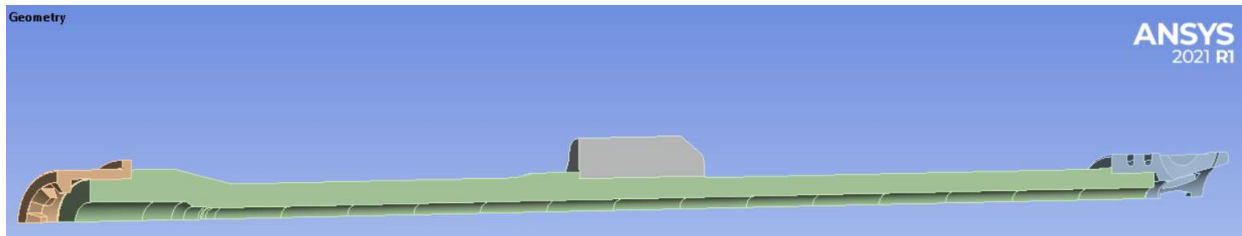


Figure 2.1: Example medium profile barrel geometry used simulations.

In this study, the barrel and accessories were assembled and cut extruded into quadrant and half-quadrant slices as shown in Figure 2.1. This simplification greatly reduced the simulation time. As the barrel is symmetric in the polar coordinates, the assumption can be made that the temperature distribution is not dependent on the polar coordinate. This allows for a zero-flux boundary condition placed along the slices of the barrel quadrant. As discussed later, the axial discretization of the barrel must be performed in SolidWorks prior to importing into ANSYS. The axial discretization can be done using offset planes and “Split-Lines” after the barrel has been modeled.

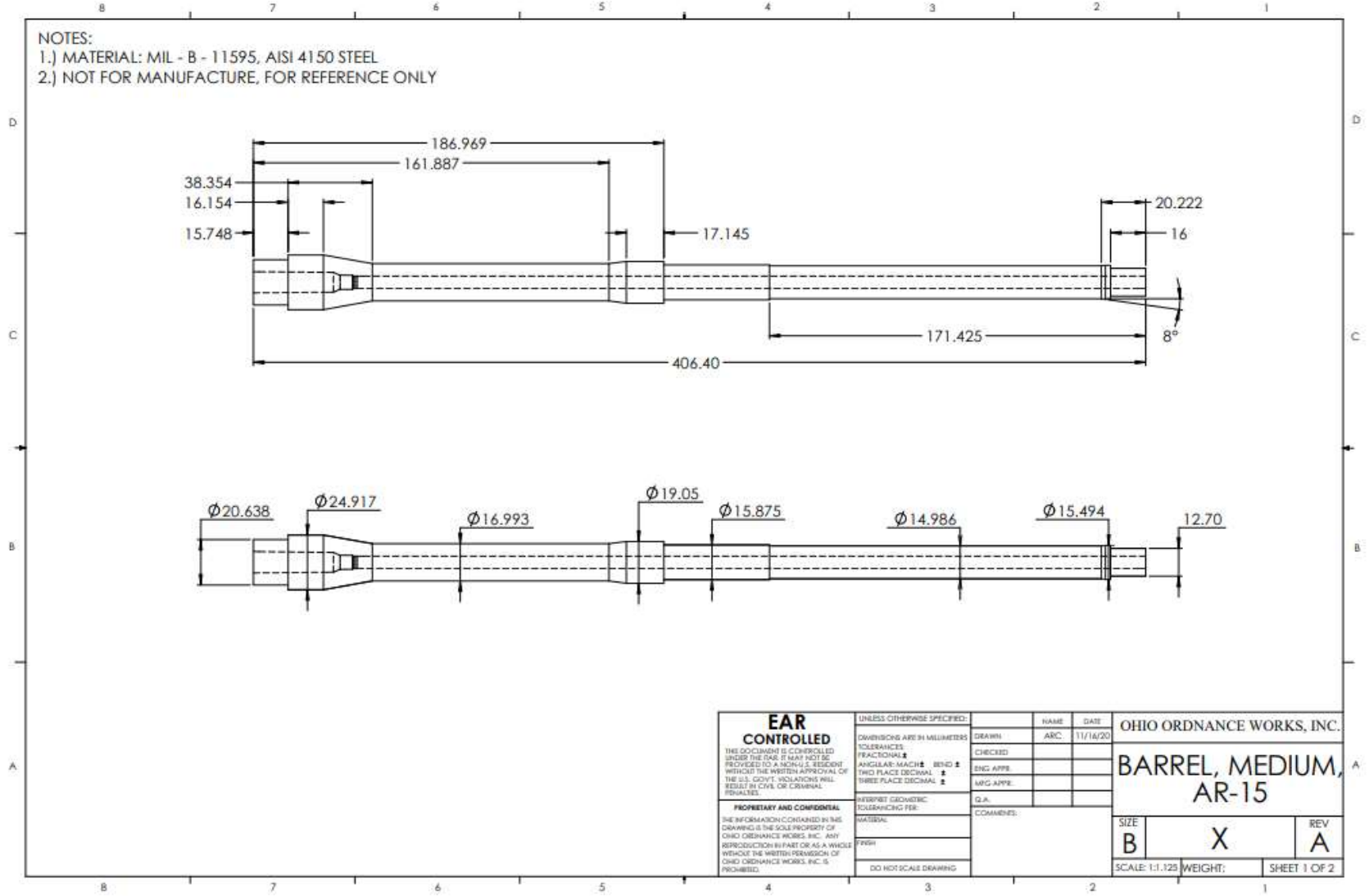


Figure 2.2: AR-15 Barrel Profile.

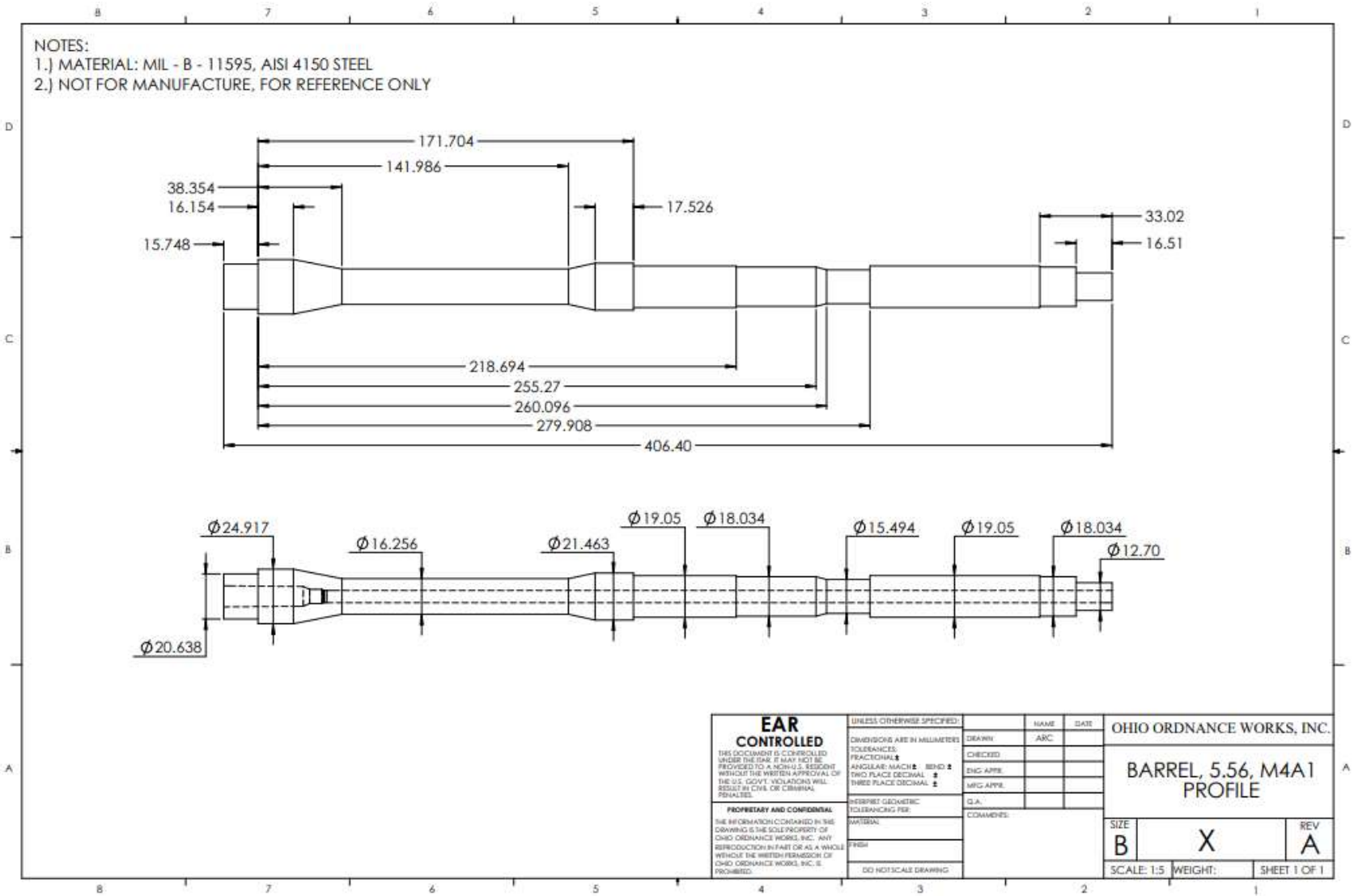


Figure 2.3: M4A1 Profile Barrel.

## 2.2.2 Determination of Propellant and Ballistic Parameters

The weapon chosen for this analysis uses the NATO 5.56 x 45 mm cartridge. To calculate the ballistic parameters of this cartridge, the internal ballistics program QuickLOAD was used. Figure 2.4 displays the start-up user interface, where the user can select from a large database of standard cartridges and powders.

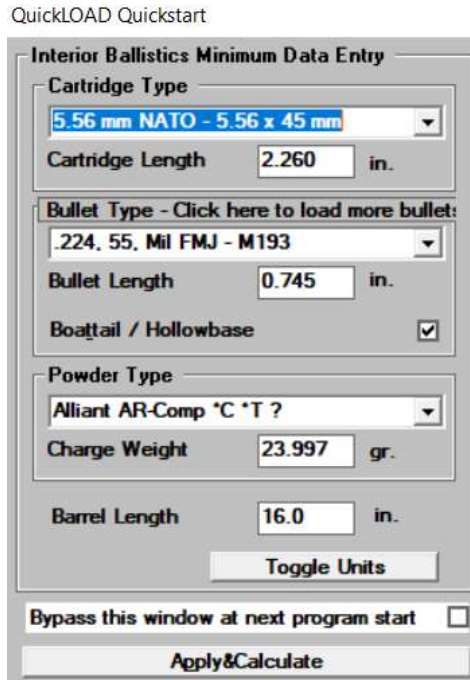


Figure 2.4: QuickLOAD Quickstart interface.

The powder chosen to evaluate the ballistic parameters is a generic 5.56 x 45 mm powder produced by Alliant Inc., which is AR-COMP. This powder is also available in the database for QuickLOAD. The outputs provided by QuickLOAD are the chamber pressure and velocity curves for the projectile. Figure 2.5 displays the chamber pressure and projectile velocity with respect to the projectile base motion. The data from Figure 2.5 will be more useful in designing a new gun tube. Figure 2.6 displays the same data with respect to time. For a heat transfer study on an existing gun tube, the data provided in Figure 2.6 will be used.

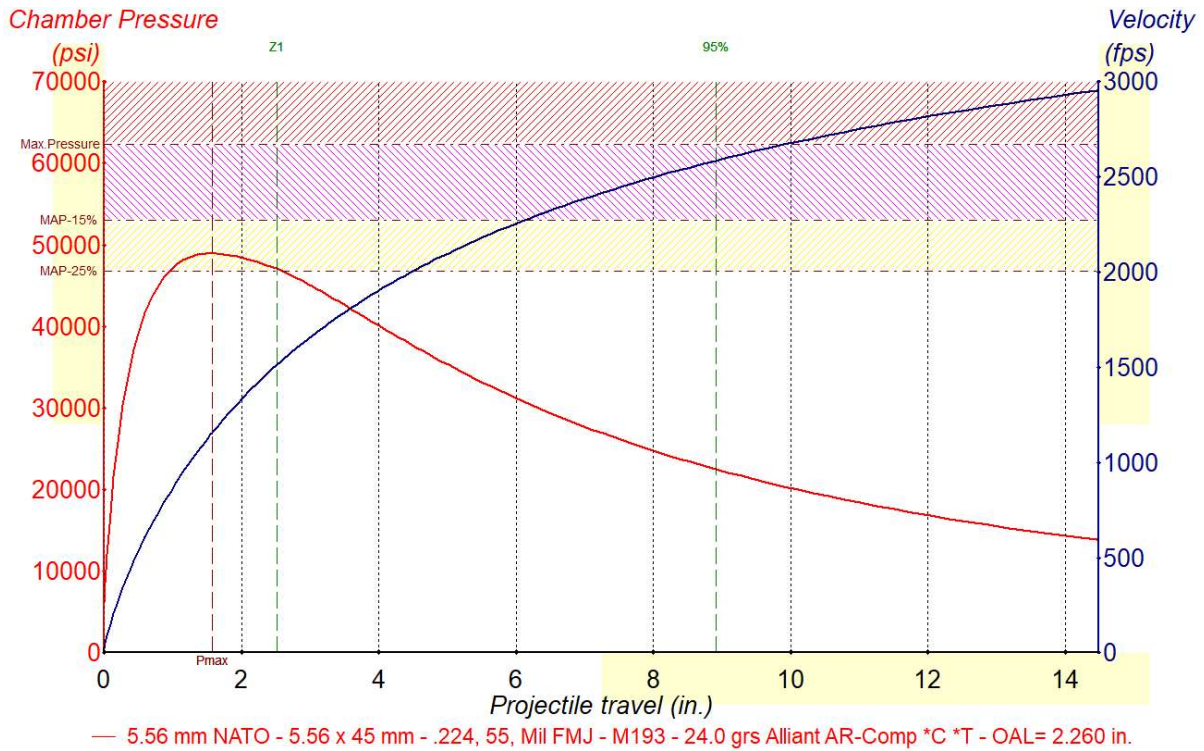


Figure 2.5: Pressure – velocity vs barrel length curves for 5.56 x 45 mm.

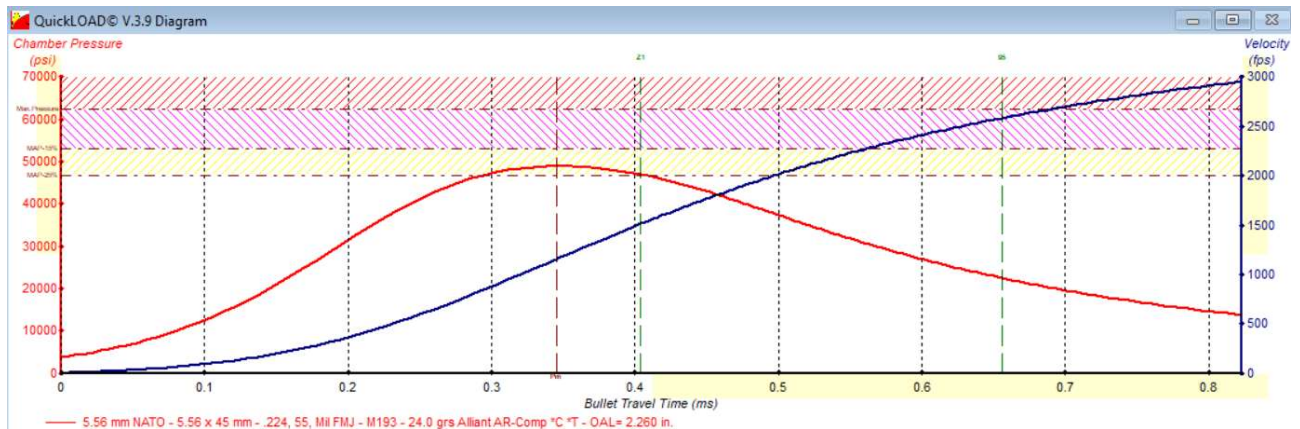


Figure 2.6: Pressure – velocity vs time curves for 5.56 x 45 mm.

The QuickLOAD output is then exported to Excel. From the ballistic curves and the propellant information, other necessary ballistic parameters and the products of combustion can be determined. Determining the composition of the combustion products is described in detail in Appendix B using Hunt’s (1951) method.

Hunt (1951, pg. 80 and pg. 273) provides the relationships between the projectile base pressure, mean gas pressure, and local pressure using

$$P_{Base}(t) = \frac{P_{Chamber}}{(1 + (w/2m_{projectile}))}, \quad 2.2.1$$

$$P_{gas,mean}(t) = P_{Base}(t)(1 + (w/3m_{projectile})), \quad 2.2.2$$

$$P_x(x, t) = P_{gas,mean}(t) \frac{1 + \frac{1}{2}(w/m_{projectile})[1 - x^2/X^2]}{1 + \frac{1}{3}(w/m_{projectile})}. \quad 2.2.3$$

The local gas temperature is assumed to be approximately mean gas temperature. The mean gas temperature can be found using the following isentropic relationship, which is provided by Hunt (1951, pg. 273),

$$T_x(x, t) \approx T_{gas,mean}(t) \quad 2.2.4$$

and

$$\frac{T_{ex}}{T_{gas,mean}(t)} = \left( \frac{P_{ex}}{P_{gas,mean}(t)} \right)^{\frac{\gamma-1}{\gamma}}, \quad 2.2.5$$

where  $\gamma$  is the ratio of specific heats for the propellant. From the mean gas temperature and composition of combustion products, the thermal conductivity, dynamic viscosity, and specific heat of the exhaust gas can be calculated using properties tables (Anthony Mills, 1995).

QuickLOAD does not calculate the residual pressure within the barrel after the projectile passes the muzzle. Methods for calculating the residual pressure are discussed in *Theory of the Interior Ballistics of Guns* by John Corner. The assumption is made that the breech pressure decreases exponentially to ambient pressure over the time of residual pressure. The first step in calculating this curve is to calculate the time of residual pressure using

$$t_{res} = \frac{w}{32.2 P_{Chamber,Muzzle} A_{bore}} (9400 - u_{projectile,muzzle}), \quad 2.2.6$$

which is the time taken for the residual pressure in the barrel to reach ambient pressure. Therefore, the exponent for the residual pressure curve can be calculated from this time and the chamber pressure when the projectile passes the muzzle. The time of residual pressure was calculated to be 1.28 milliseconds. The shot time is 0.83 milliseconds, resulting in a total time of 2.11 milliseconds. The complete ballistics cycle is displayed in Figure 2.7.

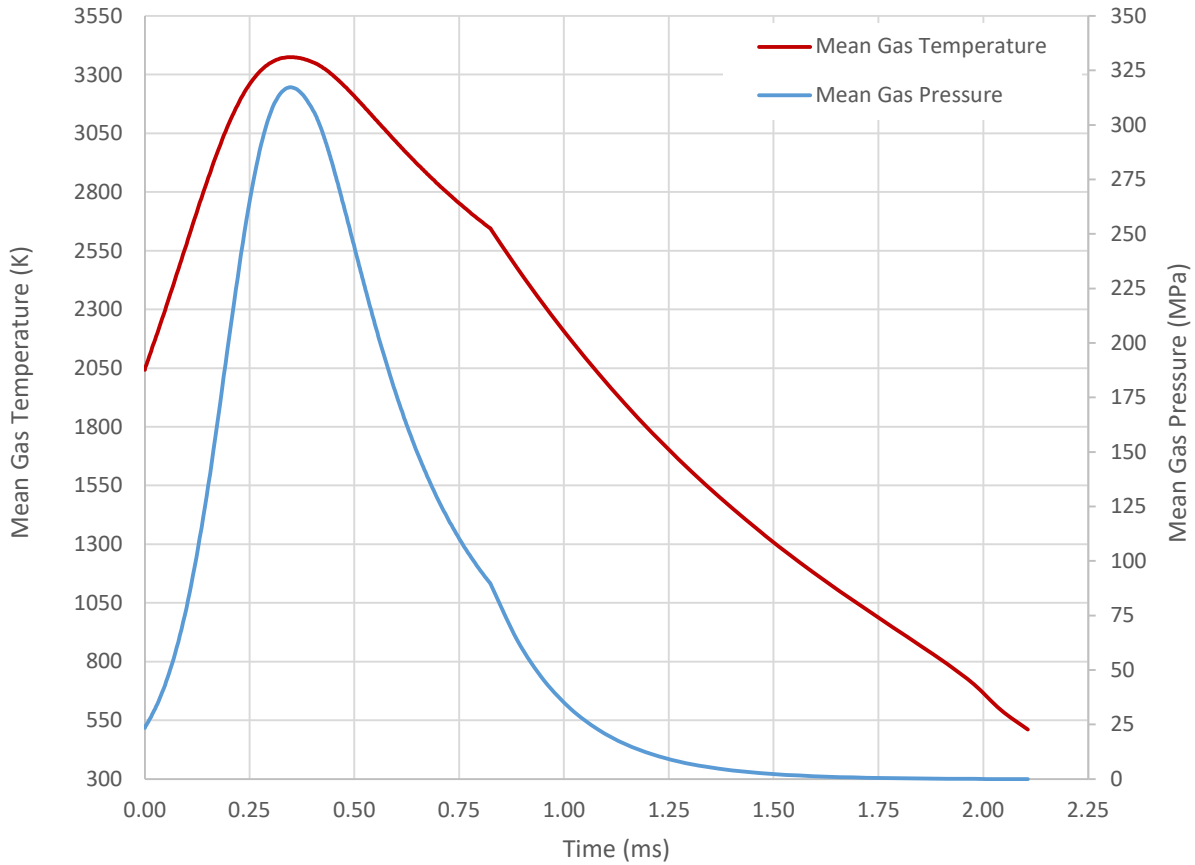


Figure 2.7: Mean gas pressure and temperature curves.

The QuickLOAD spatial output is chamber pressure versus projectile base travel. The projectile base travel must be converted to a position within the gun tube using the cartridge overall length and projectile length. The volume behind the projectile at the time of peak pressure will also reach maximum local values of pressure in accordance with equations 2.3.1 to 2.3.5. The same can be said for the gas temperature, which can be seen by interpreting Figure 2.8 from the breech to the position of peak pressure and temperature.

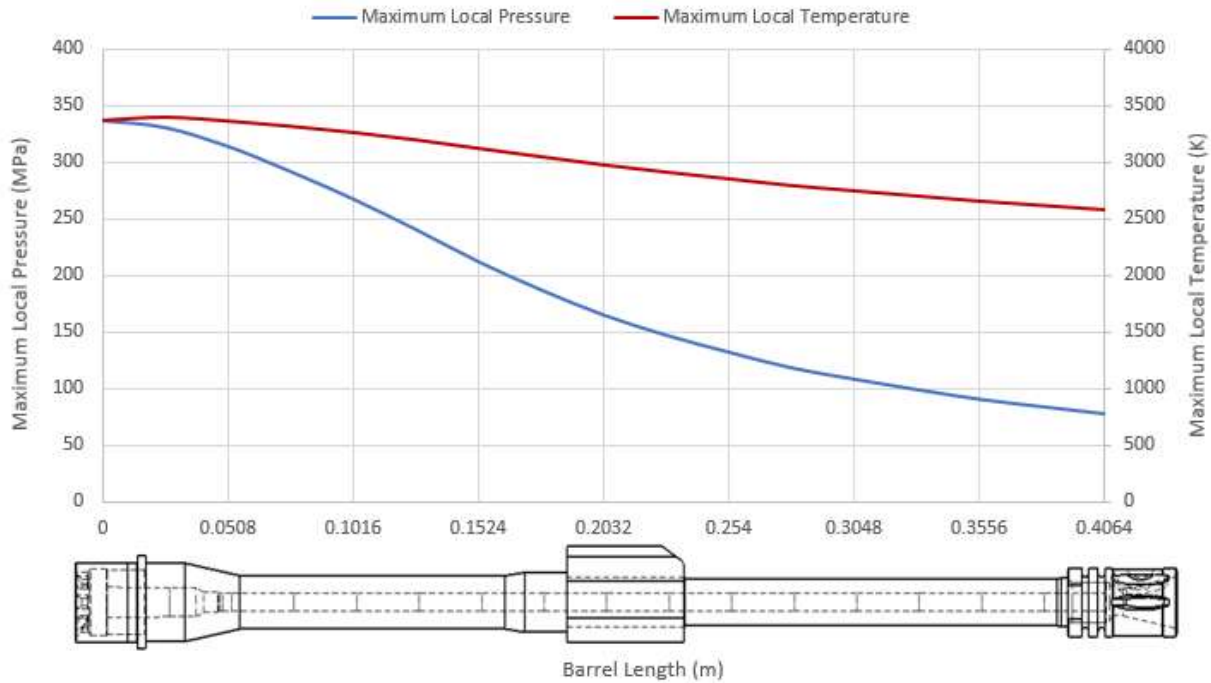


Figure 2.8: Maximum pressure and temperature at respective barrel lengths for all times.

### 2.2.3 Transient and Axial Discretization

The calculated ballistic parameters of breech pressure, projectile travel, projectile velocity, burnt propellant fraction, and shot time are exported to Excel. The transient discretization during the shot time is limited to the output of the QuickLOAD ballistics software. For the 5.56 X 45 mm NATO M193 Ball cartridge used, the ballistics software outputs 154 time steps for the shot time of .83 milliseconds. If more resolution is need, another ballistics software or custom program can be used. The 1.28 milliseconds, and corresponding pressure decay, was discretized into 50 steps which were added to the end of the QuickLOAD data to produce the curves in Figure 2.6. After calculating the residual pressure decay, columns for projectile base pressure, mean gas pressure, and mean gas temperature are created and solved. As the spatial gas temperature is assumed to be approximately equal to the mean gas temperature, the gas properties only need to be calculated for each time step, and data for gas density, dynamic viscosity, thermal conductivity, and Prandtl Number are produced.

After calculating the gas properties, the barrel length was discretized into 16, 0.0254 m, steps. For each spatial step, an internal heat transfer coefficient, local pressure, and other necessary parameters must be calculated for each time step. The external heat transfer coefficient is assumed

to vary only spatially. For the external heat transfer coefficient, discretization was performed based on the various outer diameters along the barrel.

## 2.2.4 Calculation of Internal and External Heat Transfer Coefficients

The local internal heat transfer coefficients are calculated for each discretization. The external heat transfer coefficient is calculated separately based on outer diameter. The external heat transfer coefficient is a combination of mixed convection and radiation. Incropera et al. (2006, pg. 426) provide

$$Nu_{outer,forced} = \frac{h_{outer,forced}D_{outer}}{k_{air}} = 0.683Re_{outer,forced}^{0.466}Pr_{air}^{1/3}, \quad 2.2.7$$

for forced convection of a cylinder in horizontal flow. A.F. Mills (1995, pg. 327) calculates the Nusselt number for natural convection around a horizontal cylinder using

$$Nu_{outer,natural} = \frac{h_{outer,natural}D_{outer}}{k_{air}}, \quad 2.2.8$$

$$Nu_{outer,natural} = \left\{ 0.6 + 0.387 \left[ Ra_{D_{outer}} / \left( [1 + (0.559/Pr_{air})^{9/16}]^{16/9} \right) \right]^{1/6} \right\}^2, \quad 2.2.9$$

where the Reynolds Number, Raleigh Number, and Prandtl Number are found using

$$Re_{outer,forced} = \frac{\rho_{air}u_{air}D_{outer}}{\mu_{air}} \text{ for } 40 < Re_{outer,forced} < 4000, \quad 2.2.10$$

$$Ra_{D_{outer}} = \frac{g\beta_{outer}(T_{outer} - T_{air})D_{outer}^3}{\alpha_{air}\nu_{air}}, \quad 2.2.11$$

$$Pr_{air} = \frac{\nu_{air}}{\alpha_{air}} = \frac{\mu_{air}C_{p,air}}{k_{air}}. \quad 2.2.12$$

The outer external heat transfer coefficient is found by arranging equations 2.2.7 to 2.2.9 to solve for the heat transfer coefficient ( $h$ ) and adding an effective radiative heat transfer coefficient. Incropera et al. (2006, pg. 594) provide the correlation for mixed convection in the form

$$h_{outer,mixed} = (h_{outer,forced}^N + h_{outer,natural}^N)^{1/N}. \quad 2.2.13$$

Siebers et al. (1983, pg. XX) use  $N = 3.2$  for a vertical cylinder in horizontal flow, and Incropera et al. (2006, pg. 594) suggest values of  $N$  between 3 and 4. Kreith et al. (2011, pg. 610-611) provide an effective radiative heat transfer coefficient,

$$h_{outer,rad} = \frac{\zeta\omega(T_{outer}^4 - T_{air}^4)}{T_{outer} - T_{air}}, \quad 2.2.14$$

that can be combined with  $h_{outer,mixed}$  using

$$h_{outer} = h_{outer,mixed} + h_{outer,rad}. \quad 2.2.15$$

to provide the outer heat transfer coefficient. For simplicity, if the diameters are similar, an average outer heat transfer coefficient can be used.

The internal heat transfer coefficient is calculated using the following equations from Appendix II in *Internal Ballistics*, viz. the heat transfer coefficient is found using Reynolds analogy for momentum and heat transfer in turbulent flow with a correction for Prandtl numbers not equal to unity (Hunt, 1951, pg. 276-277), i.e.

$$h_{gas} = \frac{\rho_{gas} C_{p,gas} u_{gas}}{\phi \eta_{gas}^{1/\psi} [\phi \eta_{gas}^{1/\psi} - F(Pr_{gas})]}, \quad 2.2.16$$

$$F(Pr_{gas}) = -5\{(Pr_{gas} - 1) + \ln[1 + 0.83(Pr_{gas} - 1)]\}. \quad 2.2.17$$

The boundary layer flow is assumed to be to be two-dimensional flow of a viscous incompressible fluid along a plane wall, which is valid if the thickness of the boundary layer is significantly smaller than the bore diameter (Hunt, 1951, pg. 274-275). Hunt (1951, pg. 275) provides the boundary layer velocity distribution in terms of main-stream velocity in the form

$$u_{gas} = v_0 \varphi(\eta_{gas}), \quad 2.2.18$$

$$u_{gas} = \frac{x}{X} u_{projectile}, \quad 2.2.19$$

$$\varphi(\eta_{gas}) = \phi \eta_{gas}^{1/\psi}, \text{ with } \phi = 12.4 \text{ and } \psi = 11.3, \quad 2.2.20$$

$$\vartheta_0 = \sqrt{\frac{\tau_w}{\rho_{gas}}}, \quad 2.2.21$$

$$\eta_{gas} = \frac{\vartheta_0 \delta}{v}, \quad 2.2.22$$

$$\rho_{gas,mean} = \frac{m_{gas}}{V - [(w - m_{gas})/\rho_{propellant}]} = \frac{P_{gas,mean}}{RT_{gas,mean}}. \quad 2.2.23$$

Hunt (1951, pg. 276) provides the solution to the momentum integral as

$$\eta^{1+3/\psi} = \frac{\Psi(t) Re_{gas}}{\phi^3} \text{ with } \Psi(t) = 5, \quad 2.2.24$$

where the Reynolds number and shear stress at the bore wall are given by

$$Re_{gas} = \frac{\rho_{gas} u_{gas} x}{\mu_{gas}}, \quad 2.2.25$$

and

$$\tau_w = \frac{\rho_{gas} u_{gas}^2}{\phi^2 \eta^{2/\psi}}. \quad 2.2.26$$

The forced convection from the ballistic cycle evolves to mixed convection as the residual pressure converges to ambient pressure. During this time, the barrel is exhausting the last of the propellant gas and is filling with ambient air. A fraction of the propellant gas may be not exhausted and may become part of the back flow. For simplicity, this mixture is assumed to have the properties of air. The heat transfer coefficient for this period of cooling between consecutive shots

is that of natural convection from the underside of an isothermal flat plate. Kreith and Bohn (2011, pg. 311) calculate the Nusselt number for natural convection from the underside of an isothermal flat plate as

$$Nu_{inner,L} = \frac{h_{inner}L_{char}}{k_{air}} = 0.27(Ra_{inner,L})^{1/4}, \quad 2.2.27$$

$$Gr_{inner,L} = \left[ \frac{g\beta_{inner}(T_{inner} - T_{air})L_{char}^3}{v_{air}^2} \right], \quad 2.2.28$$

$$Ra_{inner,L} = Gr_{inner,L}Pr_{air}, \quad 2.2.29$$

$$L_{char} = \frac{A_{surf,inner}}{Per}. \quad 2.2.30$$

This appears to be a reasonable assumption due to the ambient air's velocity distribution in the barrel being relatively low compared to that of the ballistic cycle and bore diameter.

### 2.2.5 Specification of Firing Schedule, Initial Barrel Temperature, and Ambient Conditions

Firing schedules, initial barrel temperature, and ambient conditions are specified to match as closely as possible to the experiments performed. To specify a firing schedule in a format that ANSYS is capable of simulating, a separate Excel tab was created using the format in Table 2.1. Value look-up functions are used to reference the transient and axial discretization of the internal heat transfer coefficient, mean gas temperature, and local gas pressure.

The parameters for the firing time, time between consecutive shots, burst time, and cooling time between bursts are known. The firing time is known from the ballistics software. The time between consecutive shots is determined from the average fire rate and firing time. The burst time can then be calculated using the number of shots fired, and the cooling time between bursts can be specified as desired.

At this point, further discretization can be done to improve simulation run times. Columns for the axial discretization are created. Using the times calculated for the firing schedule and user

specified time steps, rows are used to create transient stages of the firing schedule. This table must be replicated to reference the internal heat transfer coefficient, mean gas temperature, and local gas pressure. Using these tables, the columns for time and axial location can be copied into ANSYS.

Table 2.1: Example layout of firing schedule tables.

(Reference)	Time (seconds)	Axial Location	
		X-1	X-2 ...
<b>Burst Time</b>	Firing time	Internal heat transfer coefficient, mean gas temperature, or local pressure	Internal heat transfer coefficient, mean gas temperature, or local pressure
	Time between consecutive shots		
Firing time			
Time between consecutive shots			
<b>Cooling time between bursts</b>			
<b>Burst Time</b>	Firing time		
	Time between consecutive shots		

### 2.2.6 Barrel Geometry Implementation in ANSYS

The material information and barrel geometry need to be created in ANSYS by adding the modules shown in Figure 2.9.

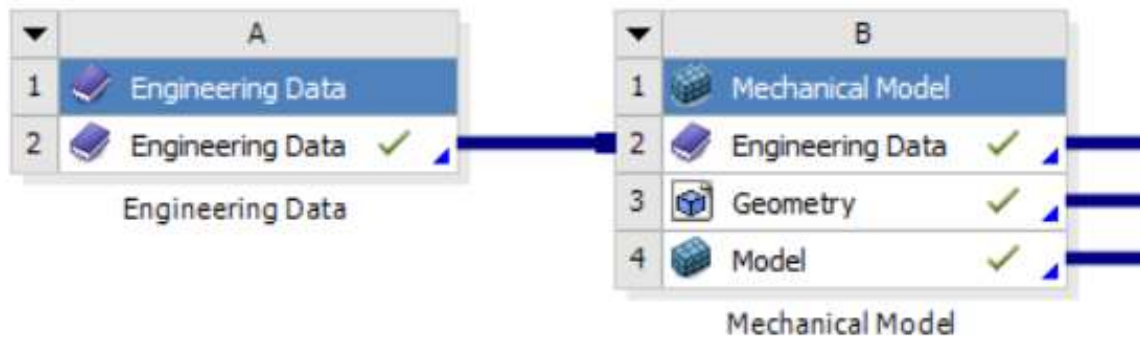


Figure 2.9: Analysis setup in ANSYS Workbench.

The engineering data module is where the material properties can be specified, this information is then input into the mechanical model. The barrel geometry is imported into ANSYS from SolidWorks directly. The mechanical model module is the preprocessing for any further analysis. This module is where the coordinate system, material, and mesh parameters are defined for the imported geometry. The user interface for geometry meshing is shown in Figure 2.10, with the corresponding generated mesh shown in Figure 2.11.

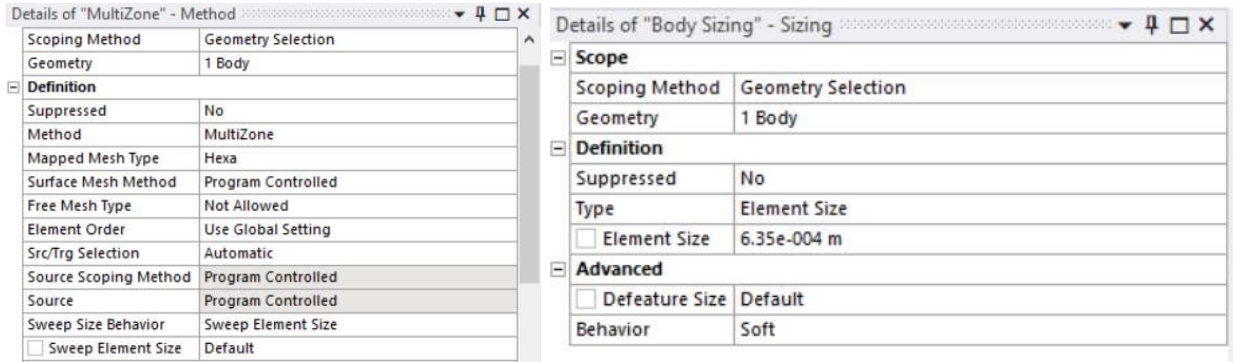


Figure 2.10: Mesh details.

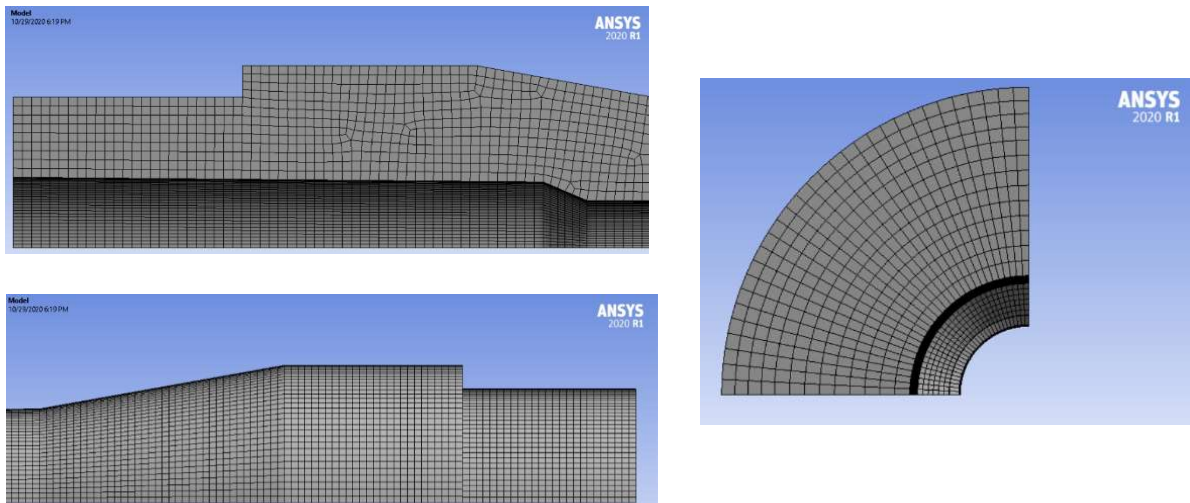


Figure 2.11: Generated axial and radial mesh distribution.

## 2.2.7 Application of Governing Equations in ANSYS

### 2.2.7.1 ANSYS Transient Thermal Analysis

By using the “Mechanical Model” module for preprocessing, multiple simulation modules can be attached to the same mesh. Figure 2.12 shows the first transient thermal analysis attached to the mechanical model.

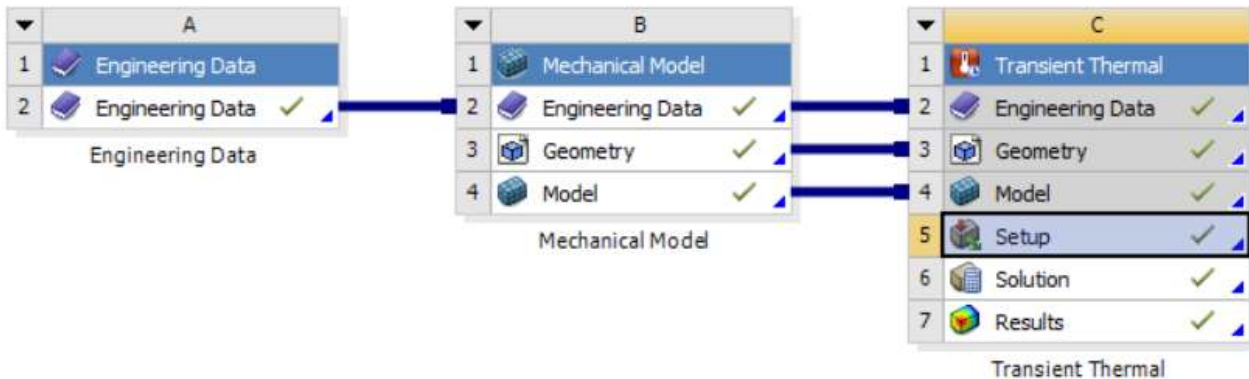


Figure 2.12: ANSYS Workbench transient thermal analysis.

After creating the transient thermal analysis, the analysis time and initial temperature are defined using the drop-down tree shown in Figure 2.13. Figure 2.14 displays the transient discretization of the firing schedule, from Excel, imported into ANSYS and corresponding time step settings. The analysis settings in ANSYS allow for further discretization by using substeps. Substeps can be defined using time or number of substeps.

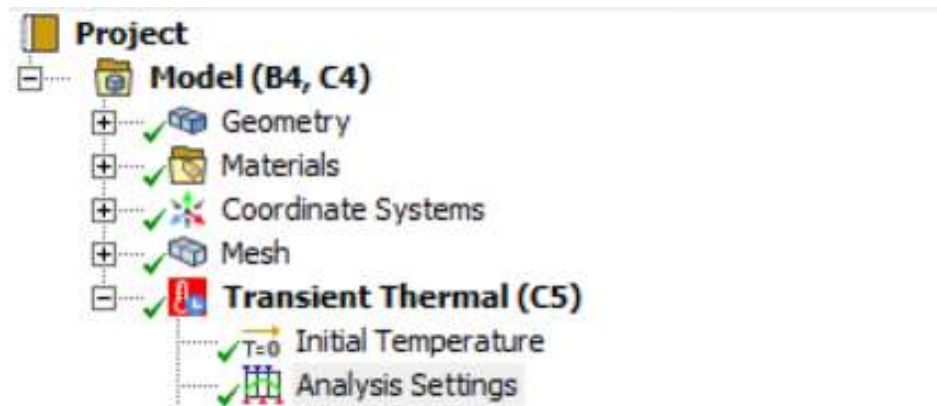


Figure 2.13: Transient thermal analysis setup.

Figures 2.15 and 2.16 show the convection and temperature load matrices applied to faces on the barrel geometry according to the axial discretization.

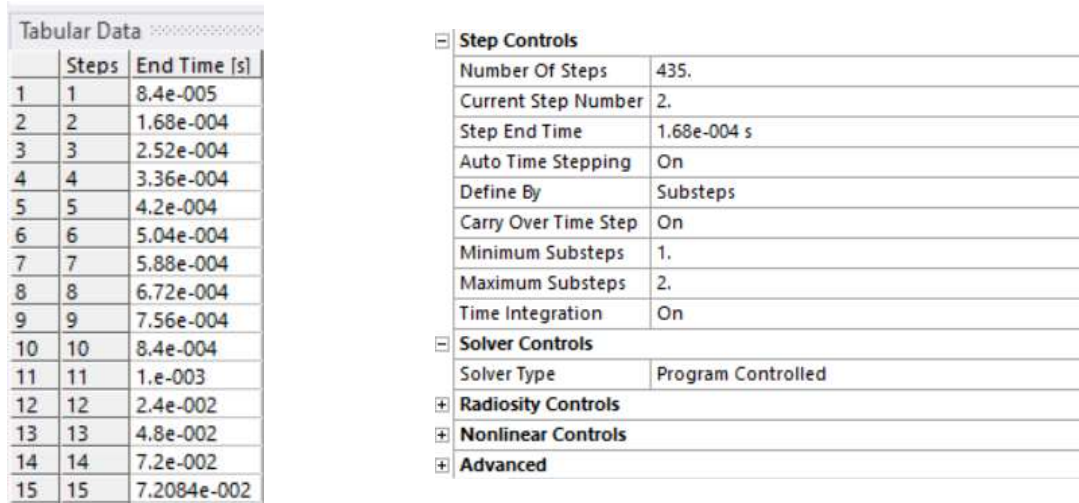


Figure 2.14: Analysis Settings and Time Steps.

Application of the boundary conditions in ANSYS requires selecting the surface and specifying the desired boundary condition from the tool bar. Figure 2.15 displays convection and radiation loads applied to the external surfaces. The user interfaces for the various boundary condition loads are shown in Figure 2.18.

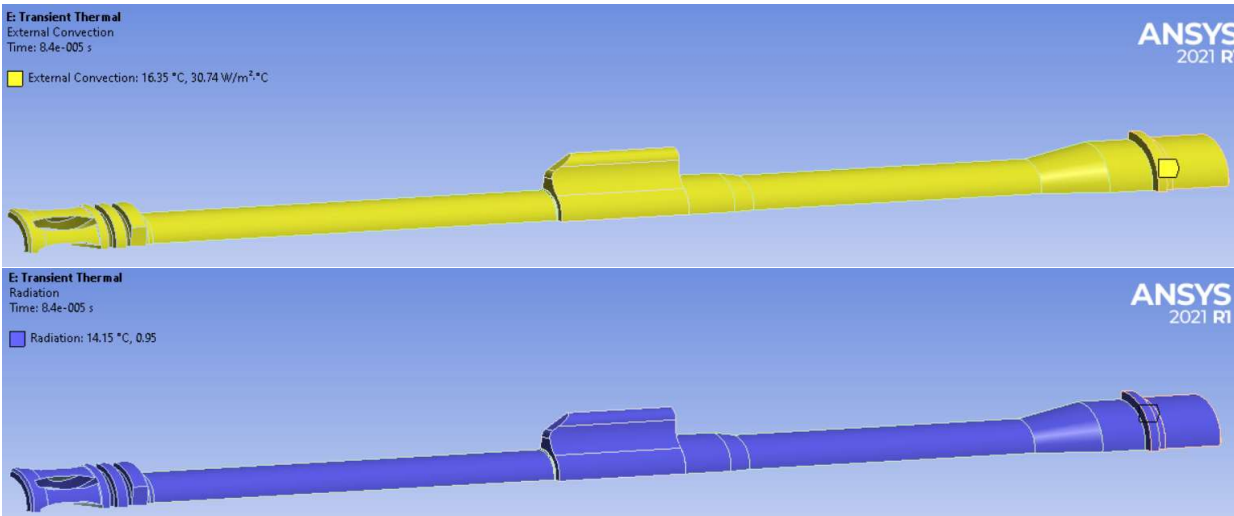


Figure 2.15: External convection and radiation boundary condition.

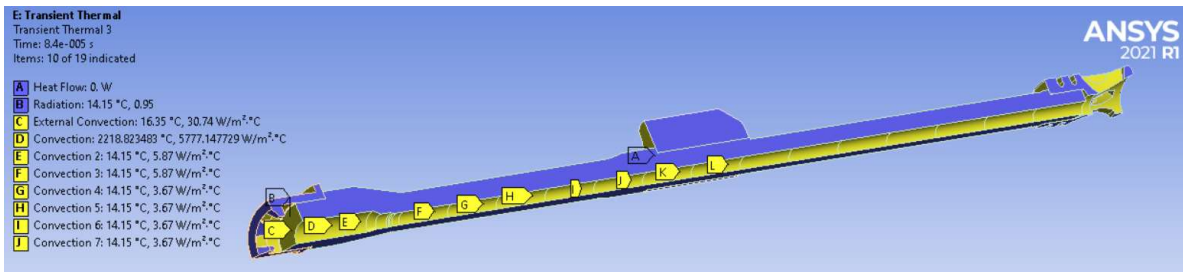


Figure 2.16: Barrel with internal and sectioning boundary conditions applied.

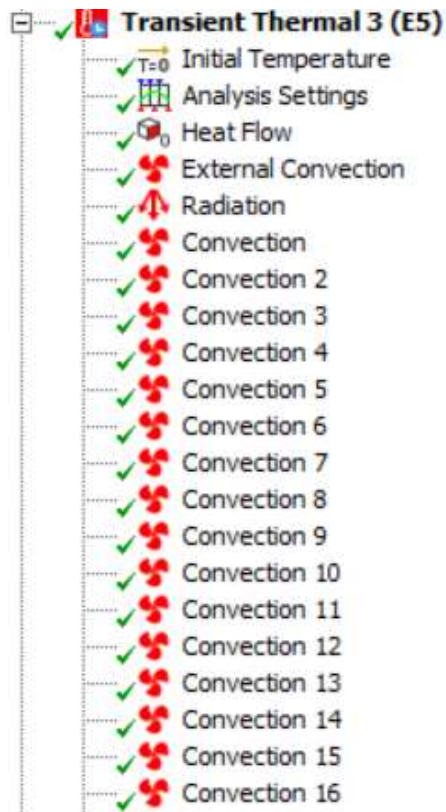


Figure 2.17: Transient Thermal Analysis simulation loads.

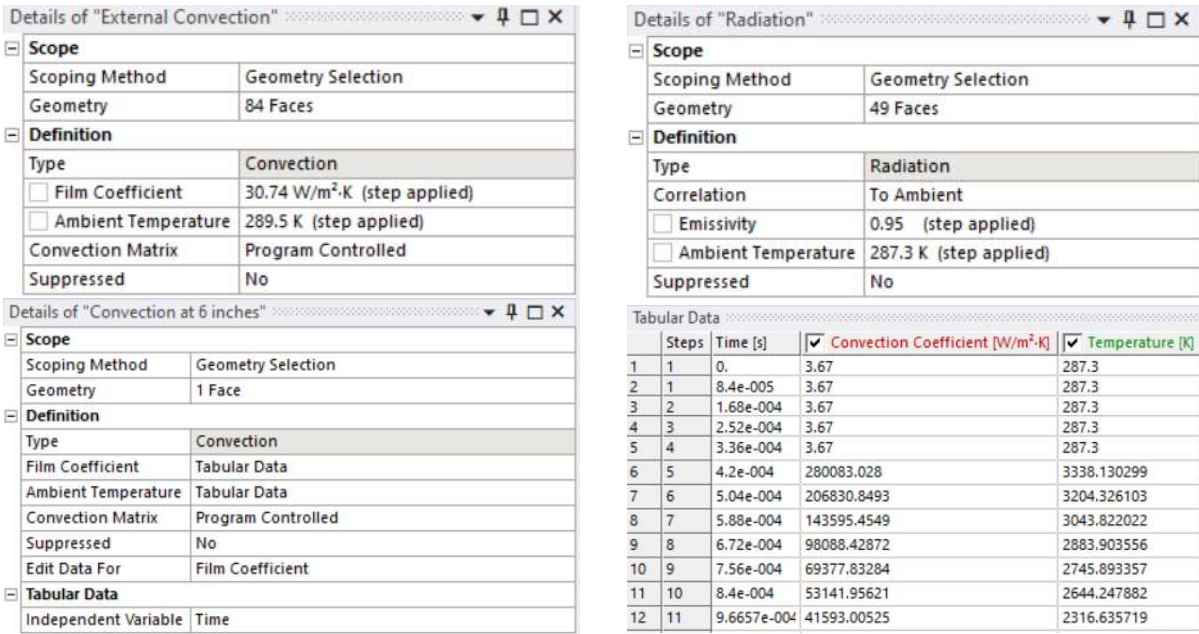


Figure 2.18: Various Boundary Condition Settings.

### 2.2.7.2 ANSYS Static Structural Analysis

ANSYS Static Structural Analysis can be directly coupled with ANSYS Transient Thermal Analysis. This is accomplished by dragging and dropping the Static Structural Analysis onto the solution of the Transient Thermal Analysis, as shown in Figure 2.19.

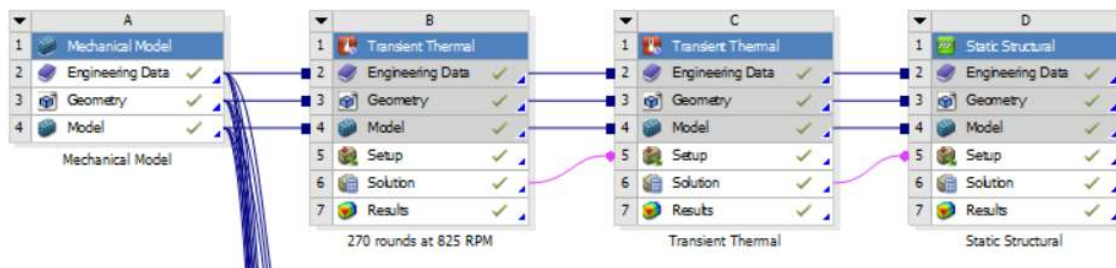


Figure 2.19: Workbench setup for coupling Transient Thermal and Static Structural Analysis.

However, the time steps and analysis settings must be the same between the two simulations. To reduce unnecessary data and long simulation times, a single shot transient thermal simulation is performed after a specified number of cartridges fired. The static structural simulation is then attached to the single shot transient thermal simulation. For example, Figure 2.19 shows the

coupled thermo-elastic stress simulation of the 271<sup>st</sup> cartridge fired. Figure 2.20 shows the transient thermal solution imported into the static structural simulation.

Details of "Imported Body Temperature"	
<b>Scope</b>	
Scoping Method	Geometry Selection
Geometry	3 Bodies
<b>Definition</b>	
Type	Imported Body Temperature
Tabular Loading	Program Controlled
Suppressed	No
Source Environment	Transient Thermal 4 (C5)
Source Time	All
<b>Graphics Controls</b>	
By	Active Row
Active Row	1

Figure 2.20: Analysis settings and imported body temperature interface.

The imported load settings must be changed by selecting “All” for the “Source Time.” After the temperature distribution for each time step has been imported, the local pressure loadings and frictionless supports shown in Figure 2.21 are applied.

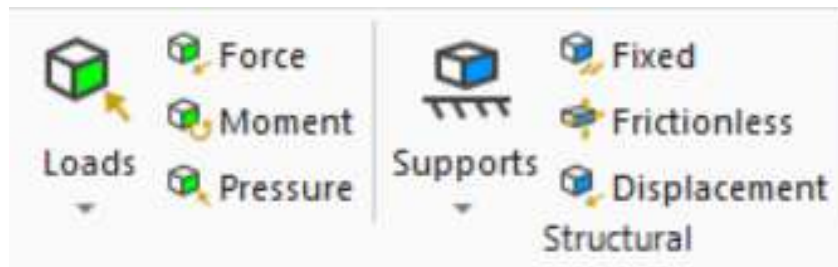


Figure 2.21: Static Structural Analysis loads and boundary conditions.

At this point, either the spatial local maximum pressure can be applied to the entire bore, or a transient local pressure curve can be applied corresponding to the axial discretization used in the transient thermal analysis. Using the spatial local maximum is convenient for design purposes and quick barrel failure checks. Using the transient local pressure for each axial step, as shown in Figures 2.22 and 2.23, is more accurate to the physical phenomena occurring in the barrel.

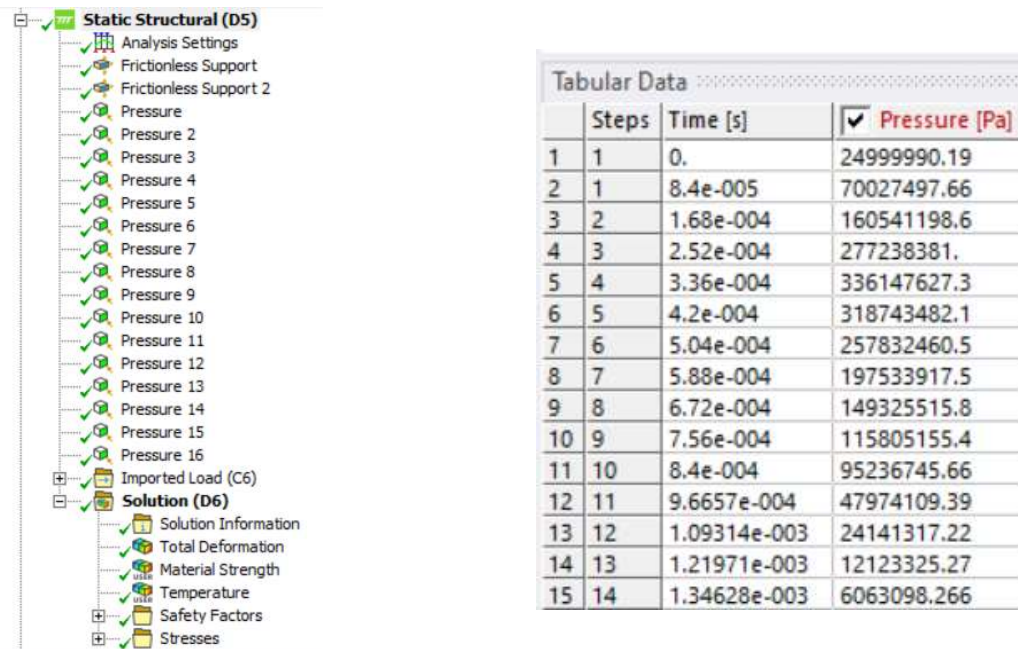


Figure 2.22: Applied loads and boundaries for Static Structural Analysis.

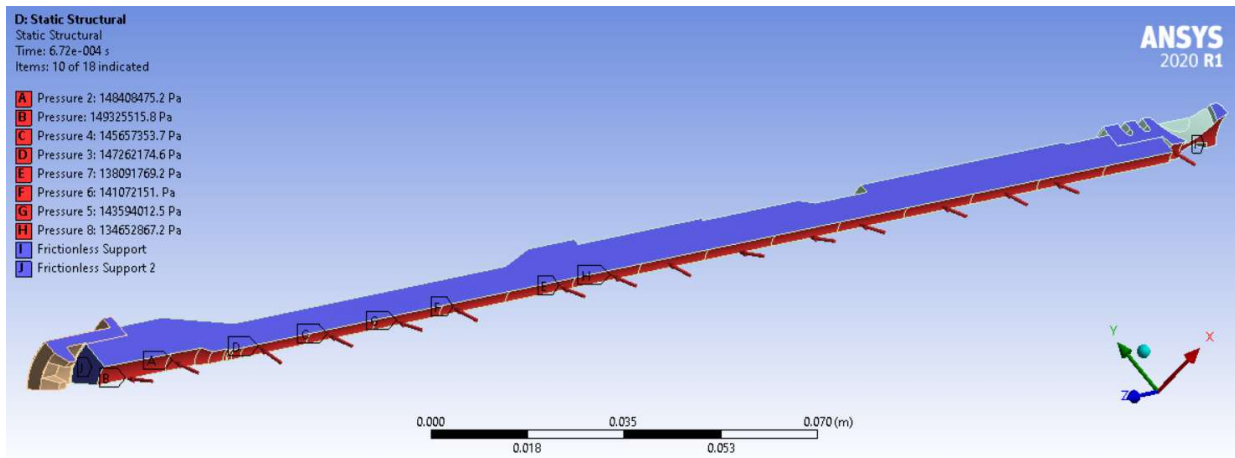


Figure 2.23: Static Structural loads and boundaries applied to barrel geometry.

Frictionless boundary conditions are placed on the sectioning cuts and breech surface. The material strength must be specified for each node by using a “User Defined Result” as shown in Figure 2.24. Figure 2.25 shows the user interface for defining the relationship between the material strength and temperature. Finally, the safety factors can be found by creating another “User Defined Result”.



Figure 2.24: Static Structural Analysis solutions tab.

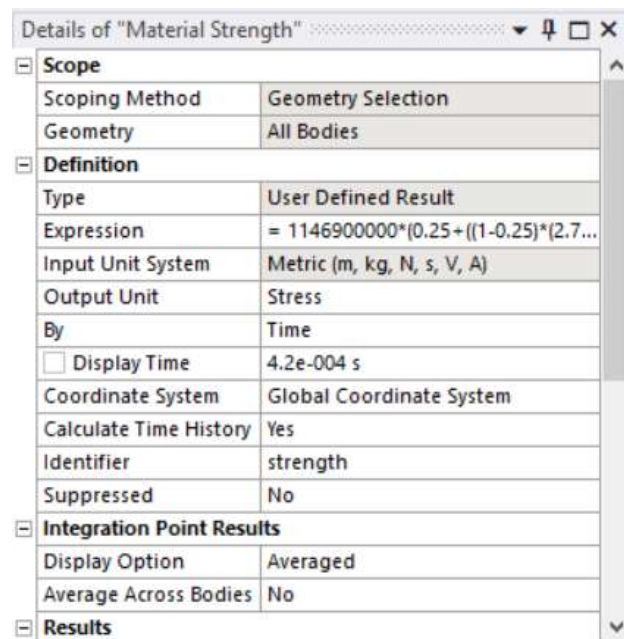


Figure 2.25: User defined material strength function.

### 3 EXPERIMENT APPARATUS AND PROCEDURE

Validating the model requires comparing simulation results to data collected by experiments. To validate the model's ability to predict the transient temperature distribution, four experiments are performed using an AR-15 rifle with different firing schedules. The experiments provide data on the transient external temperature distribution. To validate the thermo-elastic stress, Windham (1994 and 1996) provides data on the transient external temperature distribution, number of rounds until failure, and location of the failure. Due to the danger and cost of destructive testing, Windham's (1994 and 1996) data is used.

Experiment 1: 30 rounds, semi-automatic

Experiment 2: 60 rounds, fully automatic

Experiment 3: 90 rounds, fully automatic

Experiment 4: 90 rounds, fully automatic

Experiment 1 is performed to provide insight into the effects of fire mode, fire rate, and external mixed convection on barrel temperatures. The following experiments provide insight into the effects of cooling time between bursts, variations in cyclic rate of fire, and number of rounds fired on barrel temperatures. The firing schedules for each experiment are relatively intense for the fire mode. This is done to create a larger temperature change between initial and final temperatures and bore and external temperatures.

The data is statistically analyzed for repeatability by evaluating the external barrel temperature for a specific number of cartridges fired. Analyzing the data in this way correlates the barrel temperature to energy input.

This chapter describes the experiment apparatus and procedure used to gather transient temperature data about the AR-15 barrel. The transient temperature data from each experiment is used to validate the modeling and simulation method. Validation of the fourth experiment is presented in Chapter 4, while the other experiments are presented in Appendix I.

## 3.1 Apparatus and Procedure

### 3.1.1 Apparatus

The test facilities used for the experiments are an outdoor private shooting range and an indoor shooting trap provided by OOW. The outdoor range providing results with mixed convective cooling and the indoor shooting trap providing primarily natural convective cooling.

Figure 3.1 shows the equipment used and the setup for the first experiment. The list of equipment used to obtain data is listed below:

1. FLIR-E8 XT thermal camera
2. Thermocouples with digital display
3. Laptop with FLIR Thermal Studios software
4. Shot trap
5. Shooting range with a lead sled
6. Air speed indicator
7. Thermometer with hydrometer (humidity gage)
8. Go – Pro Camera
9. AR-15 Rifle
10. M4 Carbine

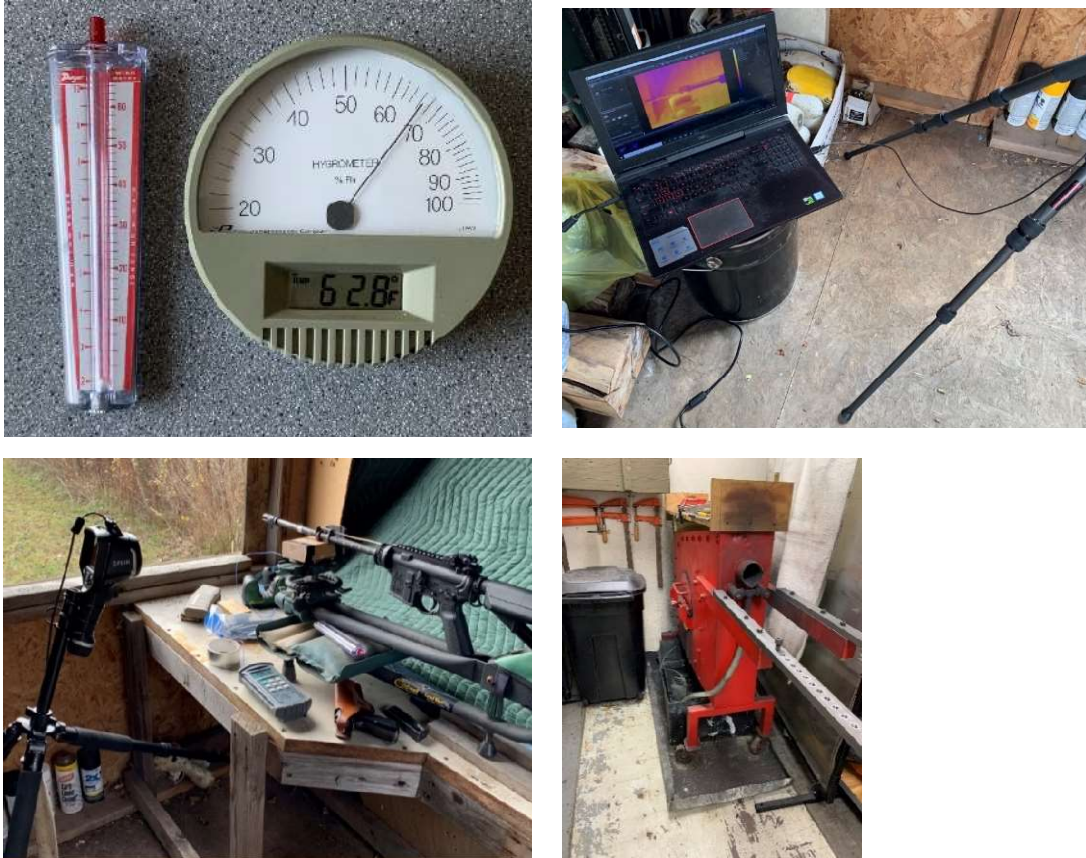


Figure 3.1: Experiment apparatus.

### 3.1.2 Procedure

The handguard of the test weapon is removed before placing the weapon into the mount. For the fully-automatic experiments, the upper receiver of the test weapon is transferred onto a post-sample M4 lower receiver provided by OOW. With the weapon secured in the mount, the FLIR E8-XT thermal camera is clamped into a tripod. The camera is positioned to allow for a complete view of the barrel. The temperature range of the thermal camera is changed to 283.1 K to 823.2 K. The thermal camera is plugged into a laptop to utilize the video recording capabilities of the FLIR Thermal Studios software. Thermocouples are attached to the barrel to measure the initial body temperature. Using the thermometer and anemometer, the ambient temperature and wind speed are measured. The distance to from the thermal camera to the barrel is measured using a tape measure. The initial data is input into the Thermal Studios Software using the user interface shown in Figure 3.2. Magazines are loaded in accordance with the firing schedule of the experiment and

staged for easy access. The thermal camera recording is started, and firing commenced in accordance with the firing schedule of each experiment.

Parameters		
Emissivity	0.95	
Reflected temp.	289.3	K
Distance	2.0	ft
Atmospheric temp.	289.3	K
Ext. optics temp.	289.3	K
Ext. optics trans.	1.0	
Relative humidity	61.0	%
Reference temp.	0.0	K

Figure 3.2: Input parameters for the FLIR E8-XT thermal camera.

## 3.2 Experiments

### 3.2.1 Measurement and Data Collection

Processing the data requires placing temperature measurement markers along the length of the barrel. Physical markers on the barrel remain visible in the thermal viewer, however the measurement markers could not track the physical markers. During firing this was not an issue, as the weapon is held rigidly in a mount. Complications arise during reloads, when the weapon needs to be removed slightly from the fixture to allow for the magazine to be change. This movement requires manual alignment of markers, and thus less frames were processed during these periods.

Two types of gas blocks are used for the experiments and are shown in Figures 3.3 and 3.4. The first type is used only for Experiment 1, while the second type is used for Experiments 2 – 4. The gas block is changed to evaluate the effect of the different barrel attachments on the heat transfer from the gas port. The gas block is also changed to create a larger heat sink for the fully – automatic experiments. The thermal camera video shows that the conduction to the gas block from the gas port is significant.

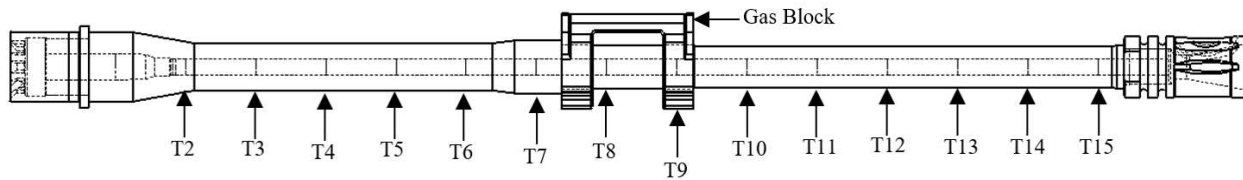


Figure 3.3: Barrel type 1 used in experiment 1.

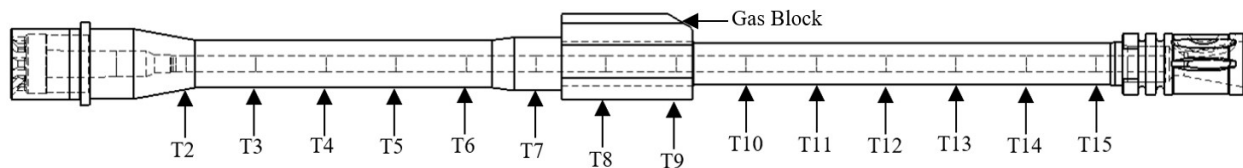


Figure 3.4: Barrel type 2 used in experiments 2 – 4.

### 3.2.2 Experiment 1

The first experiment performed was one 30 – round magazine fired semi – automatic as fast as possible. Table 3.1 provides the ambient conditions and firing schedule. The experiment location was at a private outdoor range. A heavy lead sled mount was used to keep the rifle steady during firing. Figures 3.5 shows the propellant gas being vented from the barrel into the gas tube. The gas port is located 0.1945 m from the breech. Figure 3.6 shows the temperature distribution after firing has finished.

Table 3.1: Experiment 1 information and ambient conditions.

Date:	11/08/2020	
Ambient Temperature:	296.6	<i>K</i>
Emissivity:	0.95	<i>ul</i>
Relative Humidity:	56%	<i>ul</i>
Maximum Air Velocity:	2.24	<i>m/s</i>
Minimum Air Velocity:	.89	<i>m/s</i>
Average Air Velocity:	1.57	<i>m/s</i>
Fire Mode:	Semi-automatic	<i>ul</i>
Fire Rate:	290	<i>rpm</i>
Reload Rate, Average:	N / A	<i>s</i>
Cartridges Fired:	30	<i>rounds</i>
Barrel:	Type 1	<i>ul</i>

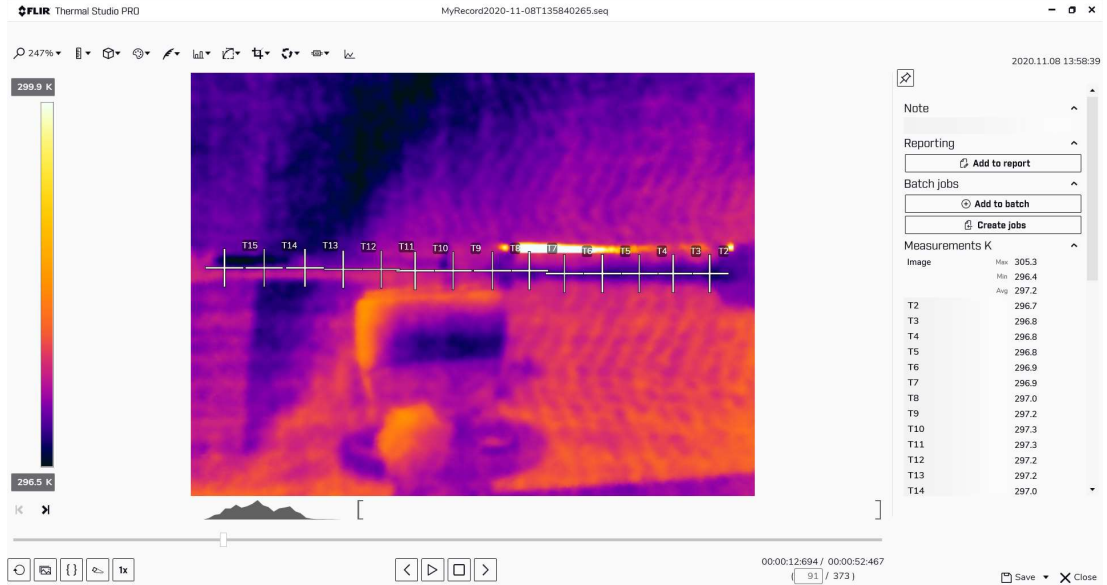


Figure 3.5: Experiment #1, first shot.

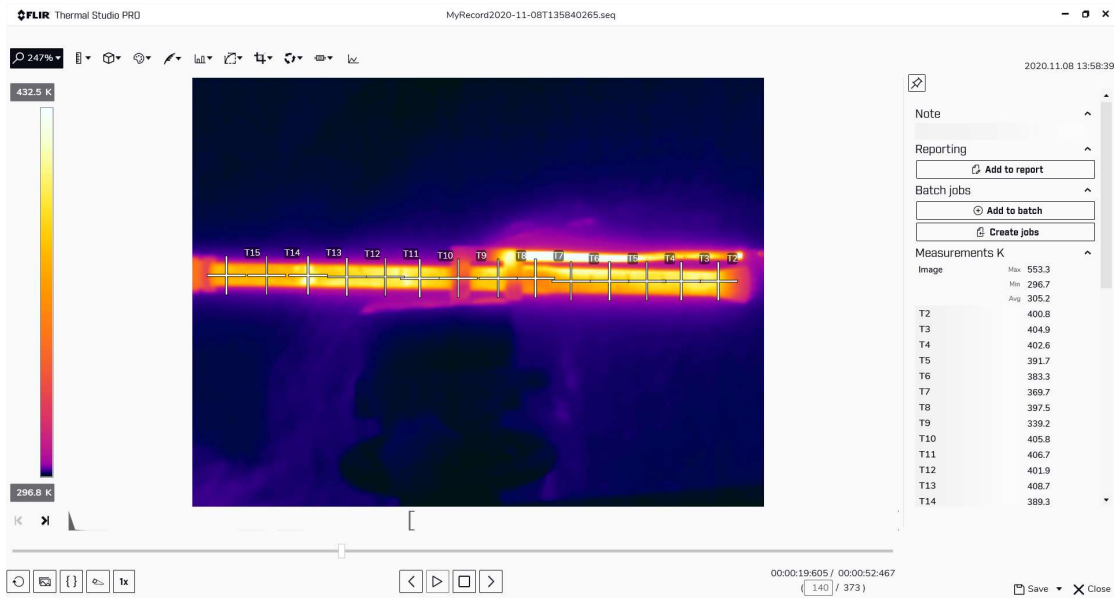


Figure 3.6: Experiment #1, external barrel temperature at 19.605 seconds.

### 3.2.3 Experiment 2

The firing schedule for the second experiment is shown in Table 3.2. This experiment uses an M4 Carbine lower receiver, instead of the semi – automatic only AR-15 receiver. The experiment was performed at Ohio Ordnance Works in an indoor setting. The weapon was placed

in a fixture and fired into a shot trap. There is a 15 second gap in data due to the operator removing the weapon from the fixture and laying the weapon on its side, shown in Figure 3.7. The correct orientation to capture data during cooling is shown in Figure 3.8.

Table 3.2: Experiment 2 information and ambient conditions

Date:	01/25/2021	
Ambient Temperature:	293.1	<i>K</i>
Emissivity:	0.95	<i>ul</i>
Relative Humidity:	51%	<i>ul</i>
Maximum Air Velocity:	N / A	<i>m/s</i>
Minimum Air Velocity:	N / A	<i>m/s</i>
Average Air Velocity:	N / A	<i>m/s</i>
Fire Mode:	Fully automatic	<i>ul</i>
Fire Rate:	918	<i>rpm</i>
Reload Rate, Average:	7.7	<i>s</i>
Cartridges Fired:	60	<i>rounds</i>
Barrel:	Type 2	<i>ul</i>

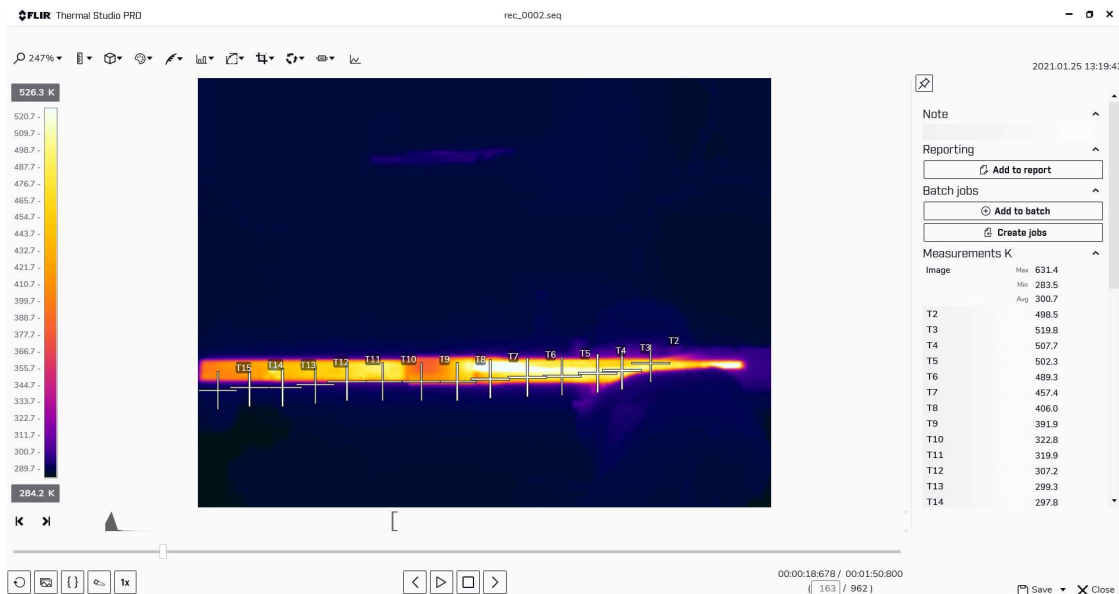


Figure 3.7: Experiment #2 Error, weapon laid on its side during cooling.

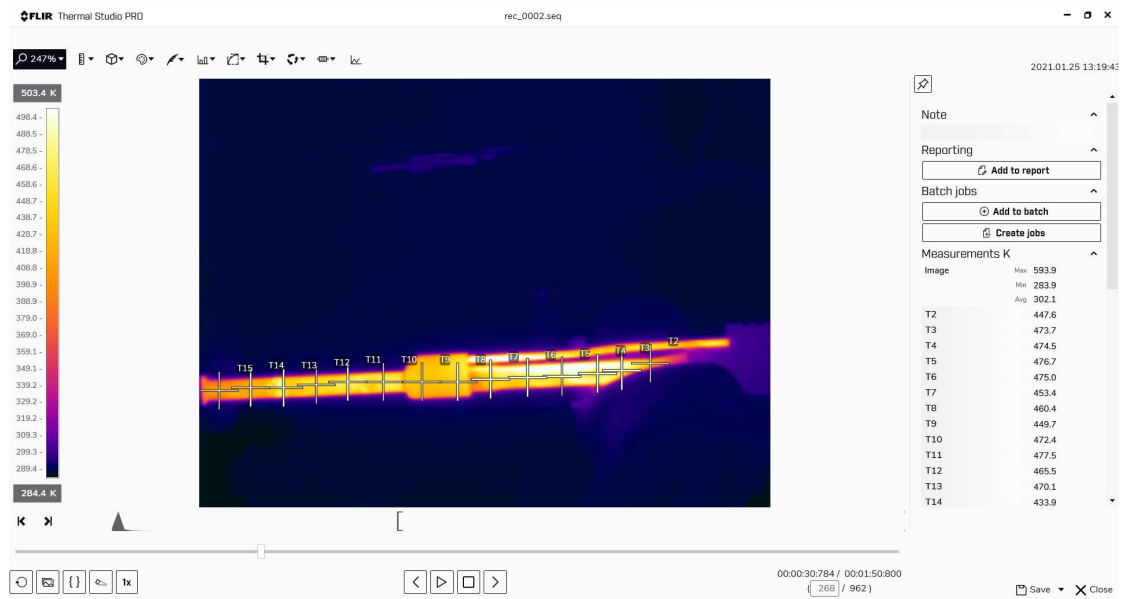


Figure 3.8: Experiment #2, weapon orientation corrected.

### 3.2.4 Experiment 3

Table 3.3 displays the ambient conditions and firing schedule for the third experiment. This experiment is performed at Ohio Ordnance Works using an indoor shot trap. This experiment uses the fully automatic M4 Carbine lower receiver provided by OOW.

Table 3.3: Experiment 3 information and ambient conditions.

Date:	02/05/2021	
Ambient Temperature:	289	<i>K</i>
Emissivity:	0.95	<i>ul</i>
Relative Humidity:	53%	<i>ul</i>
Maximum Air Velocity:	N / A	<i>m/s</i>
Minimum Air Velocity:	N / A	<i>m/s</i>
Average Air Velocity:	N / A	<i>m/s</i>
Fire Mode:	Fully automatic	<i>ul</i>
Fire Rate:	924	<i>rpm</i>
Reload Rate, Average:	11.2	<i>s</i>
Cartridges Fired:	90	<i>rounds</i>
Barrel:	Type 2	<i>ul</i>

Image information	
Camera model	FLIR E8xt Wifi
Camera serial	639097938
Lens	FOL7
Filter	
Resolution	320 x 240
File size	808090.7 KB
Created	2021.02.05 12:43:56
Modified	2021.02.28 21:54:13
Range max.	523.2 K
Range min.	253.1 K

Figure 3.9: Experiment #3 error, thermal camera set to incorrect temperature range.

In this experiment, the thermal camera temperature range was not set prior to recording, as shown in Figure 3.9. After 90 rounds had been fired, this error resulted in several locations along the barrel surpassing the temperature scale and remaining at a constant temperature. Due to this error, only the data up to 61 rounds could be confidently evaluated. The proper camera setting is shown in Figure 3.10, which was used on all other experiments.

Image information	
Camera model	FLIR E8xt Wifi
Camera serial	639097938
Lens	FOL7
Filter	
Resolution	320 x 240
File size	1150198.6 KB
Created	2021.02.20 18:40:26
Modified	2021.03.09 14:30:31
Range max.	823.2 K
Range min.	283.1 K

Figure 3.10: Experiment #4, thermal camera set to correct temperature range.

### 3.2.5 Experiment 4

Table 3.4 shows the ambient conditions and firing schedule for the fourth experiment. This experiment is performed at OOW using the indoor shot trap and M4 Carbine lower receiver. Experiment 4 is a reshoot of the firing schedule in experiment 3. Figure 3.11 and Figure 3.12 show the temperature distribution after the first and last shot, respectively.

Table 3.4: Experiment 4 information and ambient conditions.

Date:	02/20/2021	
Ambient Temperature:	289.3	<i>K</i>
Emissivity:	0.95	<i>ul</i>
Relative Humidity:	61%	<i>ul</i>
Maximum Air Velocity:	N / A	<i>m/s</i>
Minimum Air Velocity:	N / A	<i>m/s</i>
Average Air Velocity:	N / A	<i>m/s</i>
Fire Mode:	Fully automatic	<i>ul</i>
Fire Rate:	943	<i>rpm</i>
Reload Rate, Average:	8.5	<i>s</i>
Cartridges Fired:	90	<i>rounds</i>
Barrel:	Type 2	<i>ul</i>



Figure 3.11: Experiment #4, first shot.

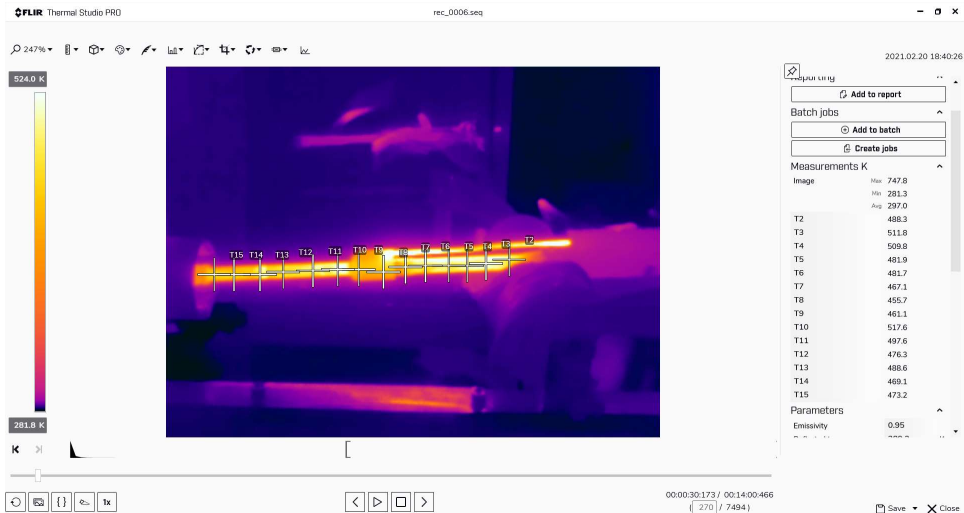


Figure 3.12: Experiment #4, external barrel temperature at 30.173 seconds.

### 3.3 Data Reduction and Sample Results

#### 3.3.1 Data Reduction

The FLIR Thermal Studio software records the experiment in video format at a frame rate of 60 frames per second. The temperature measurement nodes placed within the video viewer can export data directly to Excel in CSV format. CSV files of the full experiment videos were exported to excel. As stated above, the software measurement nodes cannot track the physical object in the video viewer. Therefore, when the weapon was moving significantly from its mount during reloading, separate CSV files needed to be used to fill in the corresponding gaps in the full CSV file. Some frames required manual tracking, frame-by-frame, of the physical marker and measurement marker. The files include camera settings, frame numbers, time, and temperature readings.

#### 3.3.2 Sample Results

Figure 3.13 through 3.15 present the data in a simplified manner. The axial temperature distribution is displayed corresponding to the number of shots fired, instead of in seconds. Presenting the data in terms of the number of shots fired is analogous to the transient energy transferred to the barrel. This method of data presentation was chosen due to the variability of fire rates for the experiments.

Appendix G presents the transient temperature data from the temperature measurement nodes. Comparing the experiment results, the higher fire rate of fully automatic fire results in higher external temperatures at a given time. However, the semi-automatic firing schedule produced higher external temperature at a given cartridge fired due to more conduction time. There was no significant difference in maximum external barrel temperature for the experiments performed. For all experiments, maximum external barrel temperatures occur momentarily after firing has finished.

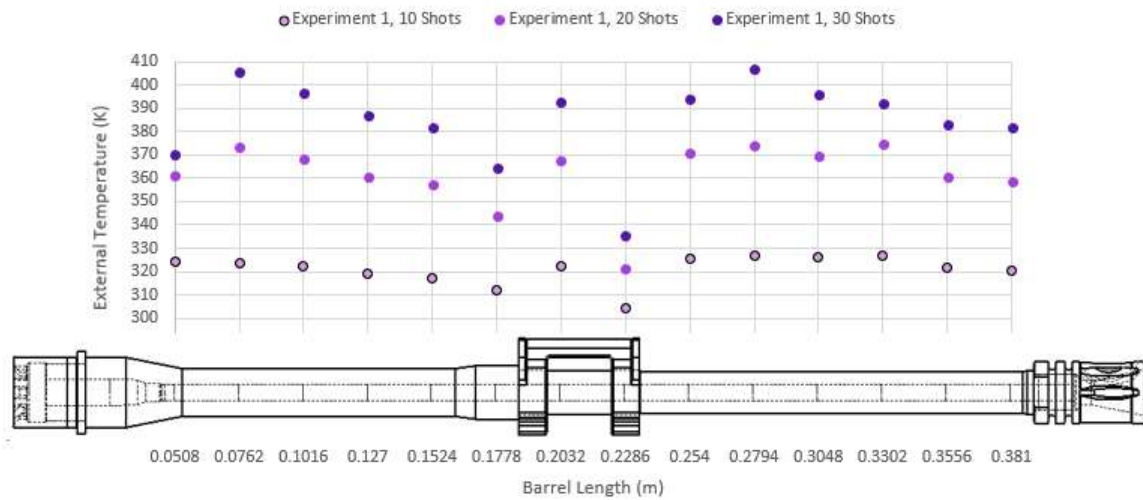


Figure 3.13: Axial Temperature Distribution at 10, 20, and 30 Rounds Fired for Barrel Type 1.

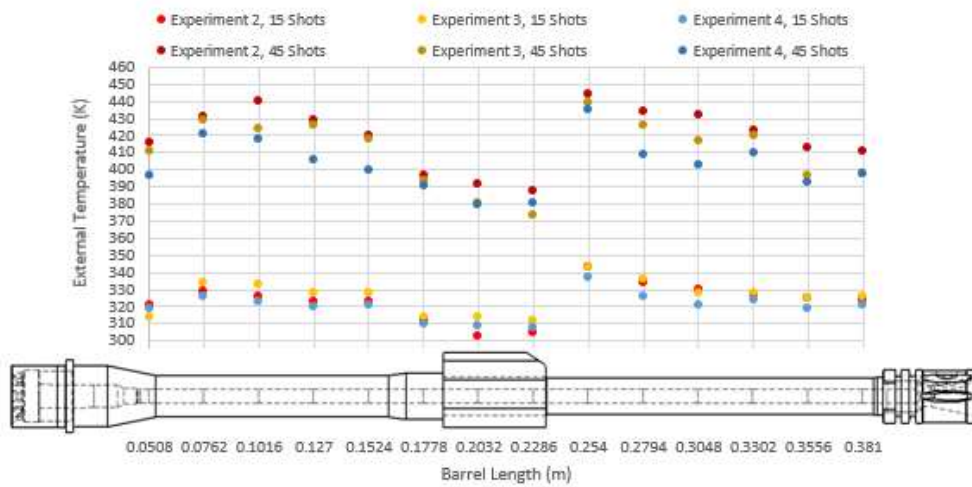


Figure 3.14: Axial Temperature Distribution at 15 and 45 Rounds Fired for Barrel Type 2.

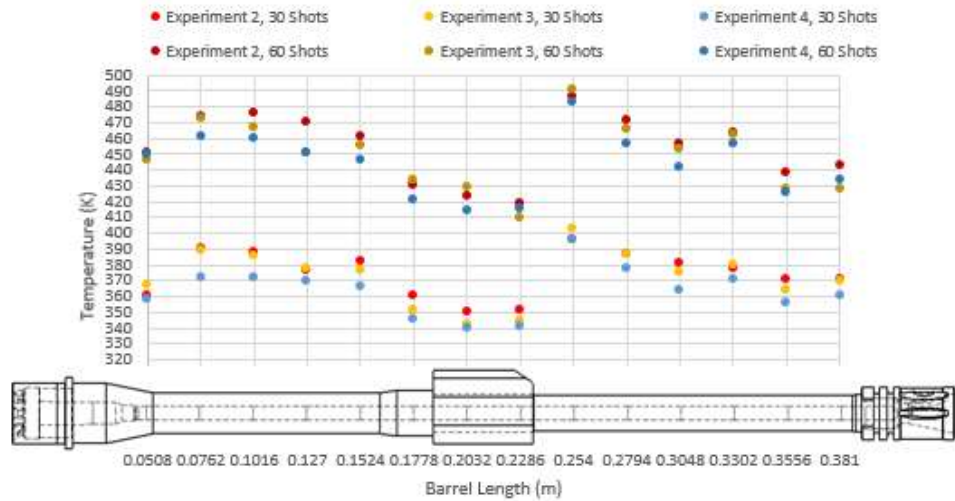


Figure 3.15: Axial Temperature Distribution at 30 and 60 Rounds Fired for Barrel Type 2.

The maximum barrel temperatures occurred at approximately 0.254 m. However, this location is not as likely to fail due to the lower pressures. The next location with high temperature occurs at approximately 0.1016 m, which is exposed to significantly higher pressure.

### 3.4 Repeatability

The maximum standard deviation for the fully automatic experiments (experiments 2 – 4) was 14.8 K at 0.3048 m from the breech. Figure 3.16 compares the temperature change for all four experiments at several locations along the gun tube. Figure 3.17 plots the standard deviation to the number of cartridges fired. Figure 3.17 shows no distinct trend for all measurement points.

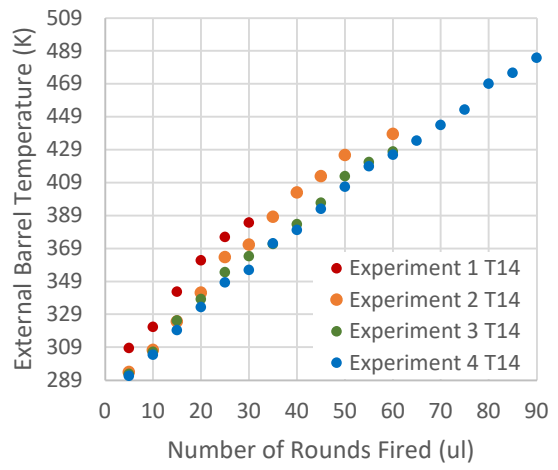
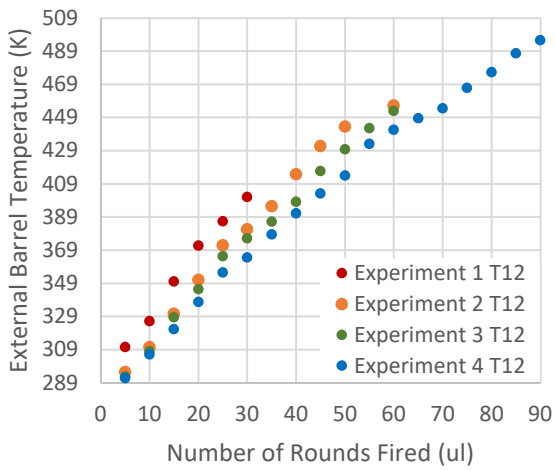
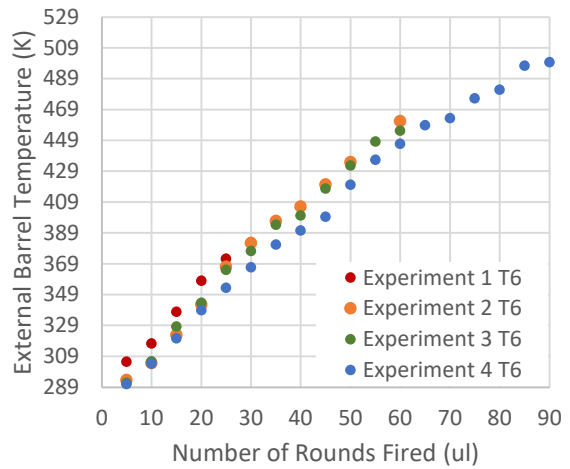
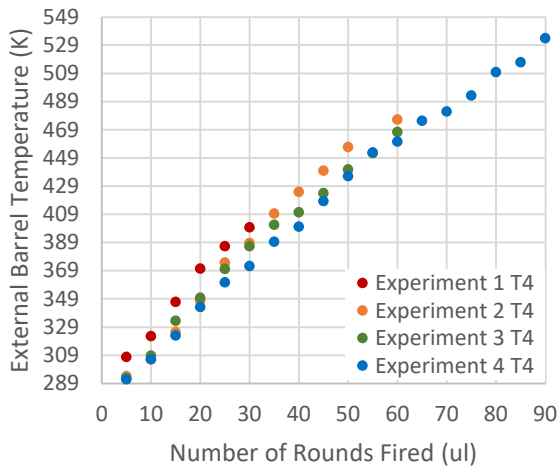


Figure 3.16: Sample results for temperature vs cartridges fired.

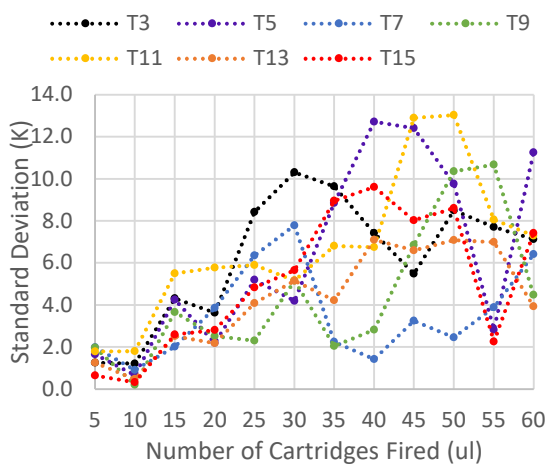
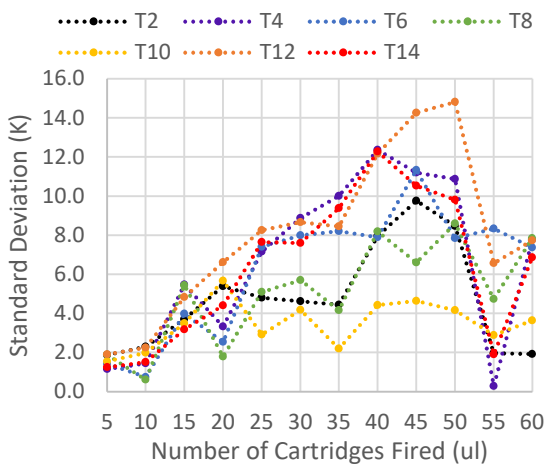


Figure 3.17: Experiment standard deviations.

## 4 SIMULATION RESULTS

This chapter presents the predicted transient temperature distribution and thermo-elastic stress results from the modeling and simulation method. The three topics discussed in this chapter are verification, validation, and predicting the effects of firing schedule parameters on gun tube temperatures.

### 4.1 Verification

Verification is the process of determining that a computational model accurately represents the underlying mathematical model and its solutions. Sections 4.1.1 and 4.1.2 investigate the stability and sensitivity of the modeling and simulation method. Sections 4.1.3 and 4.1.4 compare simulation results to analytical solutions for simplified cases.

#### 4.1.1 Mesh Independence and Simulation Stability

This section studies the effects of user defined discretization parameters on the ANSYS transient thermal simulation results. The parameters evaluated were element size, number of time steps per shot, and number of axial steps along the barrel.

A simulation is considered stable when the calculation errors remain constant or decay over further time steps. Conversely, a simulation is unstable when calculation errors in further time steps are magnified by calculation errors in previous time steps. Calculation errors consist of human error, round-off error, and truncation error. For the firing phenomena, round-off error is especially important due to time steps on the order of  $10^{-6}$  with high convection loads. The stability criteria depend on the dimensionality, governing partial differential equations, boundary conditions, time step, and element size. ANSYS automatically evaluates the solution stability and will issue the warning, shown in Figure 4.1, found in the solution information file.

```
*** NOTE ***                               CP =      26.344   TIME= 21:07:07
The preconditioned conjugate gradient solver failed to converge, and
therefore no solution was obtained. The equation solver is now being
automatically switched to the sparse solver (EQSLV,SPARSE) to allow
this analysis to continue.
```

Figure 4.1: ANSYS Failure to Converge Warning.

#### 4.1.1.1 Mesh Independence

In ANSYS, the user must, at a minimum, specify the element size to mesh the imported barrel geometry. As this parameter effects simulation stability, it is important to quantify the effect on simulation results. A simulation is considered mesh independent when the simulation converges to one solution regardless of further mesh refinement. A converged solution implies a stable simulation.

To evaluate the mesh independence of the model proposed, element sizes of 0.00254, 0.00127, and 0.000635 m were chosen. The firing schedule described in Table 4.1 is used for verification sections 4.1.1 and 4.1.2. Table 4.2 shows the percent change in maximum external temperature.

Table 4.1: Verification firing schedule.

Input Parameter	Value	Units
Barrel	AR-15	<i>ul</i>
Barrel type	2	<i>ul</i>
Initial temperature	296.6	<i>K</i>
External heat transfer coefficient	30.74	<i>W/m – K</i>
Fire rate	943	<i>rpm</i>
Number of cartridges fired per burst	30	<i>rounds/burst</i>
Total number of cartridges fired	30	<i>rounds</i>
Cooling time between bursts	5.0	<i>seconds</i>

Table 4.2: Percent Change in Maximum Temperature from an Element Size of 6.35E-4.

Element Size (m)	T2 (m)	T3 (m)	T4 (m)	T5 (m)	T6 (m)	T7 (m)	T8 (m)
.002540	0.1%	0.6%	0.2%	0.2%	0.4%	0.9%	0.5%
.001270	1.4%	1.3%	1.2%	1.1%	1.1%	1.1%	0.9%
Element Size (m)	T9 (m)	T10 (m)	T11 (m)	T12 (m)	T13 (m)	T14 (m)	T15 (m)
.002540	0.8%	1.2%	1.1%	1.0%	0.7%	0.8%	0.6%
.001270	0.7%	1.5%	1.5%	1.5%	1.3%	1.5%	1.4%

#### 4.1.1.2 Transient Discretization

Like mesh independency, a simulation is considered time-step independent when the simulation converges to one solution regardless of increased transient discretization. For this study, the transient discretization must carefully be chosen, as it showed to have the greatest impact on solution stability and convergence.

The transient discretization is quantified in number of time steps per shot. QuickLOAD only allows the user “low, medium, or high” refinement of the time steps for the time of combustion. QuickLOAD will automatically calculate the number of time steps. The QuickLOAD output is taken as the maximum number of time steps allowable for the time of combustion. To complete the firing time portion of the firing schedule, the user must define the number of steps for the exhaust period. The time between shots and the cooling time between bursts is also user specified.

To evaluate the time-step independence, the firing schedule from Table 4.1 was simulated with time steps from 30 to 200. The simulation results displayed in Figures 4.2 and 4.3 exhibit a decaying oscillatory response to the increase in time-steps.

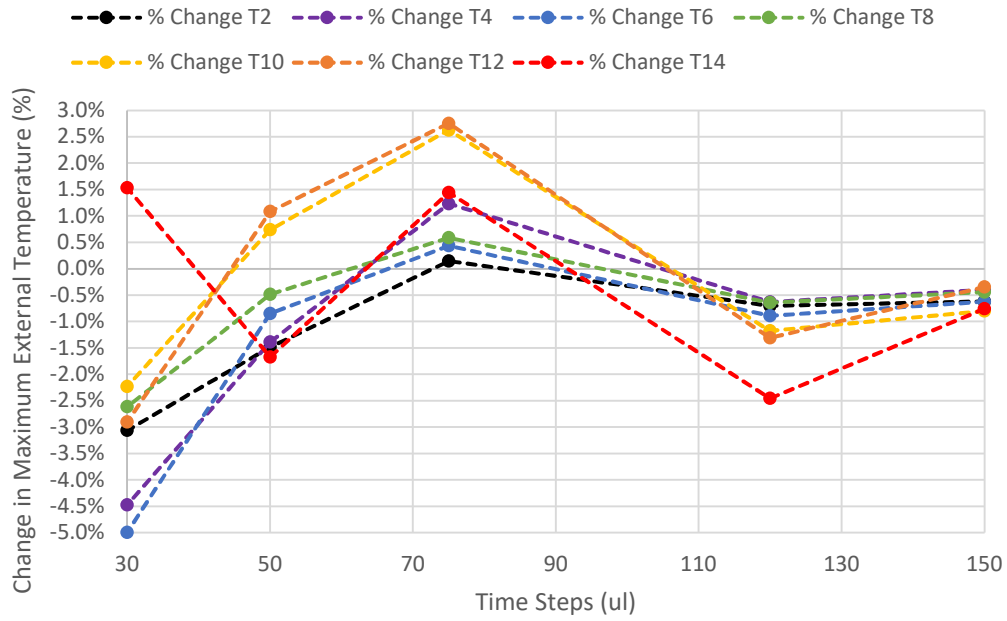


Figure 4.2: Percent change from 200 time-steps per shot.

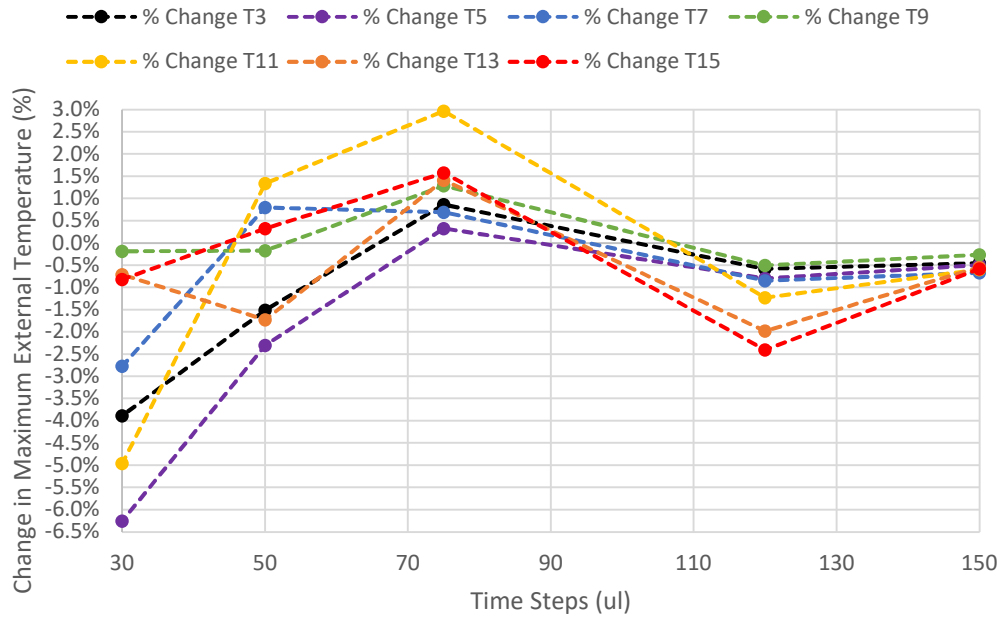


Figure 4.3: Percent change from 200 time-steps per shot.

### 4.1.1.3 Axial Discretization

As internal ballistics is a transient and spatially varying phenomena, the axial discretization is evaluated using the firing schedule from Table 4.1. For simplicity, axial steps were evenly distributed along the bore varying from 64 steps to 8 steps. Table 4.3 shows relatively coarse axial steps may be used for simulating the maximum local external temperatures of a gun tube.

Table 4.3: Percent Change in Maximum Temperature from 64 Axial Steps.

Axial Steps (ul)	T2 (m)	T3 (m)	T4 (m)	T5 (m)	T6 (m)	T7 (m)	T8 (m)
32	0.9%	-0.1%	-0.2%	-0.6%	-0.2%	-0.3%	0.1%
16	1.4%	-0.2%	-0.2%	-0.3%	0.0%	0.0%	-0.1%
8	0.9%	-0.7%	-0.9%	-1.0%	-0.8%	-0.8%	-0.4%
Axial Steps (ul)	T9 (m)	T10 (m)	T11 (m)	T12 (m)	T13 (m)	T14 (m)	T15 (m)
32	-0.1%	0.1%	0.1%	-0.1%	-0.1%	0.0%	0.4%
16	-0.3%	0.1%	0.1%	0.0%	-0.2%	0.3%	0.0%
8	-0.8%	-0.5%	-0.5%	-0.5%	-0.6%	-0.1%	-0.3%

## 4.1.2 Heat Transfer Coefficient Sensitivity

### 4.1.2.1 Internal Heat Transfer Coefficient

Table 4.4 displays the simulation results for the internal heat transfer coefficient sensitivity study. Simulation results show approximately a 10% change in maximum external barrel temperature for a 50% change in internal heat transfer coefficient. The relationship in Figure 4.4 is linear with an average slope of 17.4% with an intercept of -17.6%.

Table 4.4: Sensitivity of maximum external barrel temperature for various internal heat transfer coefficients.

	T2	T3	T4	T5	T6	T7	T8
Multiplier	0.0508 (m)	0.0762 (m)	0.1016 (m)	0.127 (m)	0.1524 (m)	0.1778 (m)	0.2032 (m)
50%	-6.9%	-7.8%	-10.4%	-10.2%	-9.8%	-7.1%	-6.8%
100%	0.0%	0.0%	0.0%	0.0%	0.0%	0.0%	0.0%
125%	6.0%	7.3%	4.4%	4.3%	4.2%	3.1%	2.8%
150%	9.5%	11.3%	8.3%	8.2%	7.9%	5.9%	5.4%

	T9	T10	T11	T12	T13	T14	T15
Multiplier	0.2286 (m)	0.2540 (m)	0.2794 (m)	0.3048 (m)	0.3302 (m)	0.3556 (m)	0.3810 (m)
50%	-6.4%	-10.9%	-10.4%	-10.8%	-10.5%	-10.0%	-10.2%
100%	0.0%	0.0%	0.0%	0.0%	0.0%	0.0%	0.0%
125%	3.0%	4.7%	4.5%	4.7%	4.5%	4.3%	4.3%
150%	5.6%	8.9%	8.6%	8.9%	8.5%	8.1%	8.1%

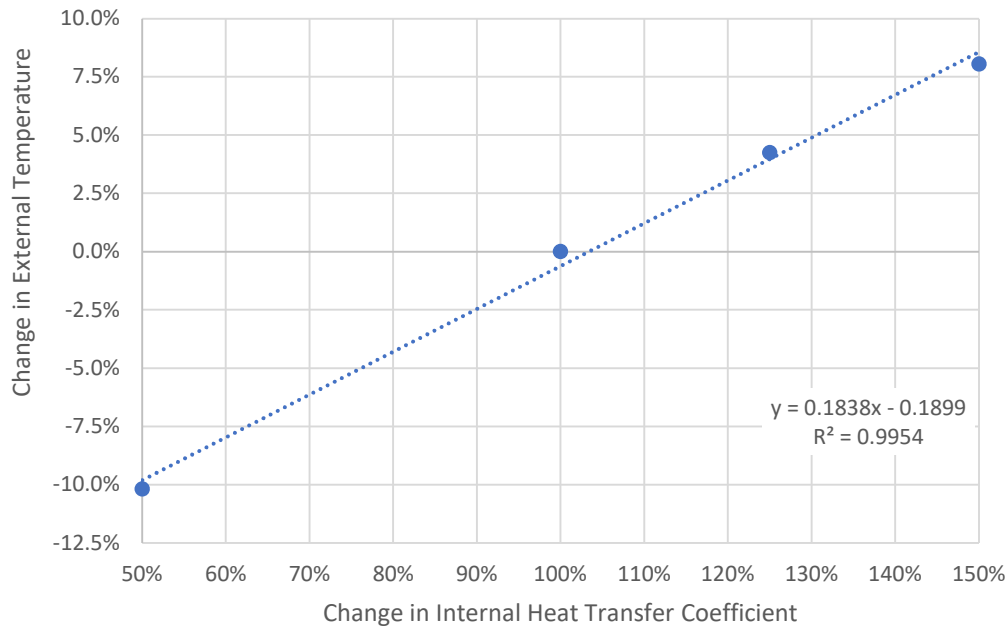


Figure 4.4: Relationship between relative change in temperature and relative change in internal heat transfer coefficient.

#### 4.1.2.2 External Heat Transfer Coefficient

The sensitivity of the simulated external barrel temperature to changes in external heat transfer coefficient was negligible over the firing time. The results for the relative change in external temperature before the cooling time between bursts is shown in Table 4.5. During the burst time, the maximum relative change in external temperature was 0.29% lower for the heat transfer coefficient of 153.7 W/m<sup>2</sup>-K.

The peak external temperature occurs shortly after the cooling time between bursts has begun. Table 4.6 shows the relative change in peak external temperature. The maximum relative change in peak external temperature is 2.34% lower for the heat transfer coefficient of 153.7 W/m<sup>2</sup>-K.

Table 4.5: Sensitivity of external barrel temperatures during firing for various external heat transfer coefficients.

Fire Rate	943 rpm	T2	T3	T4	T5	T6	T7	T8
External Heat Transfer Coefficient (W/m <sup>2</sup> – K)		0.0508 (m)	0.0762 (m)	0.1016 (m)	0.127 (m)	0.1524 (m)	0.1778 (m)	0.2032 (m)
15.37	50%	0.02%	0.03%	0.03%	0.03%	0.03%	0.02%	0.03%
30.74	100%	0%	0%	0%	0%	0%	0%	0%
76.85	250%	-0.07%	-0.09%	-0.09%	-0.09%	-0.09%	-0.06%	-0.09%
153.7	500%	-0.18%	-0.23%	-0.25%	-0.25%	-0.24%	-0.16%	-0.23%
Fire Rate	943 rpm	T9	T10	T11	T12	T13	T14	T15
External Heat Transfer Coefficient (W/m <sup>2</sup> – K)		0.2286 (m)	0.2540 (m)	0.2794 (m)	0.3048 (m)	0.3302 (m)	0.3556 (m)	0.3810 (m)
15.37	50%	0.03%	0.04%	0.03%	0.04%	0.04%	0.03%	0.03%
30.74	100%	0%	0%	0%	0%	0%	0%	0%
76.85	250%	-0.09%	-0.11%	-0.10%	-0.11%	-0.11%	-0.10%	-0.10%
153.7	500%	-0.23%	-0.29%	-0.27%	-0.29%	-0.28%	-0.27%	-0.27%

Table 4.6: Sensitivity of maximum external barrel temperatures for various external heat transfer coefficients.

Fire Rate	943 rpm	T2	T3	T4	T5	T6	T7	T8
External Heat Transfer Coefficient	(W/m <sup>2</sup> – K)	0.0508	0.0762	0.1016	0.127	0.1524	0.1778	0.2032
		(m)						
15.37	50%	0.19%	0.25%	0.27%	0.27%	0.25%	0.20%	0.22%
30.74	100%	0%	0%	0%	0%	0%	0%	0%
76.85	250%	-0.57%	-0.73%	-0.79%	-0.79%	-0.73%	-0.59%	-0.63%
153.7	500%	-1.48%	-1.88%	-2.06%	-2.04%	-1.89%	-1.53%	-1.63%
Fire Rate	943 rpm	T9	T10	T11	T12	T13	T14	T15
External Heat Transfer Coefficient	(W/m <sup>2</sup> – K)	0.2286	0.2540	0.2794	0.3048	0.3302	0.3556	0.3810
		(m)						
15.37	50%	0.25%	0.30%	0.30%	0.31%	0.30%	0.29%	0.29%
30.74	100%	0%	0%	0%	0%	0%	0%	0%
76.85	250%	-0.73%	-0.87%	-0.87%	-0.90%	-0.88%	-0.85%	-0.83%
153.7	500%	-1.88%	-2.26%	-2.26%	-2.34%	-2.27%	-2.19%	-2.15%

### 4.1.3 Transient Thermal Analysis Verification

To verify the Transient Thermal Analysis software in ANSYS, a simulation was performed to estimate the cooling time for the non-uniform body temperature to reach an average body temperature of 300 K. The simulation results are compared to an analytical solution for lumped transient cooling provided by Kreith et al. (2011, pg. 117-118). The firing schedule, shown in Table 4.7, is used for the validation of experiment 1.

Table 4.7: Firing Schedule for Transient Thermal Verification.

Input Parameter	Value	Units
Barrel	AR-15	<i>ul</i>
Barrel type	Type 1	<i>ul</i>
Initial temperature	296.6	<i>K</i>
Fire rate	290	<i>rpm</i>
Number of cartridges fired per burst	30	<i>rounds/burst</i>
Total number of cartridges fired	30	<i>rounds</i>
Cooling time between bursts	N/A	<i>seconds</i>

For the analytical solution, the first step is to calculate the Biot Number to determine that the lumped system method can be used. If the Biot Number is less than 0.1, the lumped system method can be used (Kreith et al., 2011, pg. 117)

$$Bi = \frac{h_{avg}L_{char}}{k_{BBL}}, \quad 4.1.1$$

$$L_{char} = \frac{V_{BBL}}{A_{surf,BBL}}, \quad 4.1.2$$

$$h_{avg} = \frac{A_{inner}}{A_{total}}h_{inner} + \frac{A_{outer}}{A_{total}}h_{outer}. \quad 4.1.3$$

Performing an energy balance on the lumped system barrel yields

$$h_{avg}A_{surf,BBL}(T_{air} - T) = m_{BBL}C_{pBBL} \frac{dT}{dt} \quad 4.1.4$$

(Kreith et al., 2011, pg. 117). As the temperature distribution in the barrel is non-uniform, the average body temperature is taken for the internal energy term. Kreith et al. (2011, pg. 118) provide the solution to the energy balance, in terms of  $T_{avg}(t)$  and  $t$ , by integration

$$\ln\left(\frac{T_{avg}(t) - T_{air}}{T_{initial} - T_{air}}\right) = -\frac{h_{avg}A_{surf,BBL}}{\rho_{BBL}Vol_{BBL}C_{pBBL}}t = -\Phi t, \quad 4.1.5$$

$$\frac{T_{avg}(t) - T_{air}}{T_{initial} - T_{air}} = e^{-\Phi t}. \quad 4.1.6$$

Table 4.8 displays the initial values for the inputs to equations 4.1.1 through 4.1.6. Time steps were taken every 30 seconds. A new average heat transfer coefficient needs to be calculated for each time step, because the convection coefficients change with the barrel temperature. Table 4.9 displays the results from equations 4.1.1 through 4.1.6.

Table 4.8: Analytical lumped cooling inputs.

Parameter	Value	Units
Surface Area, $A_{surf,BBL}$	0.00734	$m^2$
Volume, $Vol_{BBL}$	$1.99 \times 10^{-5}$	$m^3$
Density, $\rho_{BBL}$	7861.1	$kg/m^3$
Average Specific Heat, $C_{pBBL}$	470.0	$J/kg - K$
Average Thermal Conductivity, $k_{BBL}$	42.4	$W/m - K$
Ambient Temperature, $T_{air}$	296.6	$K$
Average Initial Temperature, $T_{initial}$	389.3	$K$
Inner Convection Coefficient, $h_{inner}$	30.7	$W/m^2 - K$

Table 4.9: Analytical lumped cooling outputs.

Output	Value	Units
Characteristic Length, $L_{char}$	0.00271	$m$
Biot Number, $Bi$	0.00152	$ul$
Time Constant, $\Phi$	0.00237	$1/sec$

Figure 4.5 displays the comparison between Experiment 1 and the verification method, and Table 4.10 provides the cooling times to 300 K.

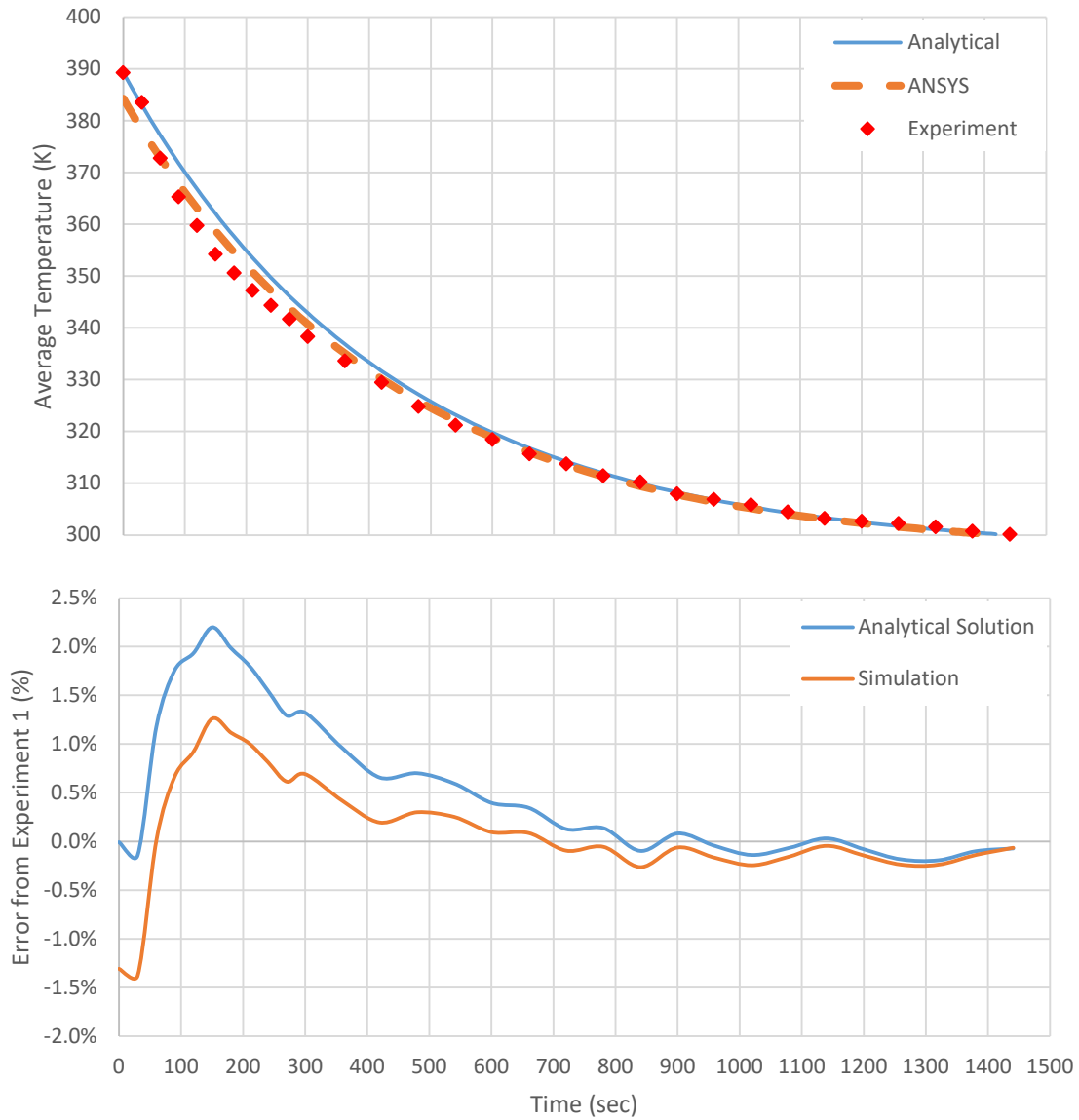


Figure 4.5: Verification of ANSYS Transient Thermal Analysis.

Table 4.10: Final Cooling Times to 300 K.

	Time (sec)	Initial Temperature (K)	Final Temperature (K)
Experiment 1	1441	389.32	300.22
Analytical Solution	1418	389.30	300.19
ANSYS	1410	384.24	300.15

#### 4.1.4 Static Structural Analysis Verification

To verify the results from ANSYS Static Structural, a simplified problem is compared to an analytical solution provided by Boresi and Schmidt (2003, pg. 410). The equations Boresi and Schmidt (2003, pg. 409-410) provide assume a steady state temperature distribution for thick-walled pressure vessels. Figure 4.6 shows the coupling of a Steady State Thermal analysis and a Static Structural analysis.



Figure 4.6: ANSYS Workbench setup for thermo-elastic stress verification.

Figures 4.7 and 4.8 show the cross-section taken 0.0762 m from the breech with the thermal and structural boundary conditions applied.

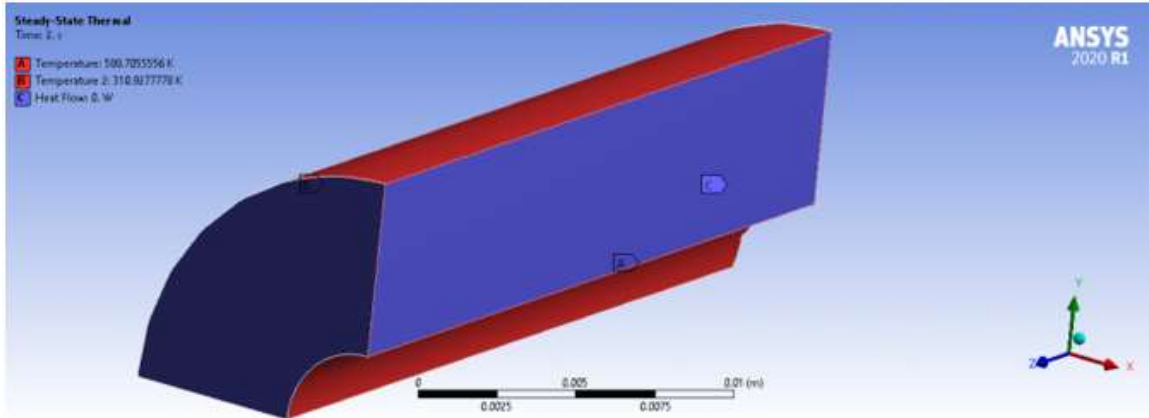


Figure 4.7: Boundary conditions for transient thermal portion of thermo-elastic stress verification.

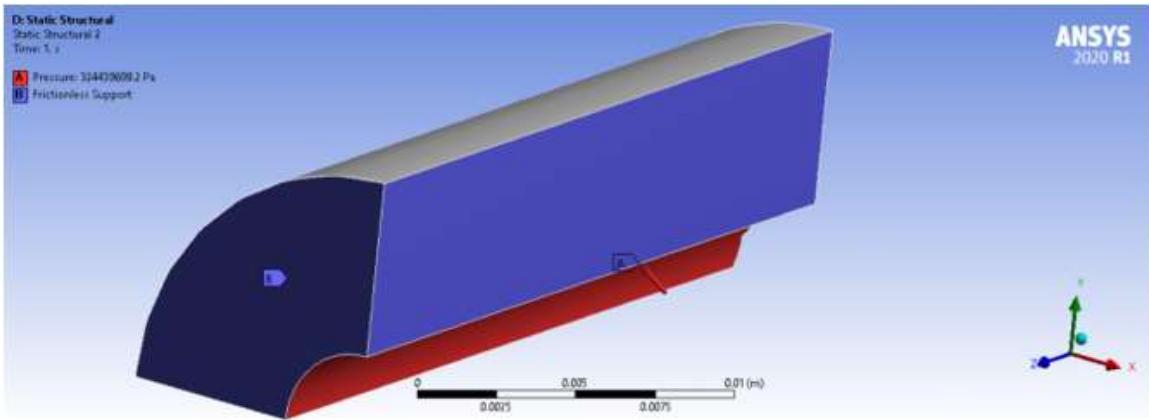


Figure 4.8: Mechanical boundary conditions for thermo-elastic stress verification.

Table 4.11 displays the inputs used for the analytical solution. ANSYS has the capability of evaluating the thermo-elastic stress equations using thermal varying parameters, such as the elastic modulus and Poisson's ratio. The maximum percent error in Figure 4.9 is in Von Mises stress with a percent error of 2.4%.

Table 4.11: Analytical thermo-elastic stress inputs.

Parameter	Value	Units
Inner Radius, $r_{inner}$	0.00277	$m$
Outer Radius, $r_{outer}$	0.0085	$m$
Internal Pressure, $P_{inner}$	$3.24 \cdot 10^8$	$Pa$
External Pressure, $P_{outer}$	0	$Pa$
Internal Temperature, $T_{inner}$	588.7	$K$
External Temperature, $T_{outer}$	310.9	$K$
Modulus of Elasticity, $E$	$2.05 \cdot 10^{11}$	$Pa$
Poisson's Ratio, $\zeta$	0.29	$ul$
Coefficient of Linear Thermal Expansion, $\mathcal{L}$	$12.28 \times 10^{-6}$	$1/K$

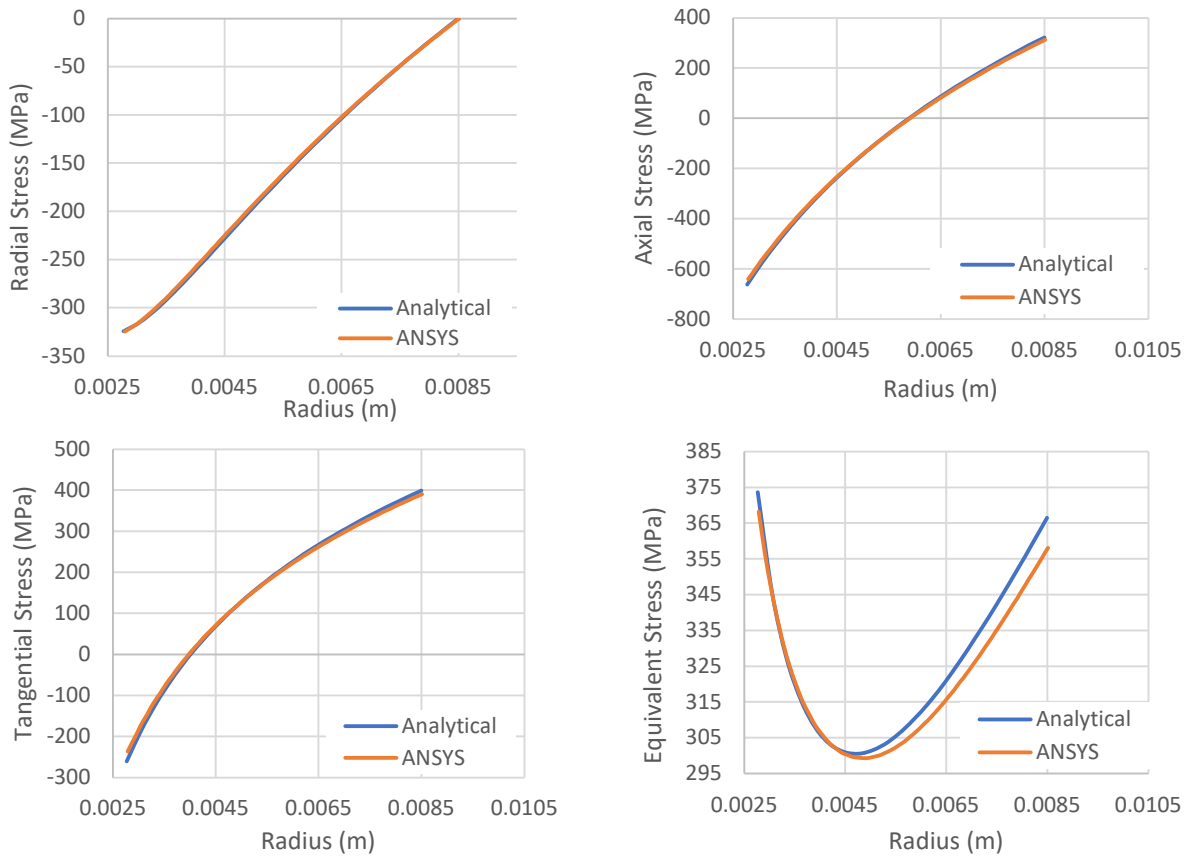


Figure 4.9: Verification of ANSYS Mechanical Output.

## 4.2 Validation

Validation is the process of determining the degree to which a model is an accurate representation of the real world from the perspective of the intended uses of the model. Validation of the model used to calculate the temperature distribution was done by two methods. The first method evaluates the transient cooling of the barrel to a specific temperature, which is the same method used to verify the ANSYS results. The second method is to evaluate the transient change in external barrel temperature at specified points along the barrel. Validation of the thermo-elastic stress in the gun tube was performed by comparing the number of rounds until rupture between the simulation results and experiment data from Windham (1996).

### 4.2.1 Validation of Temperature Distribution

Validation of the transient temperature distribution for the AR-15 medium – profile barrel was performed for each successful experiment. This section specifically covers the comparison between the fourth experiment and ANSYS. The firing schedule for ANSYS is shown in Table 4.12. The comparisons between the other experiments and their respective ANSYS simulations can be found in Appendix I.

Table 4.12: Experiment 4 simulation inputs.

Input Parameter	Value	Units
Initial temperature	289.3	<i>K</i>
External heat transfer coefficient	30.74	<i>W/m – K</i>
Fire rate	943	<i>rpm</i>
Number of cartridges fired per burst	30	<i>rounds/burst</i>
Total number of cartridges fired	90	<i>rounds</i>
Cooling time between bursts	8.5	<i>seconds</i>

Figures 4.10 through 4.12 show the comparison between the experiment data and simulation results for the fourth experiment. The maximum absolute percent error was found to be 12.3% and occurs at approximately 0.2032 meters. Not considering the gas block and port region, the maximum percent error is 10.2% occurring at 0.3048 meters.

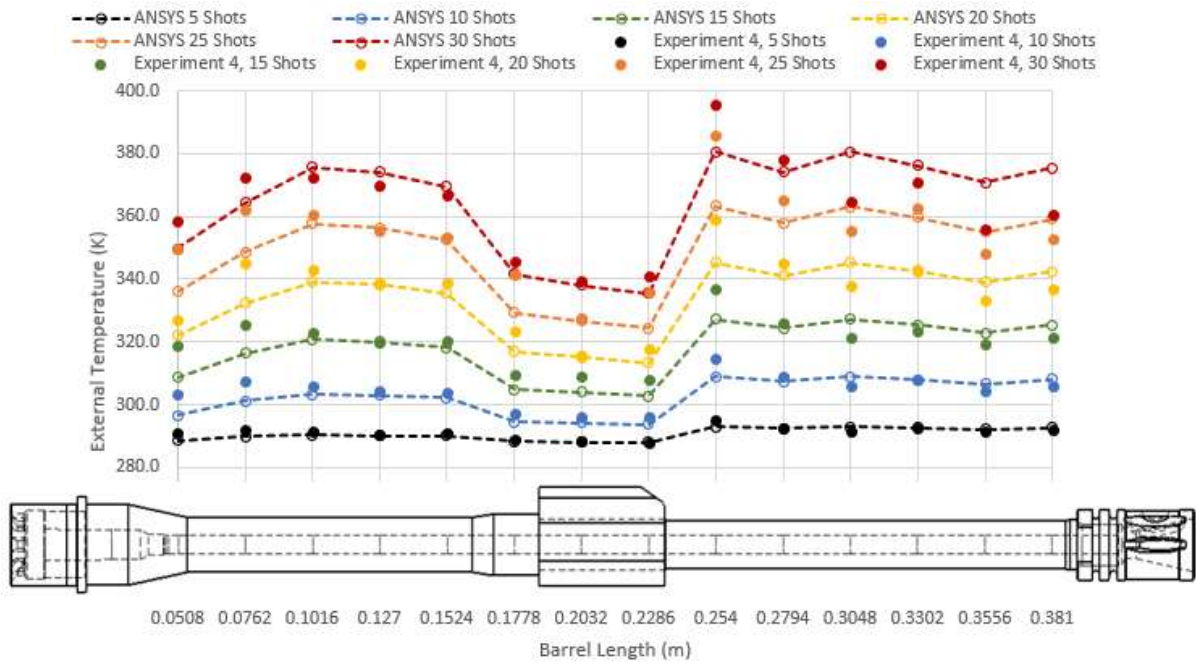


Figure 4.10: Temperature distribution after 30 rounds fired.

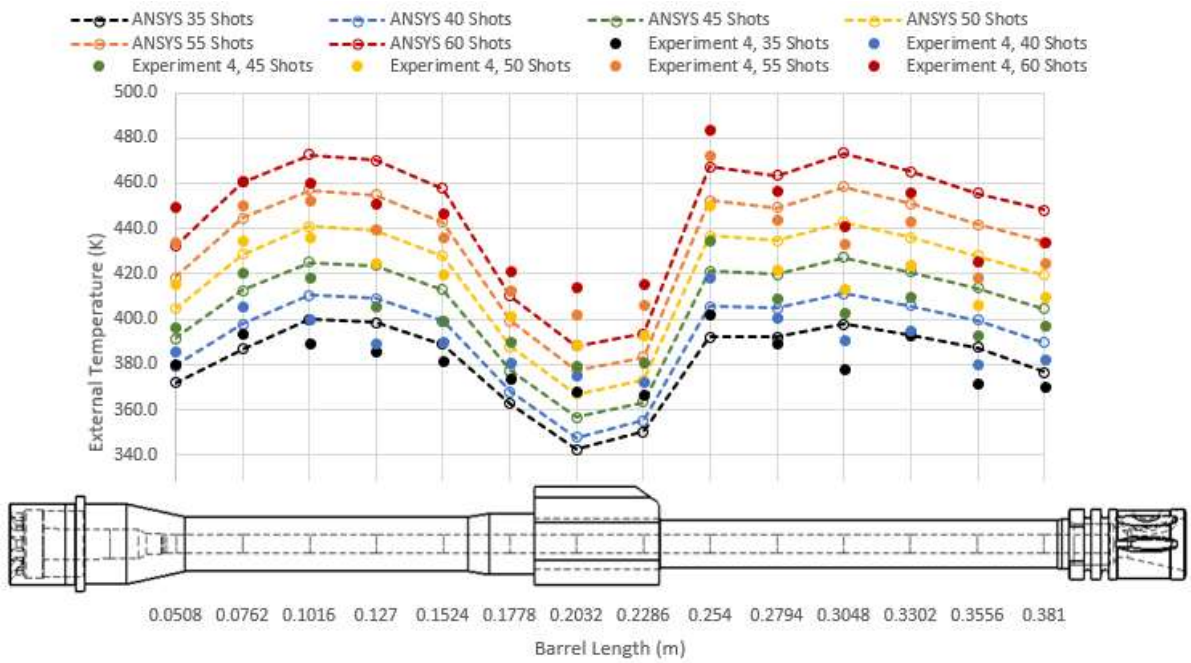


Figure 4.11: Temperature distribution after 60 rounds fired.

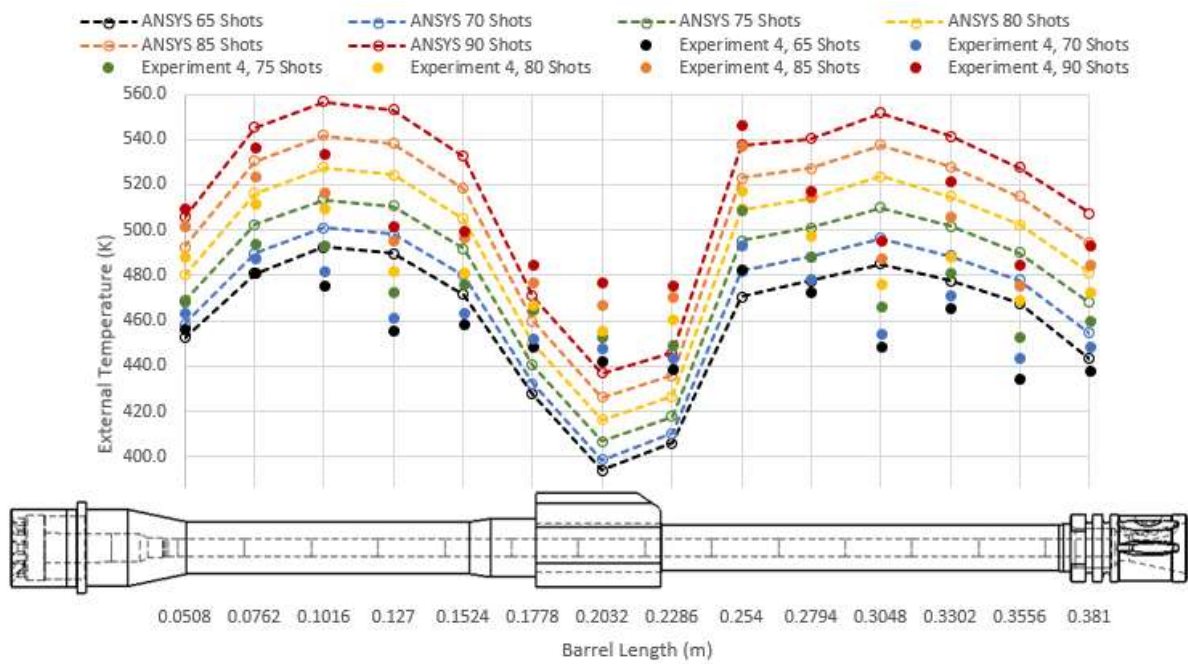


Figure 4.12: Temperature distribution after 90 rounds fired.

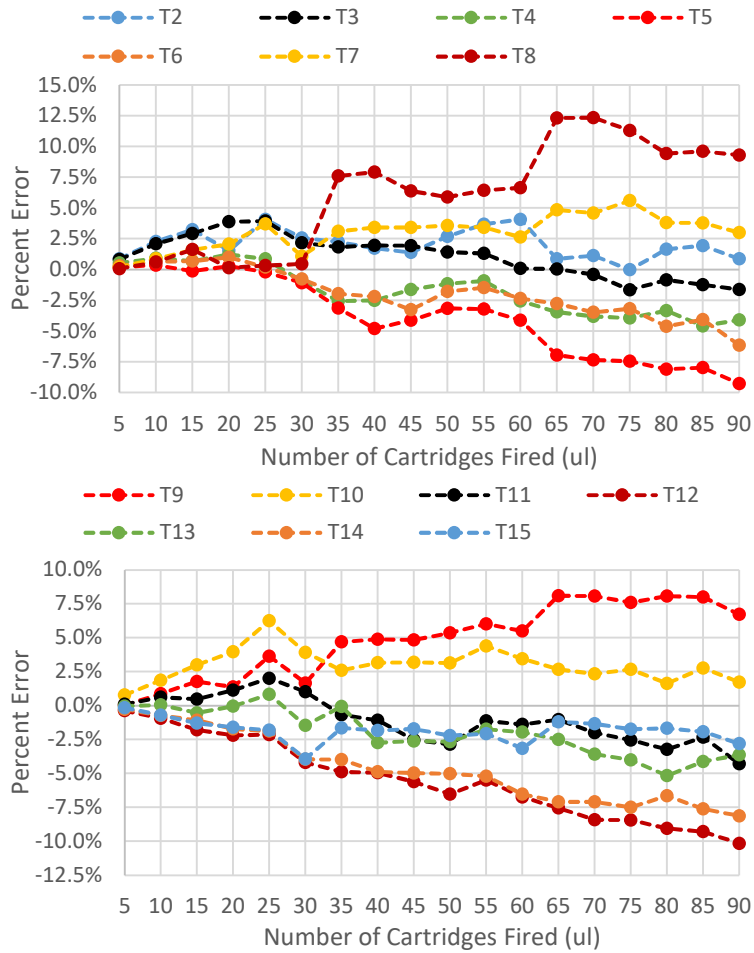


Figure 4.13: Percent error from experiment.

Figure 4.13 shows heat transfer from flow through barrel features such as gas ports should not be ignored. Gas ports allow burning propellant gas to exit the bore into a separate chamber to operate the weapon. Figure 4.13 shows the absolute percent error increases as the number of cartridges fired increases. The general trend of the barrel's external temperature distribution matches closely to the experiment. However, regardless of the accuracy and precision of any simulation, physical testing of the weapon system must always be performed to prove its adherence to the functional requirements.

#### 4.2.2 Validation of Thermo-elastic Stress

Data from *Fire to Destruction Test of 5.56 mm M4A1 Carbine and M16A2 Rifle Barrels* performed by Jeff Windham is used to validate the thermo-elastic stress. The destruction of the test weapon used in section 4.2.1 was considered too costly and dangerous to perform presently. For simplicity, the peak external temperatures were approximated from Windham’s data and are presented in Figure 4.14 and in Appendix F. The second experiment was approximated up to 360 rounds, while the first experiment was approximated to 540 rounds. Windham found both the M16 and the M4A1 Carbine barrels ruptured at temperatures between 1166 K and 1207 K. The M4 Carbine barrels saw significant damage and failure between 540 and 592 rounds, based on the firing schedules shown in Figures 1.6 and 1.7. At which point, the barrel failed by rupturing approximately 0.1016 m from the breech face. Table 4.13 shows the firing schedule used for the thermo-elastic stress validation.

Table 4.13: Firing schedule for M4A1 carbine barrel rupture simulation.

Parameter	Value	Units
Fire Rate	925	<i>rounds/minute</i>
Number of Shots	600	<i>rounds</i>
Shots per Reload	30	<i>rounds/magazine</i>
Shot Time	2.11	<i>milliseconds</i>
Reload Time	8.0	<i>seconds</i>
Cooling Time Between Bursts	0	<i>seconds</i>
Ambient Temperature	295.15	<i>K</i>
External Heat Transfer Coefficient	30.74	<i>W/m<sup>2</sup> – K</i>

In *Fire to Destruction Test of 5.56 mm M4A1 Carbine and M16A2 Rifle Barrels*, the reload time is approximated to be 10 seconds. There is also a 30 second cooling period induced on the second M4A1 Carbine barrel during tested, which may have affected the number of rounds until failure. Figure 4.14 also compares the ANSYS transient thermal results to the data collected by Windham in 1996 and 1994. Figure 4.15 shows the simulated transient bore temperature and external temperature for distances of 0.0508 m, 0.1016 m, and 0.1397 m from the breech.

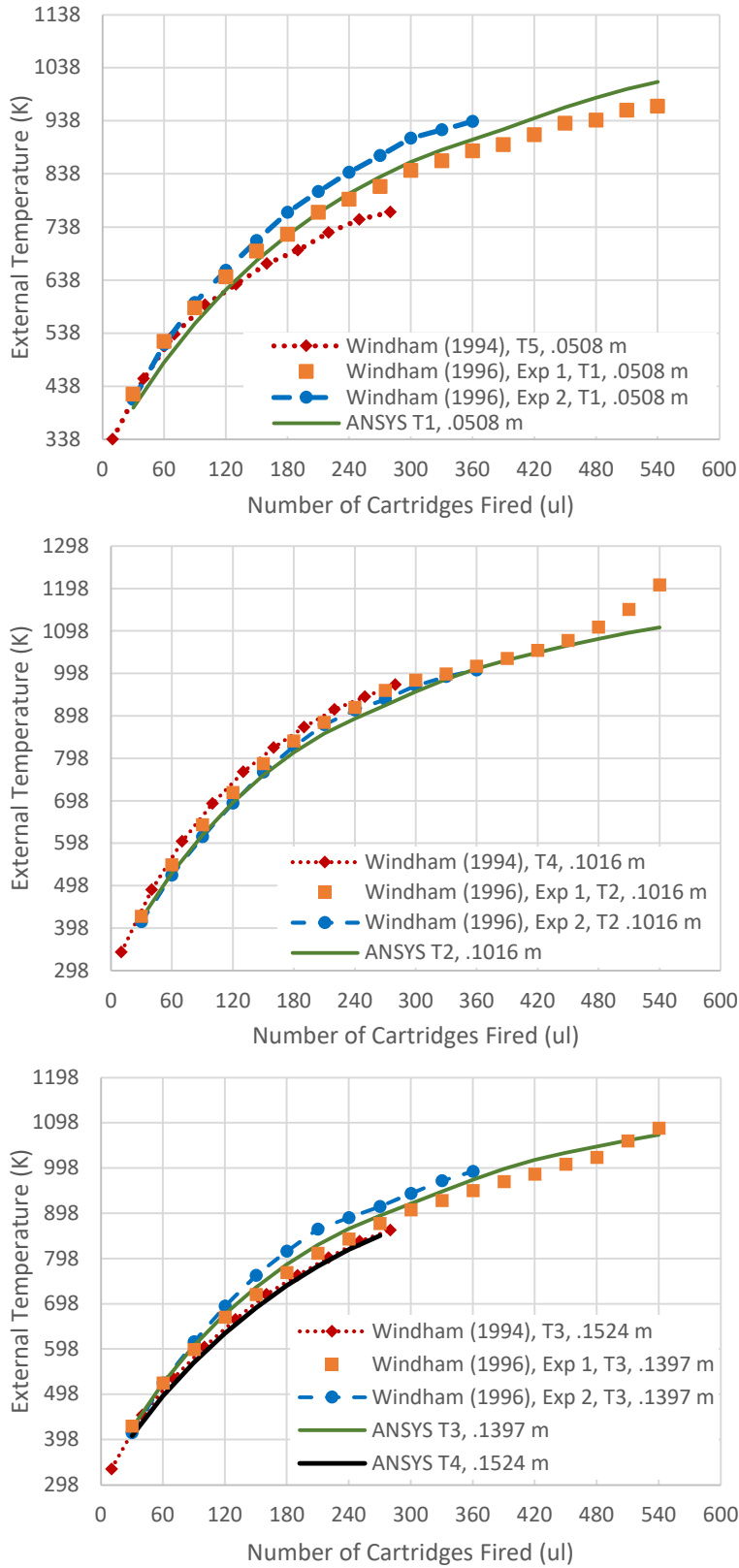


Figure 4.14: Comparison of ANSYS results to data collected by Windham (1994 and 1996).

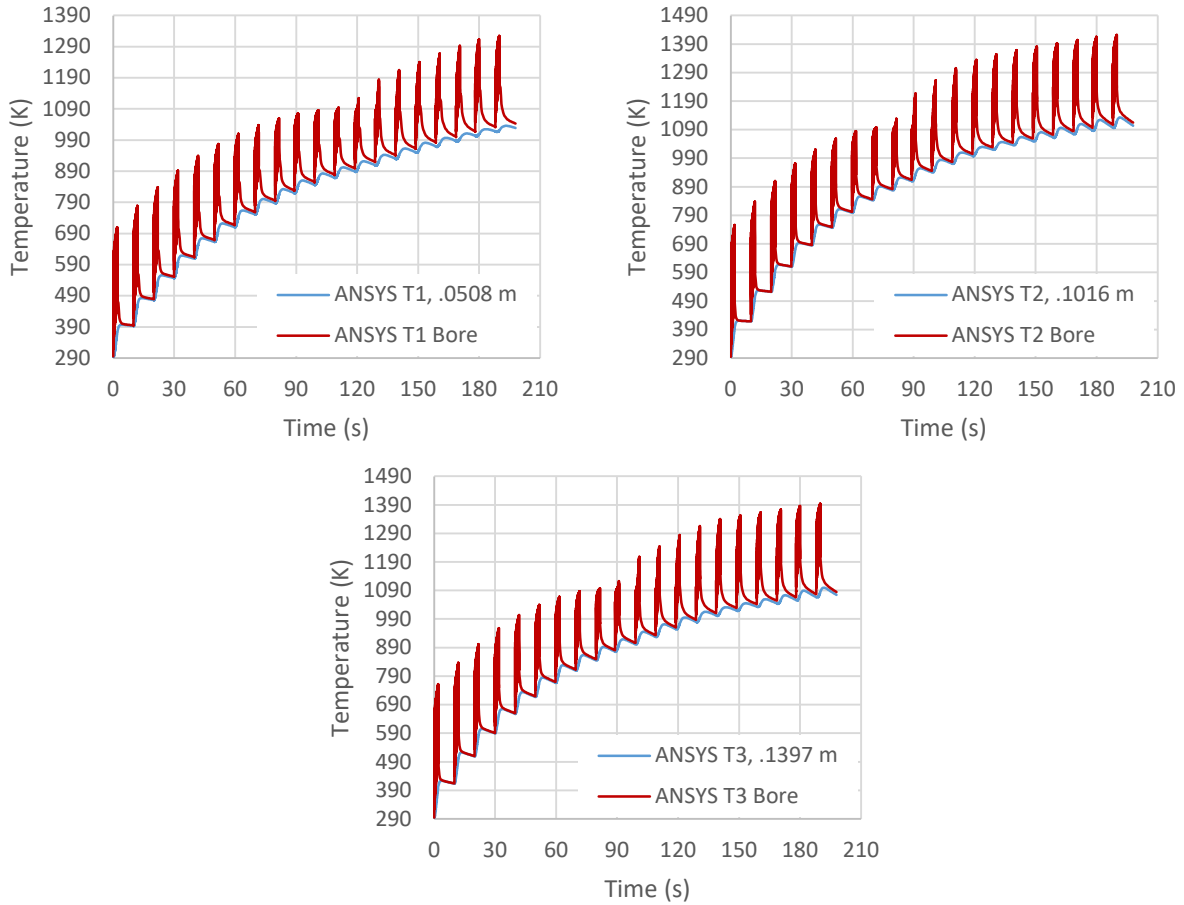


Figure 4.15: Bore and external temperatures for 600 round simulation.

The maximum local pressure curve, shown in Figure 2.8, is used to quickly check the safety factor of the gun tube at several times during the simulations. The maximum local pressure curve allows for an informative view of the maximum stresses along the gun tube, but the transient nature of ballistics is neglected. Figure 4.16 shows the first minimum local safety factor check at 270 rounds fired. The results show the gun tube is sufficiently safe at 270 rounds fired.

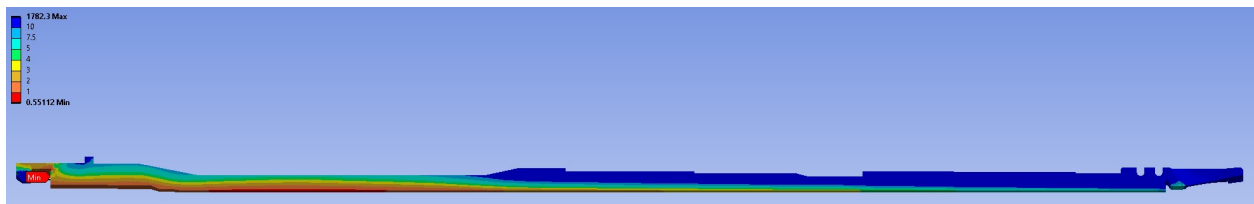


Figure 4.16: Safety factor for maximum local pressure at 270 rounds.

Figure 4.17 shows the minimum local safety factor check at 450 rounds fired, which shows the gun tube has a minimum safety factor between 1 and 2 at the outer diameter.

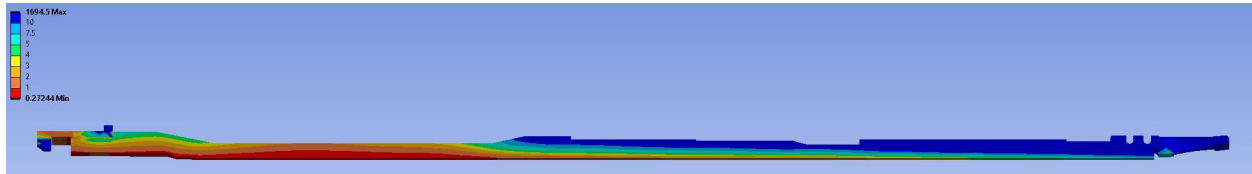


Figure 4.17: Safety factor for maximum local pressure at 450 rounds.

After 600 rounds had been simulated, the minimum local safety factor is checked for the last cartridge fired in each magazine between 450 and 600 rounds. This is done to reduce simulation time and converge on the exact cartridge that will rupture the gun tube. The cartridge at which the minimum local safety factor at the outer diameter becomes less than 1 is at 548 rounds. Figure 4.18 shows the minimum local safety factor at 548 rounds.

Next, a simulation is performed using the local transient pressure curves. Figure 4.19 shows the equivalent stress at 0.42 milliseconds after shot ignition. Figure 4.20 shows the point of failure at 0.0918 m from the breech. Figure 4.21 shows the temperature distribution at the time of failure, where the temperature at the location of failure is 1090.1 K. The resulting safety factor is 0.98 with respect to the ultimate strength shown in Figure 4.22. 0.42 milliseconds is slightly past the time of peak pressure in the gun tube, which is at 0.35 milliseconds. At the peak pressure of 317.3 MPa, the projectile has moved 0.078 m and has a velocity of 351.7 m/s. At 0.42 milliseconds, the projectile has a local gas pressure of approximately 278 MPa, has moved 0.109 m, and has a velocity of 486.7 m/s.

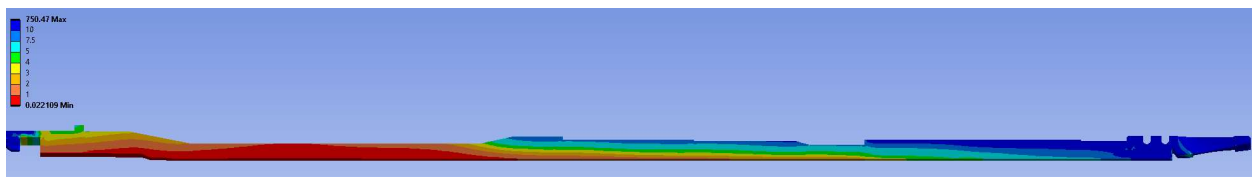


Figure 4.18: Safety factor for maximum local pressure at 548 rounds.

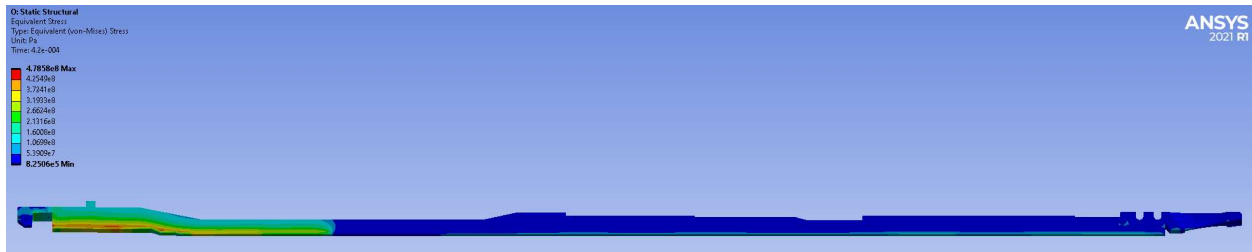


Figure 4.19: Equivalent stress at the time of barrel failure.

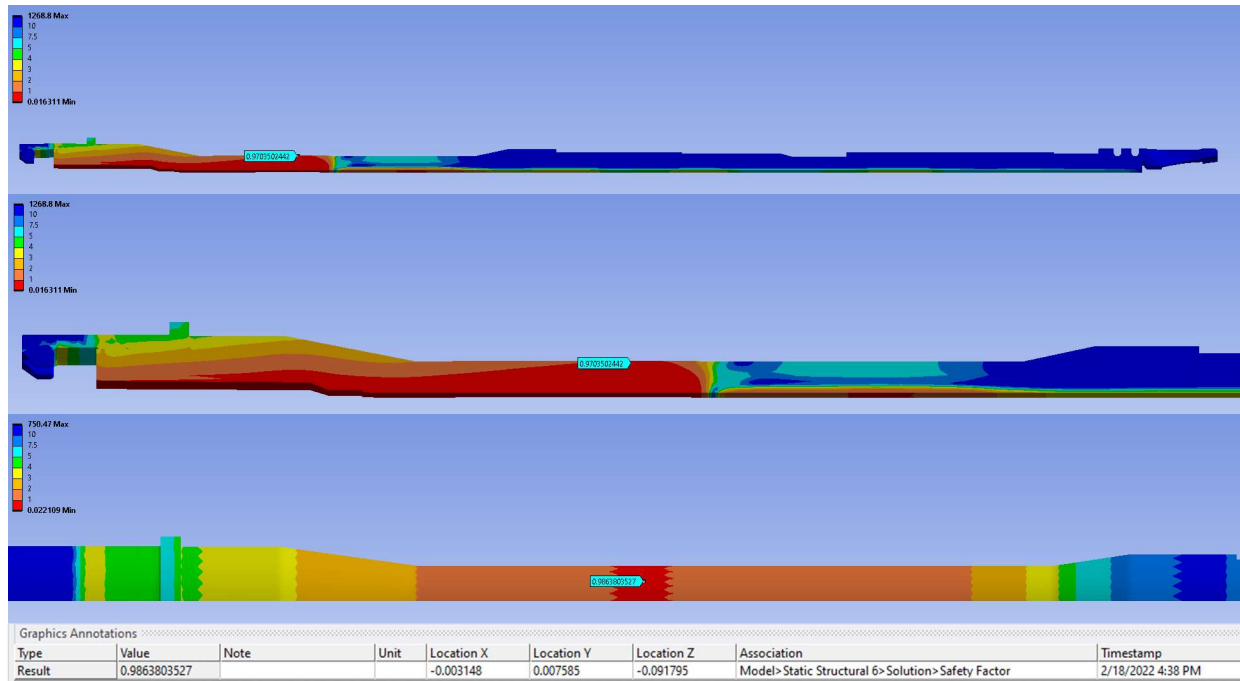


Figure 4.20: Initiation of barrel failure at 548 rounds.

Considering the maximum heat transfer coefficient along the gun tube, the peak of this curve occurs between .1016 and .1524 m, corresponding to times of .41 to .5 milliseconds. As the pressure is decaying, failure is more likely to occur closer to .1016 m. For the M4A1 carbine barrel, there is a strong correlation between the location of the maximum heat transfer coefficient and the failure position of the gun tube.



Figure 4.21: Temperature distribution at time of failure.

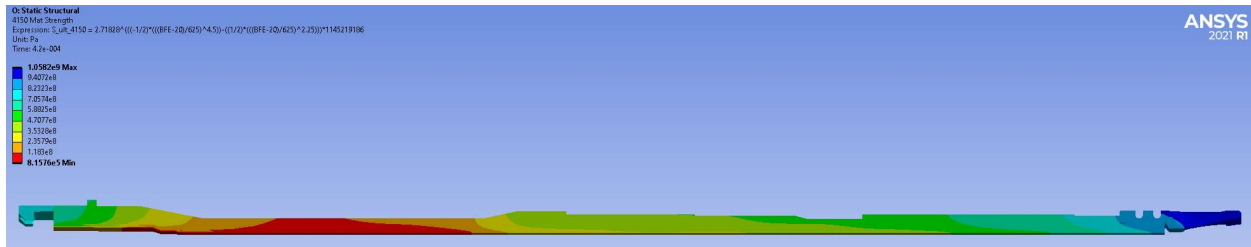


Figure 4.22: Material strength at time of failure.

Table 4.14 summarizes the ANSYS results and compares them to the data found by Windham in *Fire to Destruction Test of 5.56mm M4A1 Carbine and M16A2 Rifle Barrels*.

Table 4.14: ANSYS simulation results of the M4 Carbine barrel failure.

	ANSYS	Windham	Percent Error
Number of Rounds until Failure	548	592	7.4%
Point of Failure	.0918	.1016	9.7%
External temperature at point of failure	1090.1	1207	9.7%

### 4.3 Effects of Firing Schedule Parameters on Gun Tube Temperatures

#### 4.3.1 Cyclic Rate of Fire

Section 4.3.1 will evaluate the effects of variation in cyclic performance on the temperature distribution of the barrel. Variations in cyclic performance can be due to cartridge energy,

manufacturing (such as gas port size), or environmental differences that effect the response of the mass – spring – damper system. The acceptable range for the cyclic fire rate for the M4 Carbine is between 700 and 950 rpm. If the cyclic rate of fire is outside of this range, the weapon system is considered defective. To evaluate the effects of cyclic rate of fire, three simulations were performed using the firing schedules in Table 4.15.

Table 4.15: Inputs for the effects of cyclic rate of fire simulations.

Parameter	Value	Units
Barrel Type	M4 Carbine	
Fire Rate	950	<i>rounds/minute</i>
	825	
	700	
Number of Shots	270	<i>rounds</i>
Shots per Burst	30	<i>rounds/magazine</i>
Shot Time	2.11	<i>milliseconds</i>
Time Between Bursts	3.05	<i>seconds</i>
Ambient Temperature	296.6	<i>K</i>
External Heat Transfer Coefficient	30.74	<i>W/m<sup>2</sup> – K</i>

Figure 4.23 shows the rate of heat transfer to the barrel increases as the cyclic rate of fire increases. At a given timing during a burst, a higher cyclic rate of fire will produce higher barrel temperatures. However, there is no significant change in peak external barrel temperature after the burst, as the same number of cartridges are fired. Therefore, when considering variations in cyclic rate of fire during barrel design, the average cyclic rate of fire for the weapon should provide sufficient accuracy. Table 4.16 displays the barrel temperatures and percent change at the test points used by Windham (1996).

Table 4.16: External barrel temperature at the end of the firing schedule.

Cyclic Fire Rate (rpm)	External Temperature (K)			
	T1 .0508 (m)	T2 .1016 (m)	T3 .1397 (m)	T4 .2794 (m)
700	948	1032	1014	832
825	944	1032	1014	833
950	948	1031	1014	833

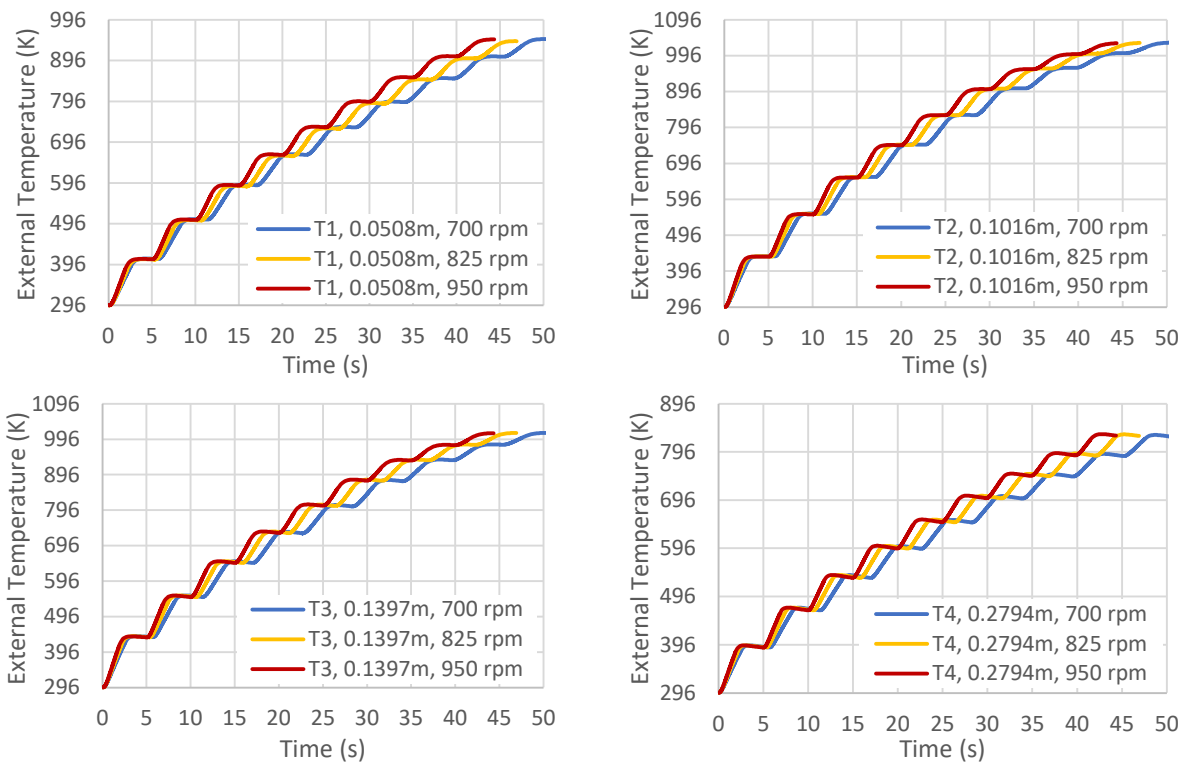


Figure 4.23: Temperature vs. time at various cyclic rates of fire.

### 4.3.2 Cooling Time Between Bursts

To provide insight in the effect of varying the cooling time between bursts, three simulations were performed using the firing schedules in Table 4.17.

Table 4.17: Inputs for the effects of cooling time between bursts simulations.

Parameter	Value	Units
Fire Rate	825	<i>rounds/minute</i>
Number of Shots	270	<i>rounds</i>
Shots per Burst	30	<i>rounds/magazine</i>
Shot Time	2.11	<i>milliseconds</i>
Time Between Bursts	3.05	<i>seconds</i>
	6	
Ambient Temperature	296.6	<i>K</i>
	10	
External Heat Transfer Coefficient	30.74	<i>W/m<sup>2</sup> – K</i>

The time between bursts was chosen to reflect the reload times for competitive shooting, well trained, and average shooters. However, these times are arbitrary.

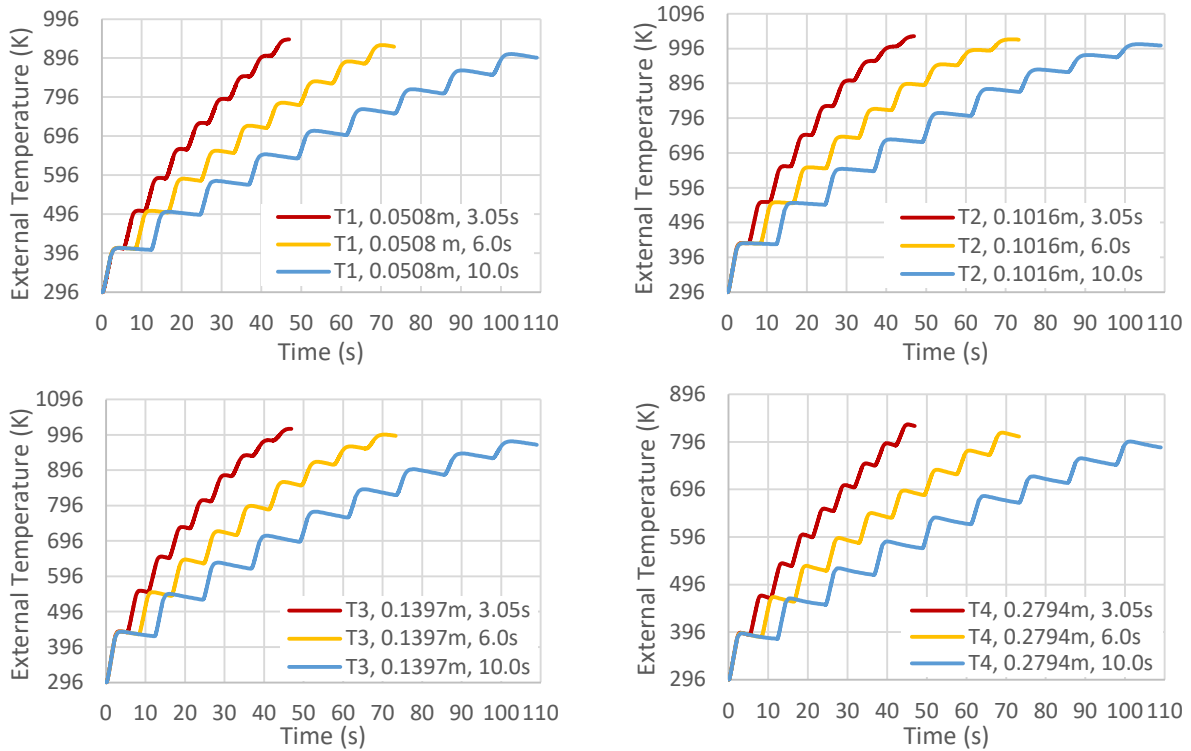


Figure 4.24: External temperature vs. time for various cooling time between bursts.

The simulation results shown in Figure 4.24 suggest a greater cooling time between bursts will produce lower barrel temperatures. Therefore, continuous fire will produce the highest barrel temperatures. These results support what is found in common functional requirements. As previously stated, functional requirements often specify the minimum number of cartridges that must be fired continuously. During the design process, it is desirable to specify firing schedules to provide both sufficient effect on target and maximum cooling time between bursts.

Figure 4.25 shows the relative change in external temperature for 6 and 10 seconds. The maximum change in external temperature at the end of the firing schedule was calculated to be 4.4% lower between a reload time of 3 seconds and 10 seconds. Tabular data for Figure 4.25 can be found in Appendix J.

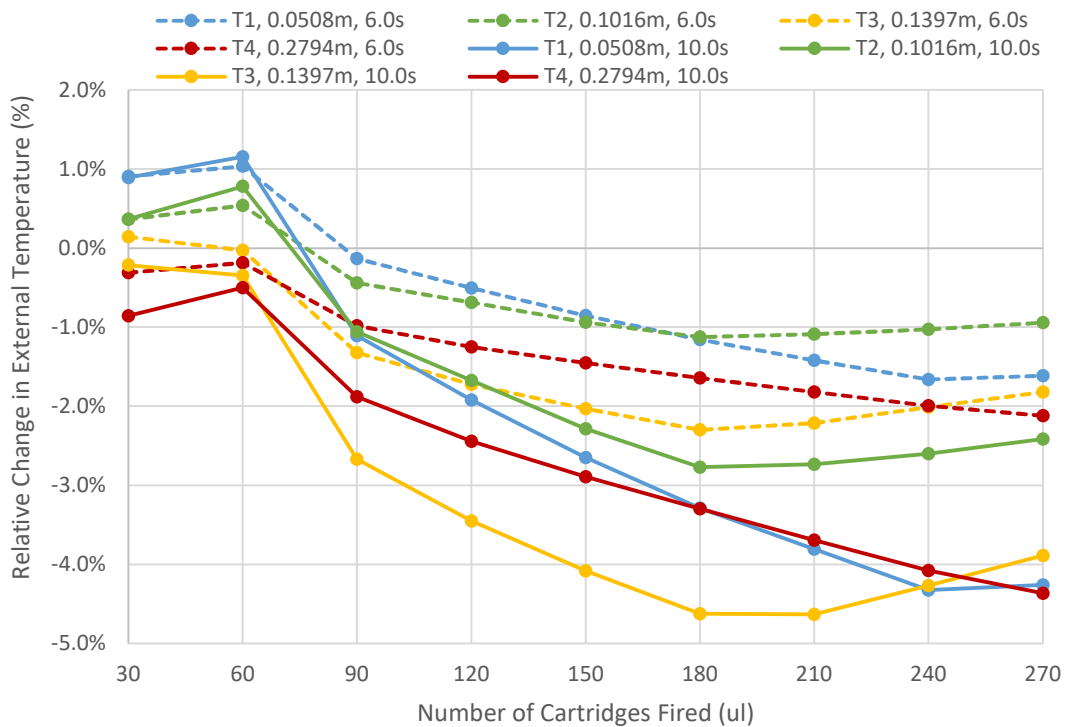


Figure 4.25: Relative change in external temperature for different times between bursts.

## 5 CONCLUSION

The objectives of this work are to predict the transient temperature distribution and thermo-elastic stress in gun tubes. Key steps in the process include:

1. Barrel geometries are created using SolidWorks and imported into ANSYS.
2. Ballistic data is calculated using QuickLOAD and exported to Excel.
3. The ballistic cycle is discretized axially and transiently.
4. Local internal and external heat transfer coefficients are calculated based on the discretized ballistic cycle.
5. The firing schedules and initial conditions are specified.
6. The barrel geometries are discretized and meshed in ANSYS.
7. Transient Thermal analysis is attached to the geometry module. The firing schedule, boundary conditions, and initial conditions from Excel are applied to the geometry.
8. Static Structural analysis is attached to the Transient Thermal analysis to calculate pressure and thermal stresses and strains.
9. Four experiments were performed to gather transient temperature data from an AR-15 barrel for validation of the model.
10. Simulations are performed to verify the model and understand the sensitivity of the model.
11. Simulations are performed to validate the model.
12. Simulations are performed to predict the effect of firing schedule parameters on gun tube temperatures.

The modeling and simulation process provides satisfactory results for predicting the transient temperature distribution and thermo-elastic stress in AR-15 and M4 Carbine barrels. Significant findings include:

- For the AR-15 barrel, the maximum error in temperature distribution was 12.3%.
- For the thermo-elastic stress simulation of an M4 Carbine barrel, the maximum percent error is less than 10% in the prediction of the location and temperature of failure.

- The number of cartridges fired before failure was 548 rounds, which is 7.4% error from that found by Windham.

Two significant conclusions from the study are:

- The rate of heat transfer increases as the cyclic rate of fire increases.
- For a given number of rounds fired in a burst, a greater cooling time between bursts has more effect on peak external barrel temperatures than variations in cyclic rate of fire.

## 6 RECOMMENDATIONS

To further refine the model, studies should be performed on gun tubes of different weapon classifications, cartridges, and propellants.

It is not recommended to use an FLIR Thermal Camera for experiments that require significant movement of the weapon due to the extensive amount of time and potential for user error. The FLIR software is unable to track user placed measurement nodes to the physical barrel, therefore requiring the weapon to remain stationary during the experiment. The firearm is rigidly held in a mount while shooting, however issues arise when the weapon is reloaded. When the weapon moves, the user must manually reposition the measurement nodes to the correct physical marker for each frame. To get a more accurate position for the temperature measurements from the FLIR Thermal Studios software, a grid should be applied to the barrel. The grid should convey the centerline of the barrel and graduations at desired increments in the axial and radial directions. Alternatively, properly rated thermocouples or a software that combines target tracking and thermal imaging would allow more weapon movement during testing.

## LIST OF REFERENCES

1. Windham, Jeff. "External Barrel and Handguard Temperature of the 5.56mm M4 Carbine." Engineering Support Directorate: Small Arms Branch, Rock Island, Illinois, 1994.
2. Windham, Jeff. "Fire to Destruction Test of 5.56mm M4A1 Carbine and M16A2 Rifle Barrels." Engineering Support Directorate: Small Arms Branch, Rock Island, Illinois, 1996.
3. Hunt, Col. F. R. W., et al. "Internal Ballistics." Philosophical Library, 1951.
4. Carlucci, Donald E., and Sidney S. Jacobson. "Ballistics: Theory and Design of Guns and Ammunition." 2nd ed., Taylor & Francis Group, 2014.
5. U.S. Army Materiel Command Alexandria Va. "ENGINEERING DESIGN HANDBOOK: GUNS SERIES, GUN TUBES." Fort Belvoir, VA: Defense Technical Information Center, February 1, 1964. <https://doi.org/10.21236/AD0830297>.
6. U.S. Army Materiel Command Alexandria Va. "ENGINEERING DESIGN HANDBOOK: BALLISTICS SERIES, INTERIOR BALLISTICS OF GUNS." Fort Belvoir, VA: Defense Technical Information Center, 1965.
7. U.S. Army Materiel Command Alexandria Va. "ENGINEERING DESIGN HANDBOOK: AMMUNITION SERIES, SECTION 4, DESIGN FOR PROJECTION." Fort Belvoir, VA: Defense Technical Information Center, 1964.
8. Boresi, Arthur P., and Richard J. Schmidt. "Advanced Mechanics of Materials." 6th ed., John Wiley & Sons, 2003.
9. Siebers, D, R Schwind, and R Moffat. "Experimental Mixed-Convection Heat Transfer from a Large, Vertical Surface in a Horizontal Flow." July 1, 1983. <https://doi.org/10.2172/5873492>.
10. Ludovisi, Daniele, and Ivo A. Garza. "Natural Convection Heat Transfer in Horizontal Cylindrical Cavities: A Computational Fluid Dynamics (CFD) Investigation." In *Volume 2: Reliability, Availability and Maintainability (RAM); Plant Systems, Structures, Components and Materials Issues; Simple and Combined Cycles; Advanced Energy Systems and Renewables (Wind, Solar and Geothermal); Energy Water Nexus; Thermal Hydraulics and CFD; Nuclear Plant Design, Licensing and Construction; Performance Testing and Performance Test Codes*, V002T11A001. Boston, Massachusetts, USA: American Society of Mechanical Engineers, 2013. <https://doi.org/10.1115/POWER2013-98014>.
11. Seif, Mina, Joseph Main, Jonathan Weigand, Fahim Sadek, et al. "Temperature-Dependent Material Modeling for Structural Steels: Formulation and Application." National Institute of Standards and Technology, April 2016. <https://doi.org/10.6028/NIST.TN.1907>.

12. Wright, P. (1990). "MILITARY HANDBOOK: METALLIC MATERIALS AND ELEMENTS FOR AEROSPACE VEHICLE STRUCTURES." Vol. 1. Washington, D.C.: U.S. Government Printing Office.
13. Kreith, F., Bohn, M., and Manglik, R. "Principles of Heat Transfer." 7th ed. Stamford, CT, Cengage Learning, 2011.
14. Mills, Anthony F. "Basic Heat and Mass Transfer." Chicago: Richard D. Irwin, INC., 1995.
15. Shelton, S., Bergles, A., and Saha, P. "Study of Heat Transfer and Erosion in Gun Barrels." Air Force Armament Laboratory, United States Air Force, Eglin Air Force Base, Florida, March, 1973.
16. "M240B Medium Machine Gun B3M0501XQ Student Handout." Camp Barrett, VA, United States Marine Corps Training Command.
17. Johnston, Ian A. "Understanding and Predicting Gun Barrel Erosion." Weapons Systems Division, DSTO, Edinburgh, South Australia, Australia, 2005.
18. <https://www.flir.com/discover/rd-science/infrared-camera-accuracy-and-uncertainty-in-plain-language/>
19. <https://www.flir.com/products/e8-xt/>
20. Corner, John. "Theory of the Interior Ballistics of Guns." New York: John Wiley & Sons, 1950.
21. Guo-Tong Feng, Ke-Dong Zhou, et. al. "The Study of Gun Barrel's Two-Dimensional Nonlinear Thermal Conduction." International Journal of Thermophysics, Springer Science and Business Media, LLC.
22. Gadalla, M., Jasim, M., & Ahmad, O. "Heat Transfer Characteristics of Various Gun Barrels Under Different Operating Conditions." Proceedings of the ASME 2019 International Mechanical Engineering Congress and Exposition. Volume 8: Heat Transfer and Thermal Engineering. Salt Lake City, Utah, USA. November 11–14, 2019. V008T09A081. ASME. <https://doi.org/10.1115/IMECE2019-12083>.
23. Russell, L. H. "Simplified Analysis of the Bore Surface Heat Transfer Reduction in Gun Barrels as Achieved by Using Wear-Reducing Additives." Fort Belvoir, VA: Defense Technical Information Center, October 1, 1975. <https://doi.org/10.21236/ADA020639>.
24. Nastelin, H. "Determination of the Emissivity of Materials." Washington D.C., National Aeronautics & Space Administration, December 31, 1962.
25. Evci, Celal. "ANALYSIS OF THE EFFECT OF PROPELLANT TEMPERATURE ON INTERIOR BALLISTICS PROBLEM." *Journal of Thermal Engineering*, June 13, 2018, 2127–36. <https://doi.org/10.18186/journal-of-thermal-engineering.433738>.

26. Cheng, Xu, Yonghai Wu, and Xiaorong Guan. "The Transient Stress and Life Analysis of a Gun Tube." Anaheim, California, Proceedings of the ASME 2014 Pressure Vessels & Piping Conference, July 20-24, 2014.
27. Elbe, Ronald E. "External Barrel Temperature of the M16A1 Rifle." Fort Belvoir, VA: Defense Technical Information Center, July 1, 1975. <https://doi.org/10.21236/ADA019649>.
28. Conroy, P. J. "GUN TUBE HEATING." Aberdeen Proving Ground, Maryland, USA Ballistic Research Laboratory, December, 1991.
29. Chaturvedi, Devendra K. "Modeling and Simulation of Systems Using MATLAB® and Simulink®." Boca Raton, Florida: Taylor & Francis Group, 2010.
30. Incropera, F., Dewitt, D., Bergman, T., and Lavine, A. "Fundamentals of Heat and Mass Transfer." 6th ed., John Wiley & Sons, 2006.

## APPENDIX A. DETERMINATION OF THE POWDER, AND SIMULATION OF THE PRESSURE AND VELOCITY CURVES OF THE PROJECTILE

QuickLOAD is an internal ballistics program that produces pressure and velocity curves for many cartridges. Figure A.1 displays the QuickLOAD user interface. The powder chosen is AR-COMP, which is a generic 5.56 x 45 mm powder, produced by Alliant Inc.

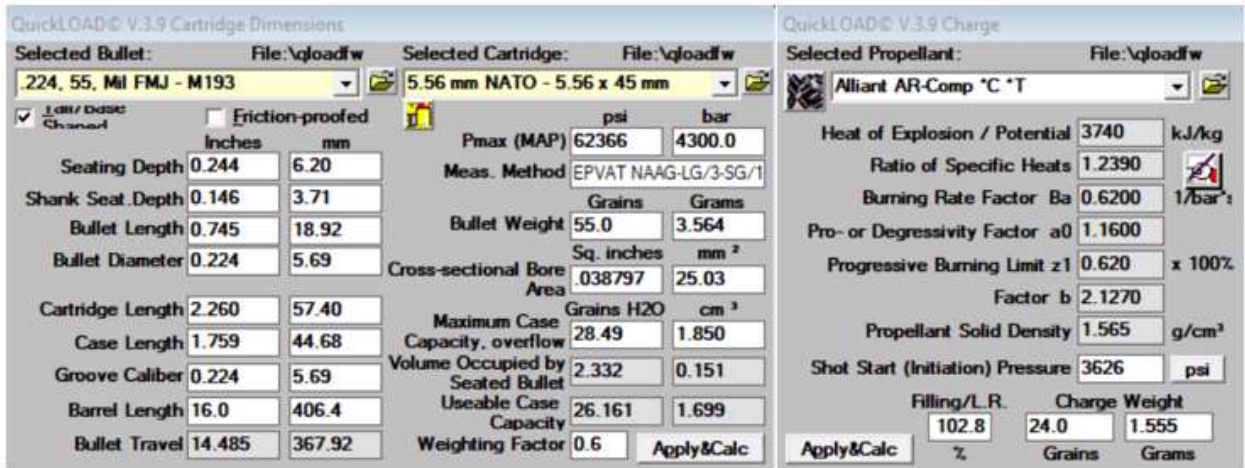


Figure A. 1: QuickLOAD 5.56 x 45 mm specifications.

Figure A.2 shows the user interface for quick ballistics results. Figures A.3 and A.4 show the calculated pressure – velocity curves.

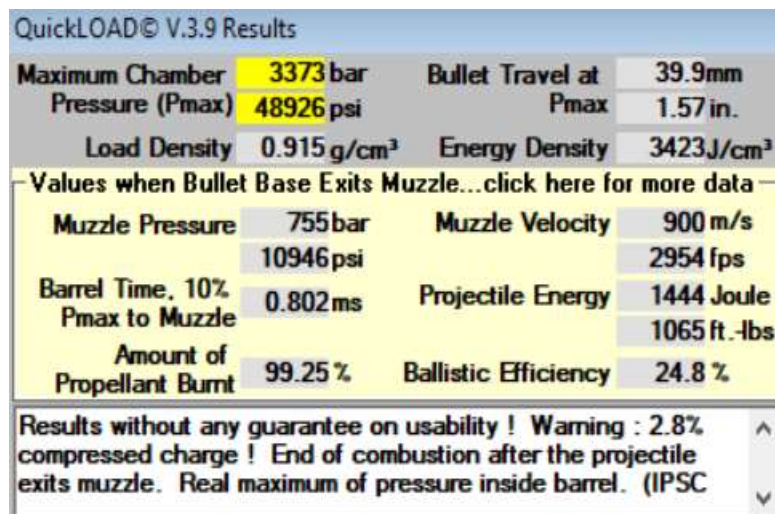


Figure A. 2: QuickLOAD 5.56 x 45mm result statistics.

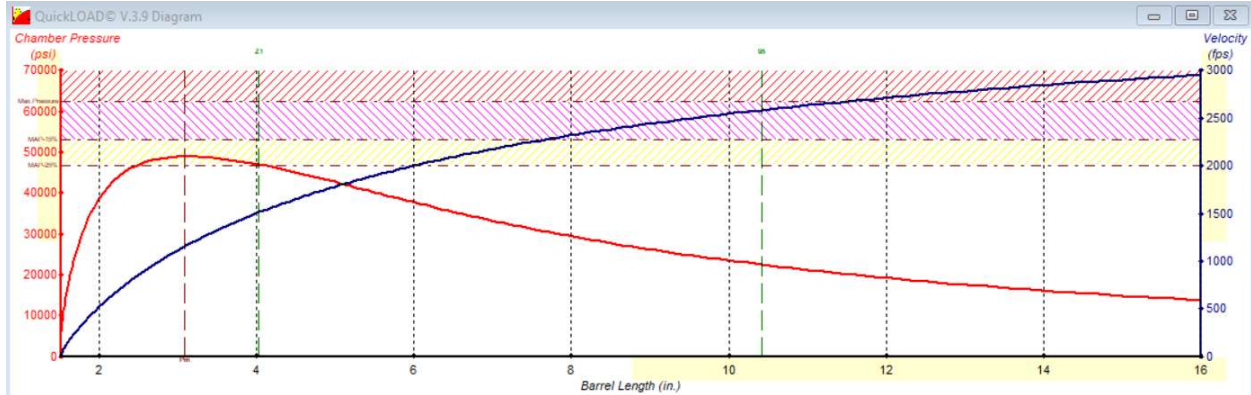


Figure A. 3: Pressure – velocity vs barrel length curves for 5.56 x 45 mm.

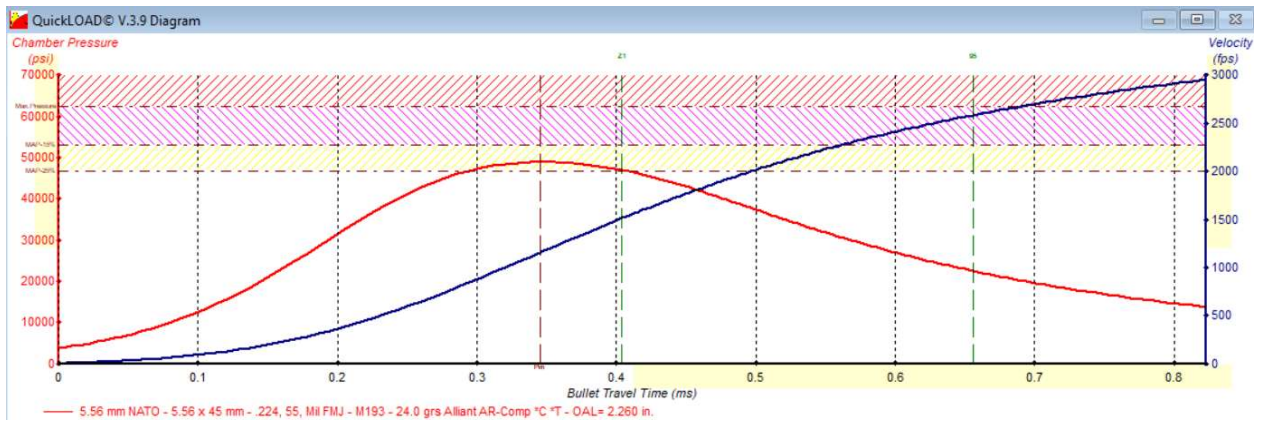


Figure A. 4: Pressure – velocity vs time curves for 5.56 x 45 mm.

## APPENDIX B. DETERMINATION OF PROPELLANT COMPOSITION AND COMBUSTION PRODUCTS

The composition of the solid propellant is determined using a material safety data sheet and iterative calculations. The SDS sheet specifies Nitrocellulose, Nitroglycerin, Di-isopentyl phthalate, Diphenylamine, and Urea. The SDS sheet provides a range for the weight percents of solid propellant constituents, which provides an estimate for the first iteration. The weight percents will be iteratively changed to converge onto the correct temperature, density, and heat of explosion provided by QuickLOAD.

The heat of formation for the solid propellant is

$$HF_{propellant} = \sum_i f_i HF_i \quad (\text{B.1.1})$$

where  $f_i$  is the mass fraction of a constituent (i.e. NC) and  $HF_i$  is the heat of formation for that constituent (Hunt, 1951, pg. 10).

For the products of combustion, determining the heat of explosion is more extensive. The adiabatic temperature ( $T_{ex}$ ), proportions of solid propellant constituents ( $f_{w,i}$ ), and gas density ( $1/V$ ) are inputs and initially assumed. Here, the adiabatic temperature and gas density is assumed based on data from similar propellants. The reaction is assumed to take place so rapidly at the high temperatures that the thermodynamic equilibrium is always maintained. Therefore, the C, H, N, and O content must be the same in the gas as in the solid propellant, and the ratios of the partial pressures can be determined by equilibrium constants (Hunt, 1951, pg. 10-11).

The major components of solid propellant combustion are  $CO_2$ ,  $H_2$ ,  $N_2$ ,  $CO$ , and  $H_2O$ . Present but less prevalent combustion products are  $OH$ ,  $H$ ,  $NO$ ,  $O_2$ ,  $O$ , and  $N$ .

$$\frac{\text{Product of partial pressures of second group}}{\text{Product of partial pressures of first group}} = K(T) = e^{-\Delta F/RT}, \quad (\text{B.1.2})$$

here  $\Delta F$  is the sum of the free energies of the second group minus the sum of the free energies of the first group (Hunt, 1951, pg. 11).

The equation of state for the gas is found using Hunt (1951) and Corner's (1950) method

$$P = \frac{nRT}{V} \left( 1 + \frac{B}{V} + \frac{nC}{V^2} \right), \quad (\text{B.1.3})$$

$$b = V \left[ 1 - \frac{n_0}{n} \left( 1 + \frac{B}{V} + \frac{nC}{V^2} \right) \right], \quad (\text{B.1.4})$$

$$B = (CO_2)B_{CO_2} + (CO)B_{CO} + \dots + (N_2)B_{N_2}, \quad (\text{B.1.5})$$

$$C = (CO_2)C_{CO_2} + (CO)C_{CO} + \dots + (N_2)C_{N_2}. \quad (\text{B.1.6})$$

B and C are linear functions of temperature and gas composition, b is the covolume of the products, n is the number of moles, and  $n_0$  is the value of n at explosion temperature.

$$n = \{C\} + \frac{1}{2}\{H\} + \frac{1}{2}\{N\} + \text{dissociated products} \quad (\text{B.1.7})$$

From equation B.1.2 for the partial pressures of the combustion products, the equilibrium constant can be found for the water-gas reaction. Let  $\{ \}$  denote the gram atoms per gram of an element and  $( )$  denote quantities in gram molecules per gram.

$$\frac{(CO)(H_2O)}{(CO_2)(H_2)} = K_0 = K_0(T) e^{\left\{ \frac{n\Delta B}{V} - \frac{n^2\Delta C}{2V^2} \right\}}, \quad (\text{B.1.8})$$

$$\Delta B = B_{CO} + B_{H_2O} - B_{CO_2} - B_{H_2}, \quad (\text{B.1.9})$$

$$\Delta C = C_{CO} + C_{H_2O} - C_{CO_2} - C_{H_2}. \quad (\text{B.1.10})$$

Now, a chemical balance can be performed, assuming no dissociation, for the major products of combustion. An iterative process is used to solve for the dissociated products of combustion from the major products of combustion. The iteration is complete when the composition of dissociated products remains the same as the previous iteration. The dissociated products subtract from the major products of combustion. The major products are

$$(N_2) = \frac{1}{2}\{N\}, \quad (\text{B.1.11})$$

$$(CO) + (CO_2) = \{C\}, \quad (\text{B.1.12})$$

$$(H_2) + (H_2O) = \frac{1}{2}\{H\}, \quad (\text{B.1.13})$$

$$(CO) + 2(CO_2) + (H_2O) = \{O\}. \quad (\text{B.1.14})$$

Where the dissociated products are

$$(OH) = \frac{(H_2O)}{\sqrt{(H_2)}} \left( \frac{V}{RT} \right)^{\frac{7}{11}} K_1(T) e^{\left( \frac{-20n}{V} \right)}, \quad (B.1.15)$$

$$(H) = \sqrt{(H_2)} \left( \frac{V}{RT} \right)^{\frac{7}{11}} K_5(T), \quad (B.1.16)$$

$$(NO) = \frac{(H_2O)\sqrt{(N_2)}}{(H_2)} \left( \frac{V}{RT} \right)^{\frac{7}{11}} K_2(T) e^{\left( \frac{-20n}{V} \right)}, \quad (B.1.17)$$

$$(O_2) = \left\{ \frac{(H_2O)}{(H_2)} \right\}^2 \left( \frac{V}{RT} \right) K_3(T), \quad (B.1.18)$$

$$(O) = \sqrt{(O_2)} \left( \frac{V}{RT} \right)^{\frac{7}{11}} K_4(T), \quad (B.1.19)$$

$$(N) = \sqrt{(N_2)} \left( \frac{V}{RT} \right)^{\frac{7}{11}} K_6(T). \quad (B.1.20)$$

After the composition of the combustion products is found, the internal energy (U) of the gas can be calculated using Corner's method,

$$U = U_0 + \left( \frac{n}{V} \right) U_1 + \left( \frac{n}{V} \right)^2 U_2. \quad (B.1.21)$$

$U_0$  is the internal energy at constant volume computed from the mean molecular heat, see Table 2.05 in *Internal Ballistics*.

The heat of formation of the combustion products is

$$HF_{products} = \sum_i y_i HF_{products,i}, \quad (B.1.22)$$

which can be used to calculate the heat of explosion

$$HE = HF_{products} - HF_{propellant}. \quad (B.1.23)$$

If the adiabatic temperature has been chosen correctly, the internal energy will equal the heat of explosion. If the adiabatic temperature and composition have been chosen correctly, then the calculated heat of explosion will match the heat of explosion found in QuickLOAD. The chemical composition of the solid propellant is provided in Table B.1, with the resulting gas composition is provided in Table B.2.

Table B. 1: Solid Propellant Composition.

Propellant Constituent	Composition, $f_i$	Formula
Nitrocellulose, 13.5 % N	77 %	$C_6H_7O_2(OH)_{3-s}(ONO_2)_s$
Nitroglycerin	16 %	$C_3H_5N_3O_9$
Di-isopentyl phthalate	3 %	$C_{18}H_{26}O_4$
Diphenylamine	2 %	$C_{12}H_{11}N$
Urea	2 %	$CH_4N_2O$

Table B. 2: Products of Combustion Composition.

Product	Molar Fraction, $y_i$
N <sub>2</sub>	0.1259
CO	0.4340
H <sub>2</sub>	0.1081
H <sub>2</sub> O	0.2320
CO <sub>2</sub>	0.0950
OH	0.0025
H	0.0020
NO	0.0002
O <sub>2</sub>	0.0002
O	6.1E-05
N	3.1E-05

Table B. 3: Calculated Gas Properties.

Result	Value	Units
Internal Energy	885.6	<i>cal/g</i>
Heat of formation of Propellant	492.4	<i>cal/g</i>
Heat of formation of Products	1388.7	<i>cal/g</i>
Heat of Explosion	896.4	<i>cal/g</i>
Molecular Weight of Gas.	24.32	<i>g/mol</i>
Adiabatic Temperature	3200	<i>K</i>
Explosion Pressure	$2.41 \times 10^8$	<i>Pa</i>
Density	.20	<i>g/cc</i>
Ballistic Efficiency	.20	<i>ul</i>
Percent Error Calculated	1.2 %	<i>ul</i>

Table B.3 displays the results of the combustion analysis. QuickLOAD provides a heat of explosion of  $3740 \text{ kJ/kg}$ , or  $893.9 \text{ cal/g}$ . This results in a 0.30 % error between the calculated heat of explosion and that provided by QuickLOAD.

## APPENDIX C. SPECIFICATION OF MATERIAL PROPERTIES

The barrel material is AISI 4150 with no chrome lining, this is the case for the barrel of the test weapon. However, the barrels used in the study conducted by Windham (1994, 1996) likely have chrome lined barrels, as that configuration is standard for military M4 Carbines. The versions of ANSYS used in this study are 2020 R1 and 2021 R1. These versions of ANSYS does not have the capability of evaluating nodal temperature dependent ultimate strength or yield strength. However, these versions of ANSYS can evaluate temperature dependent specific heat, thermal conductivity, Young's Modulus, and other material properties. Due to this limitation, the temperature dependent material strength data, shown in Figure C.1, from *METALLIC MATERIALS AND ELEMENTS FOR AEROSPACE VEHICLE STRUCTURES* requires a curve fit equation to be input into ANSYS.

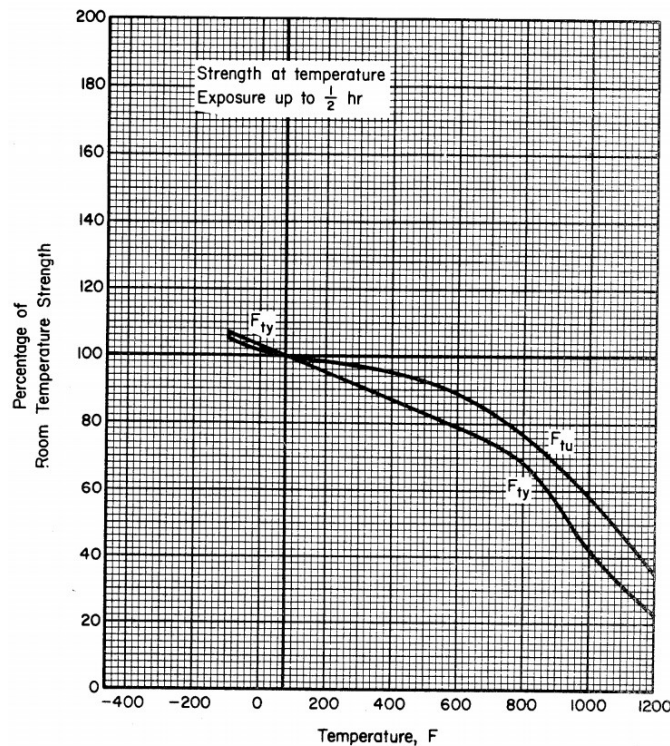


FIGURE 2.3.1.1.1. Effect of temperature on the tensile ultimate strength ( $F_{tu}$ ) and tensile yield strength ( $F_{ty}$ ) of AISI low-alloy steels (all products).

Figure C. 1: Material strength from METALLIC MATERIALS AND ELEMENTS FOR AEROSPACE VEHICLE STRUCTURES.

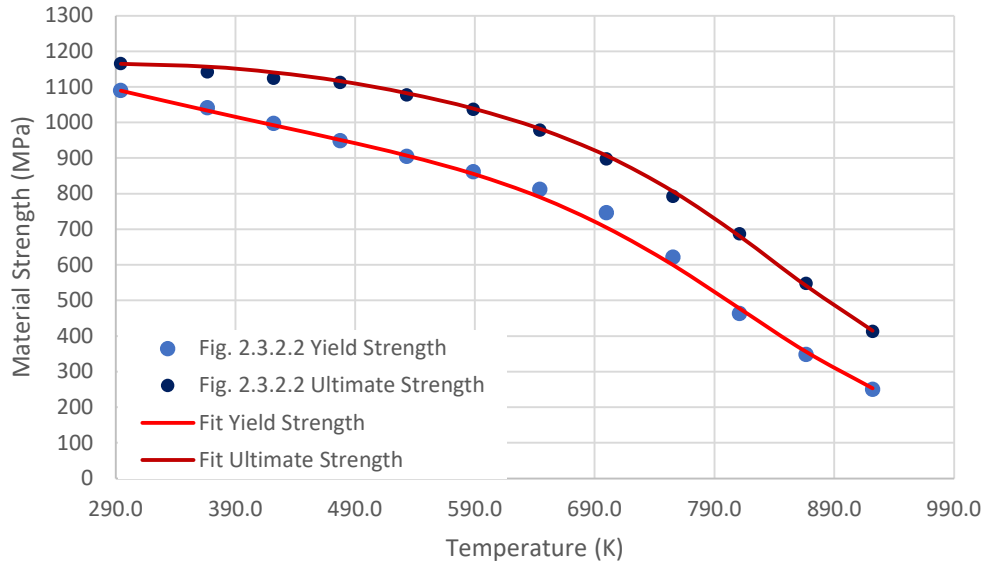


Figure C. 2: Tensile ultimate strength and tensile yield strength vs temperature for AISI 4150.

Figure C.2 shows the resulting curve fit for the material strength. The curve fit equation is of the form used in *Temperature-Dependent Material Modeling for Structural Steels: Formulation and Application*. Table C.1 provides the percent error of the curve fit.

Table C. 1: Material strength curve fit percent error.

Temperature (K)	Percent Error, Yield Strength	Percent Error, Ultimate Strength
294.3	-0.1%	0.0%
366.5	-0.7%	1.4%
422.0	-0.5%	1.5%
477.6	0.3%	0.3%
533.2	0.3%	0.5%
588.7	-0.7%	0.2%
644.3	-2.7%	0.3%
699.8	-5.6%	1.1%
755.4	-3.6%	1.8%
810.9	3.1%	-1.0%
866.5	2.0%	-1.2%
922.0	1.0%	0.4%

There are four popular methods for rifling barrels; cut rifling, button rifling, hammer forging, and electro-chemical machining (ECM). The rifling process used influences what hardness of material can be formed. Generally, cut rifling allows for Rockwell C values in the high 30's to low 40's. Button rifling allows for Rockwell C values in the high 20's to low 30's. Hammer forging allows for Rockwell C ranges in the mid 30's, and ECM has no material hardness limitations. The assumption was made that the M4 Carbine barrels tested by Windham were cut rifled. However, there is no source specifying Colt's rifling process for M4 Carbine barrels. The Rockwell C hardness assumed in this study was 36. The user interface for creating a new material, and adding material properties to existing materials, is shown in Figure C.3.

Properties of Outline Row 12: Steel, AISI 4150, MIL-B-11595, Normalized 870C			
	A	B	C
1	Property	Value	Unit
2	Density	7861.1	kg m <sup>-3</sup>
3	Isotropic Secant Coefficient of Thermal Expansion		
8	Isotropic Elasticity	Tabular	
18	Tensile Yield Strength	Tabular	
21	Tensile Ultimate Strength	Tabular	
24	Isotropic Thermal Conductivity	Tabular	
27	Specific Heat, C <sub>p</sub>	Tabular	

Figure C. 3: ANSYS material properties menu.

The specific heat and thermal conductivity of AISI 4150, shown in Figure C.4, were available in the ANSYS Granta Materials Library and did not require curve fit equations.

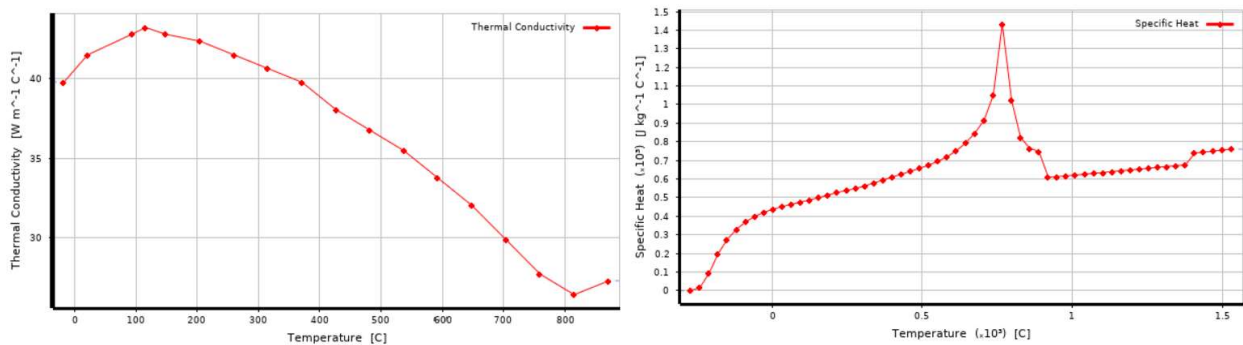


Figure C. 4: Thermal conductivity and specific heat capacity for AISI 4150.

## APPENDIX D. EXTERNAL AND INTERNAL HEAT TRANSFER COEFFICIENTS

Figure D.1 provides information on the mass flow of propellant gas, mean gas density, and motion of exhaust gas from the breech.

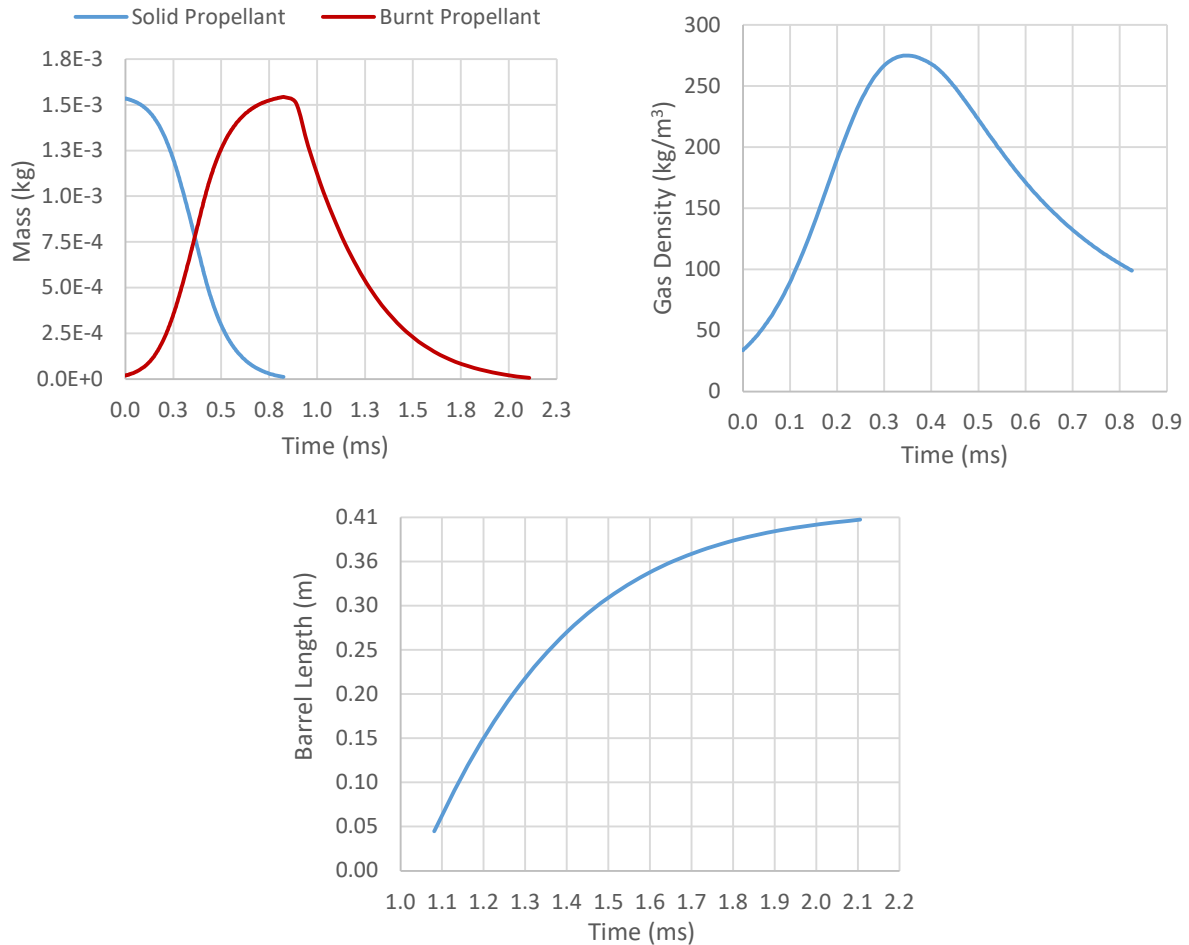


Figure D. 1: Propellant Mass Flow and Density of Combustion Products.

Figures D.2 and D.3 provide the local gas velocity and relationship between the Nusselt Number and Reynolds number for verifying boundary layer coefficients.

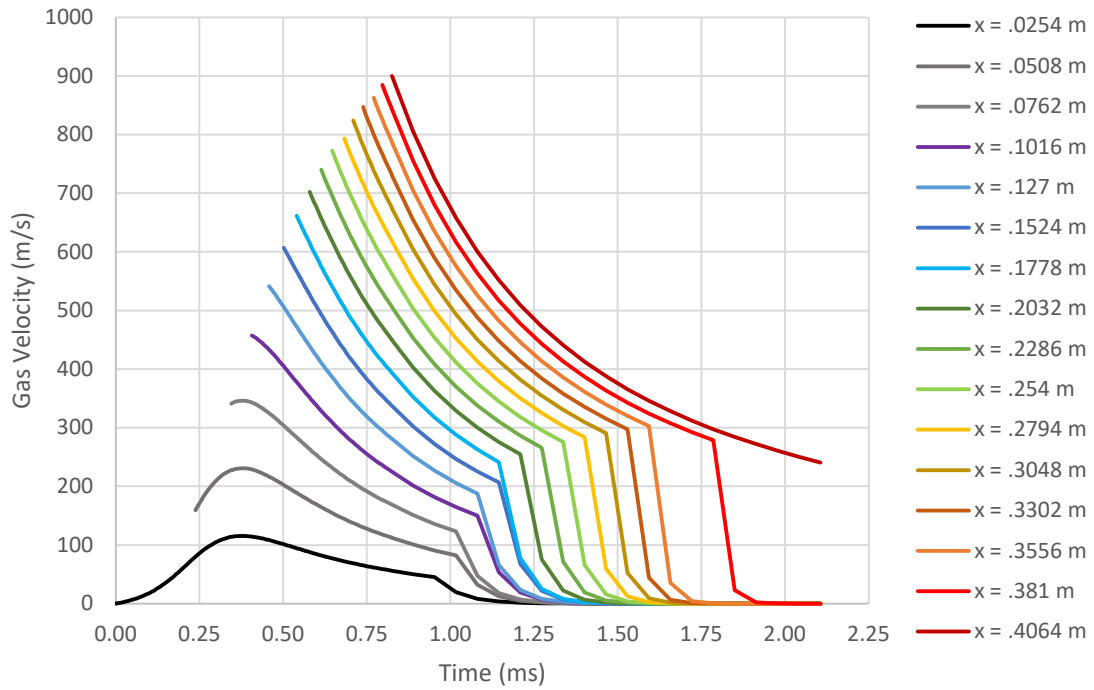


Figure D. 2: Velocity of Combustion Products vs Time.

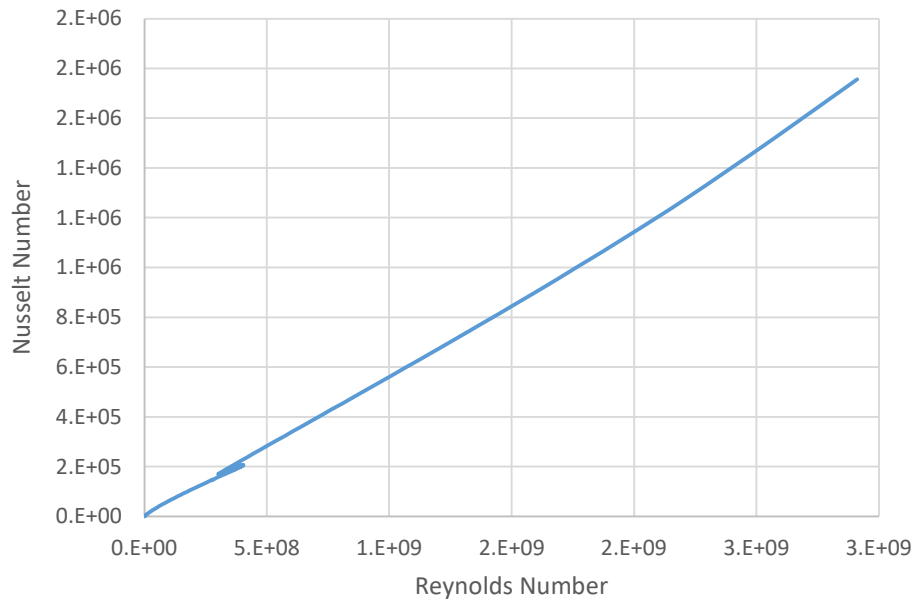


Figure D. 3: Nusselt Number vs Reynolds Number.

Figures D.4 to D.7 show the transient heat transfer coefficient and boundary layer growth of the combustion products at various distances along the barrel during firing.

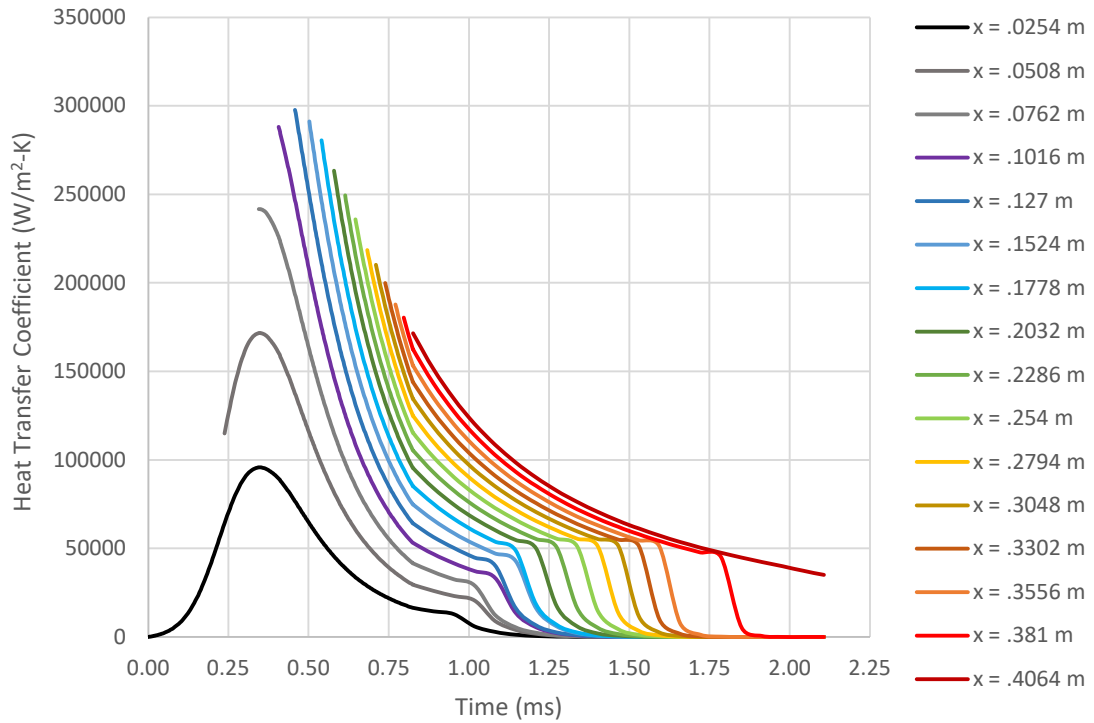


Figure D. 4: Transient internal heat transfer coefficients.

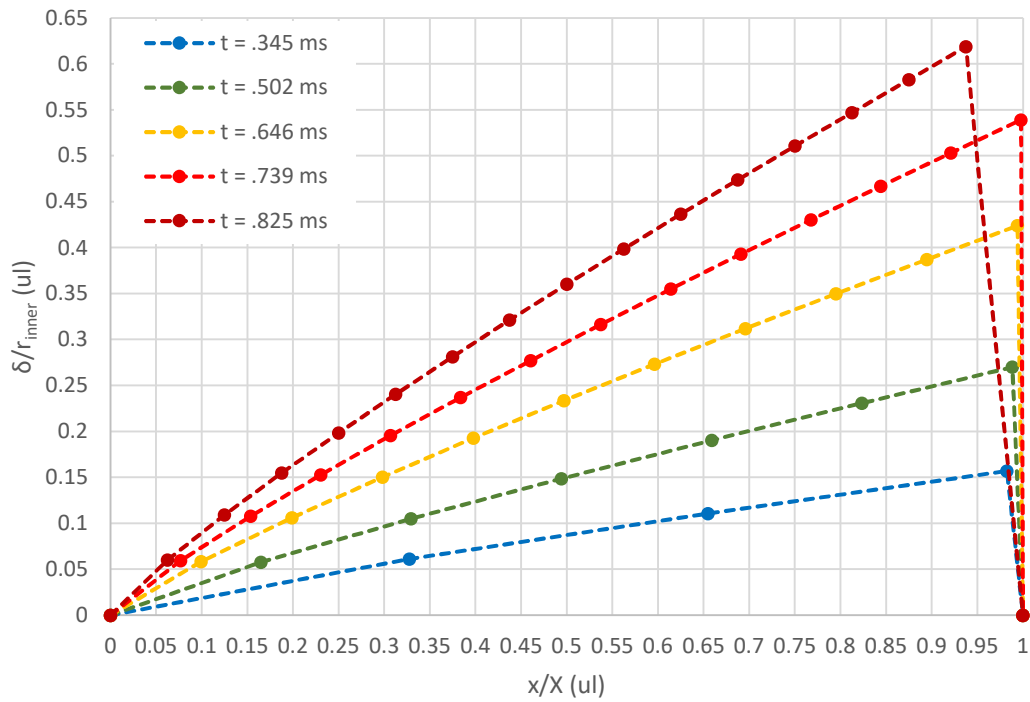


Figure D. 5: Boundary layer thickness vs projectile position.

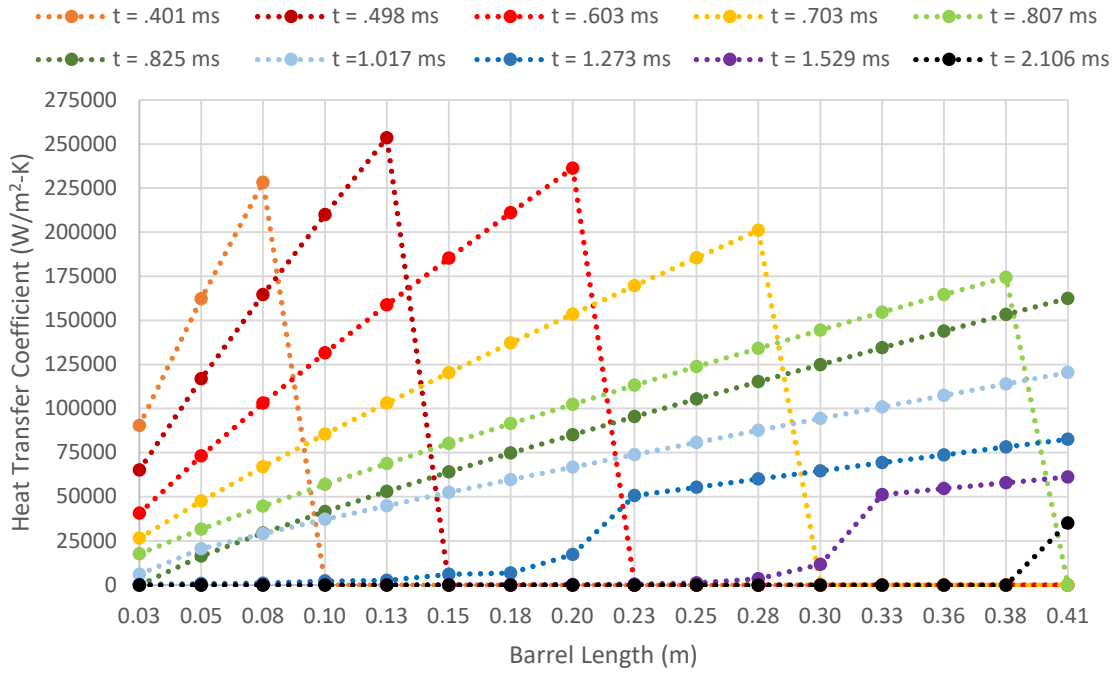


Figure D. 6: Spatial internal heat transfer coefficients.

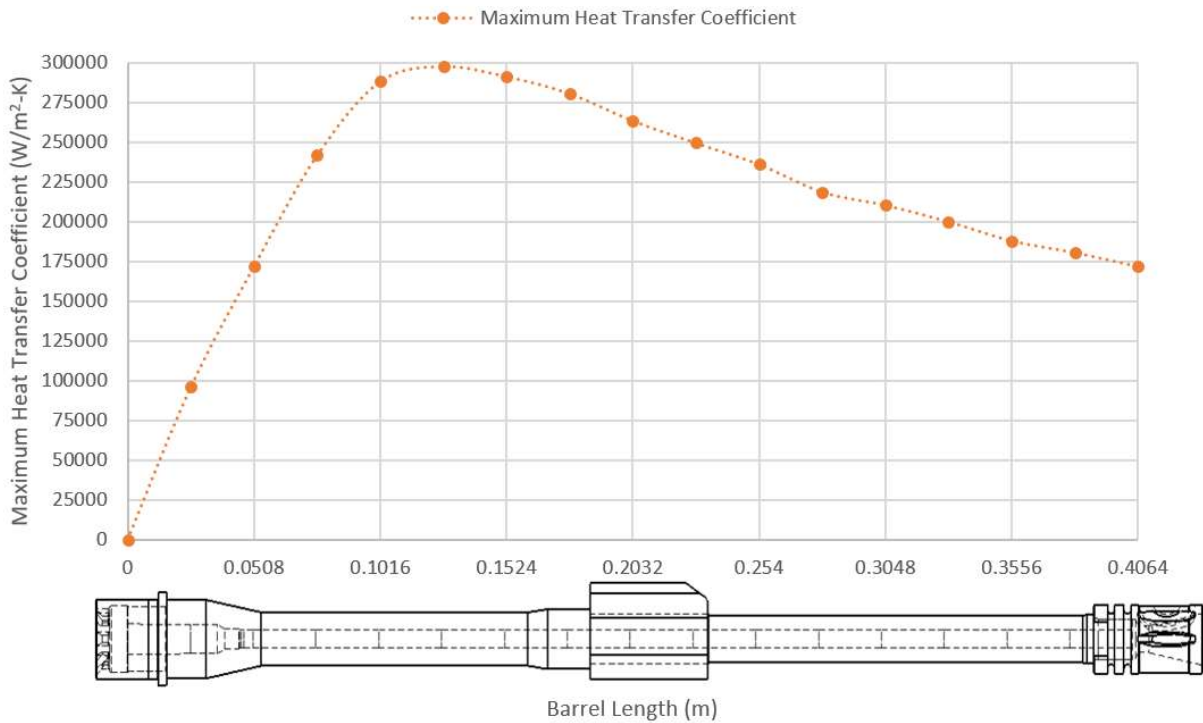


Figure D. 7: Maximum local internal heat transfer coefficients.

Figure D.8 provides the properties of the combustion products.

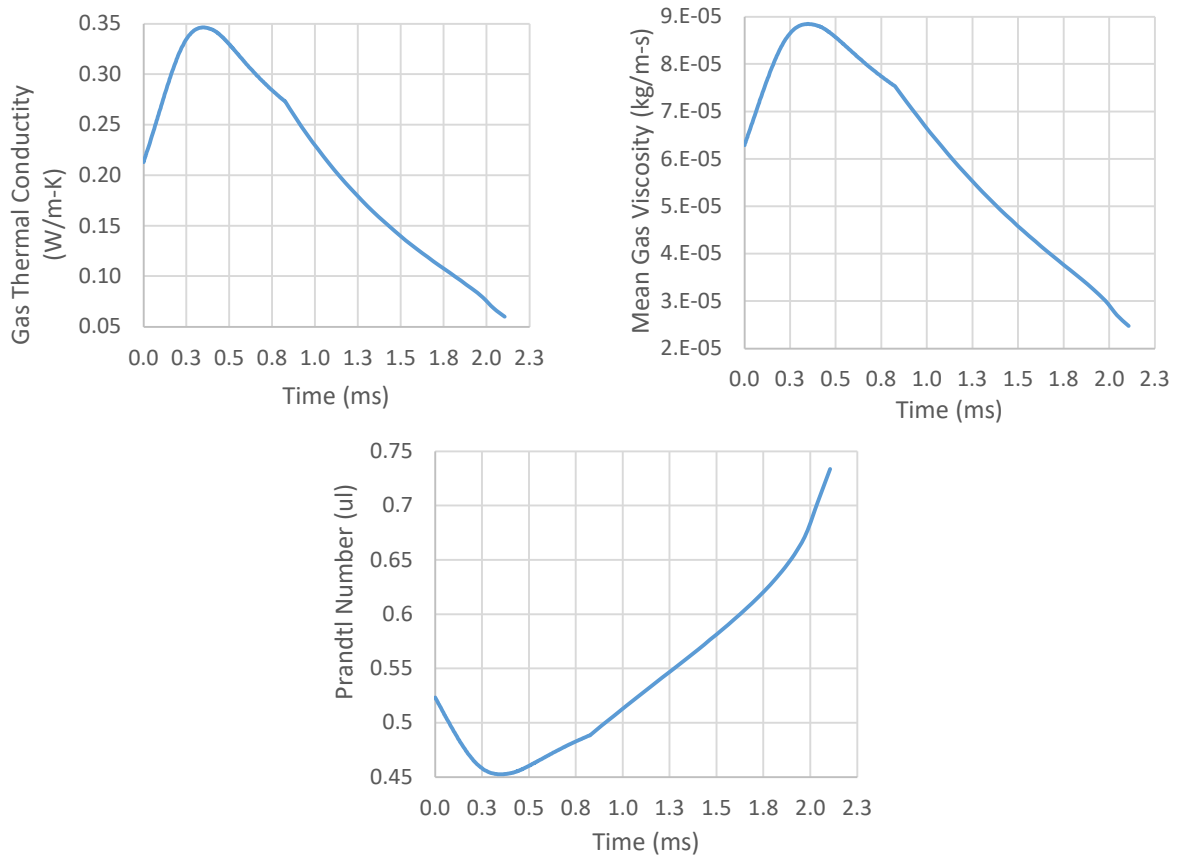


Figure D. 8: Propellant gas properties during combustion.



# APPENDIX F. DATA FROM EXPERIMENTS PERFORMED BY JEFF WINDHAM

## F.1.1 Data Comparison

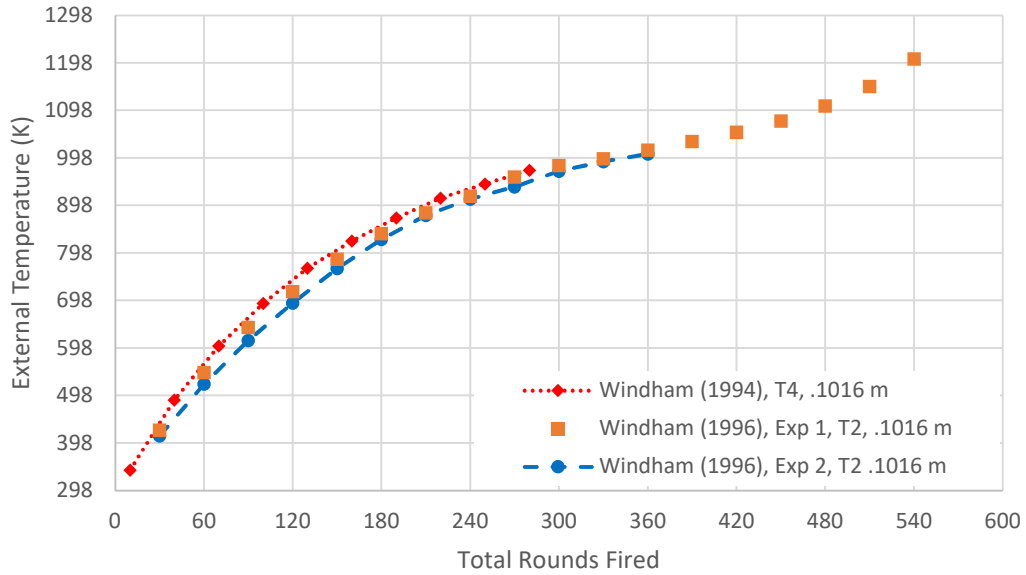


Figure F. 1: Peak burst temperatures for an M4A1 at .1016 m.

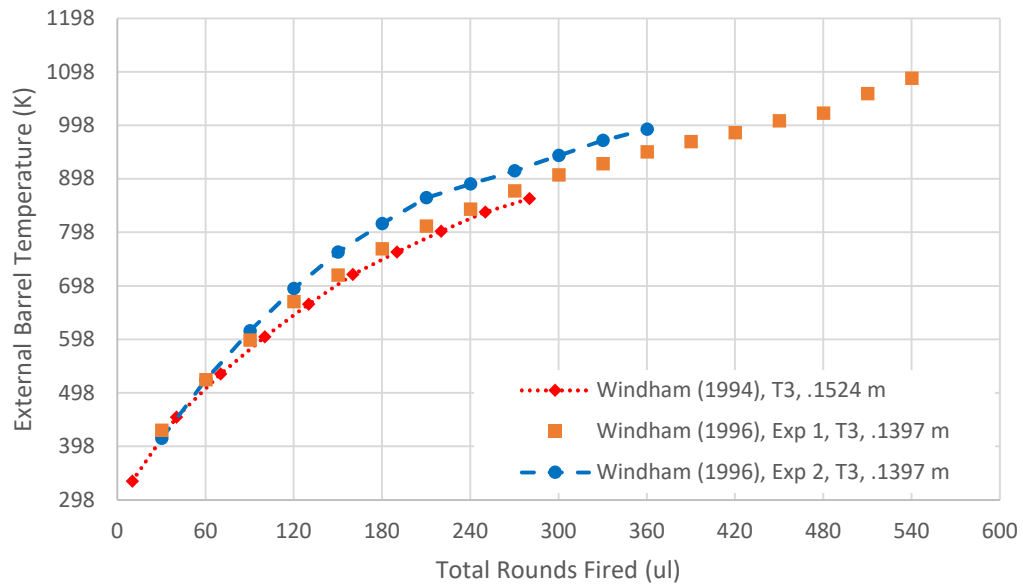


Figure F. 2: Peak burst temperatures for an M4A1 at .1524 m and .1397 m.

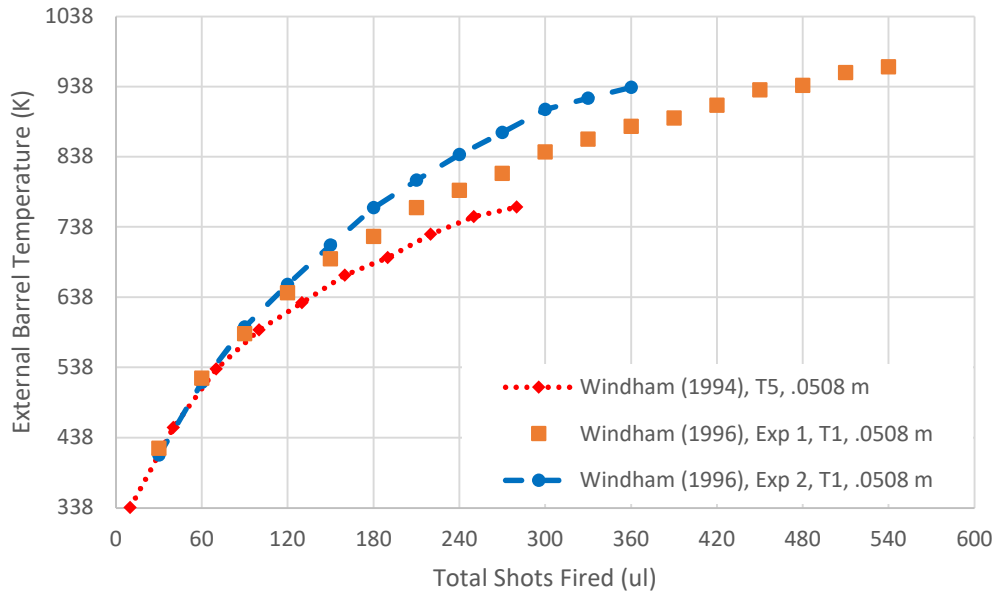


Figure F. 3: Peak burst temperatures for an M4A1 at .0508 m.

### F.2.1 External Barrel and Handguard Temperature of the 5.56mm M4 Carbine (1994):

Table F. 1: Peak burst temperature data from Windham (1994).

Thermocouple	T1 (°F)	T1 (K)	T2 (°F)	T2 (K)	T3 (°F)	T3 (K)	T4 (°F)	T4 (K)
Shots	12 (inches)	0.3048 (m)	9 (inches)	0.2286 (m)	6 (inches)	0.1524 (m)	4 (inches)	0.1016 (m)
10	122	323	118	321	140	333	155	341
40	290	416	272	406	355	453	420	489
70	420	489	390	472	500	533	625	603
100	540	555	492	529	625	603	786	692
130	645	614	575	575	735	664	920	766
160	740	666	650	616	835	719	1022	823
190	810	705	725	658	910	761	1110	872
220	890	750	780	689	980	800	1185	914
250	955	786	840	722	1045	836	1238	943
280	1015	819	895	753	1090	861	1290	972

Table F. 2: Continued: Peak burst temperature data from Windham (1994).

Thermocouple	T5 (°F)	T5 (K)	T6 (°F)	T6 (K)
Shots	2 (inches)	0.0508 (m)	1 (inch)	0.0254 (m)
10	150	339	80	300
40	355	453	135	330
70	505	536	205	369
100	605	591	260	400
130	675	630	300	422
160	745	669	340	444
190	790	694	362	456
220	850	728	390	472
250	895	753	415	486
280	920	766	448	504

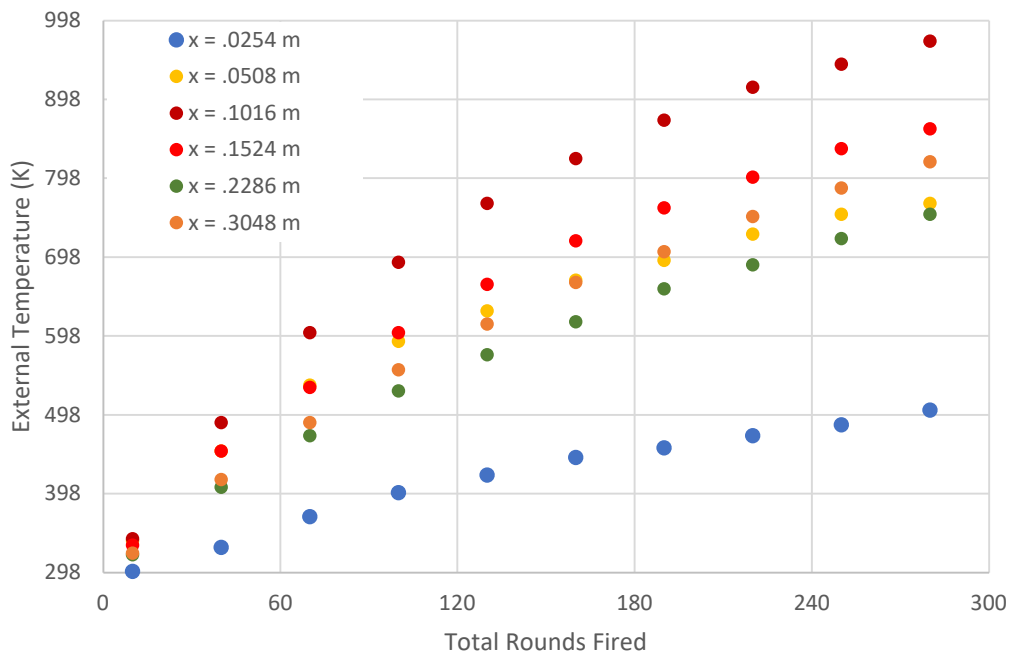


Figure F. 4: Peak burst temperature data from Windham (1994).

### F.3.1 Fire to Destruction Test of 5.56mm M4A1 Carbine and M16A2 Rifle Barrels (1996)

Table F. 3: Peak burst temperature data from experiment 1 by Windham (1996).

Thermocouple	T1 (°F)	T1 (K)	T2 (°F)	T2 (K)	T3 (°F)	T3 (K)	T4 (°F)	T4 (K)
Shots (ul)	2 (inches)	.0508 (m)	4 (inches)	.1016 (m)	5.5 (inches)	.1397 (m)	11 (inches)	.2974 (m)
30	302	423	306	426	311	428	263	401
60	481	523	525	547	481	523	394	474
90	595	586	696	642	615	597	516	542
120	700	644	831	717	744	669	613	596
150	788	693	954	785	833	718	700	644
180	844	724	1050	839	921	767	788	693
210	919	766	1129	882	998	810	866	737
240	963	790	1192	918	1054	841	919	766
270	1006	814	1264	958	1116	875	963	790
300	1061	845	1308	982	1170	906	1008	816
330	1094	863	1334	997	1208	926	1050	839
360	1127	881	1367	1015	1247	948	1085	858
390	1148	893	1400	1033	1282	968	1098	865
420	1181	912	1435	1053	1313	985	1120	878
450	1221	933	1477	1076	1352	1006	1138	887
480	1232	940	1533	1107	1378	1021	1142	890
510	1264	958	1608	1149	1444	1057	1159	899
540	1279	966	1712	1206	1495	1086	1163	901

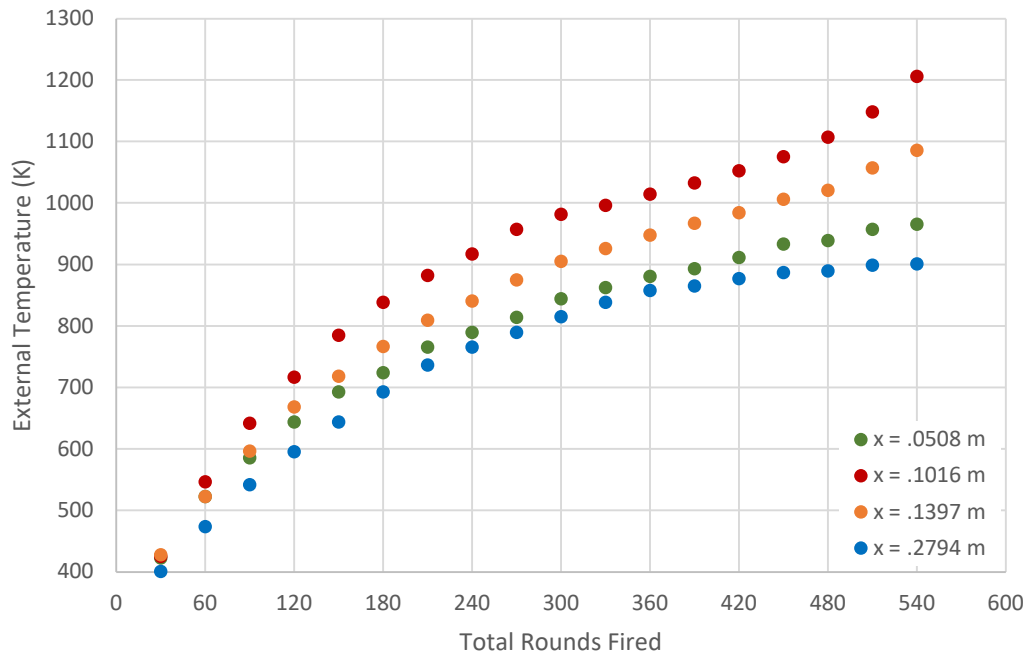


Figure F. 5: Peak burst temperature data from experiment 1 by Windham (1996).

Table F. 4: Peak burst temperature data from experiment 2 by Windham (1996).

Thermocouple	T1 (°F)	T1 (K)	T2 (°F)	T2 (K)	T3 (°F)	T3 (K)	T4 (°F)	T4 (K)
Shots (ul)	2 (inches)	.0508 (m)	4 (inches)	.1016 (m)	5.5 (inches)	.1397 (m)	11 (inches)	.2974 (m)
30	284	413	284	413	284	413	258	399
60	470	517	481	523	481	523	383	468
90	613	596	645	614	645	614	492	529
120	722	656	788	693	788	693	613	596
150	823	712	919	766	910	761	702	645
180	919	766	1028	827	1006	814	798	699
210	989	805	1120	878	1094	863	877	743
240	1054	841	1181	912	1140	889	954	785
270	1111	873	1227	937	1183	913	1006	814
300	1170	906	1286	970	1236	942	1050	839
330	1199	921	1323	991	1286	970	1098	865
360	1227	937	1352	1006	1323	991	1133	885

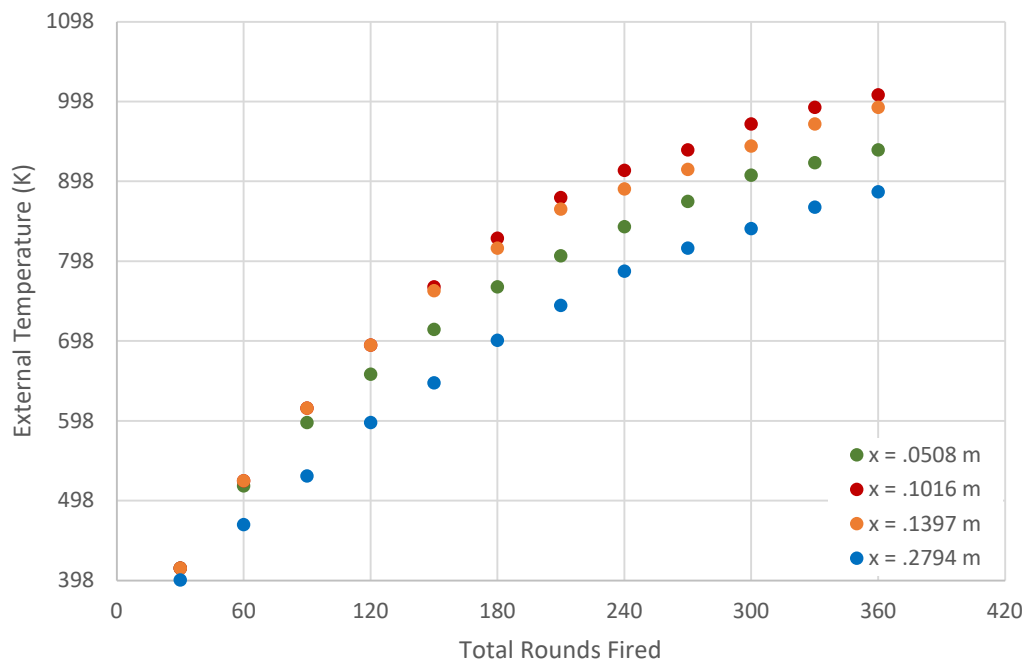


Figure F. 6: Peak burst temperature data from experiment 2 by Windham (1996).

## APPENDIX G. THERMAL CAMERA DATA

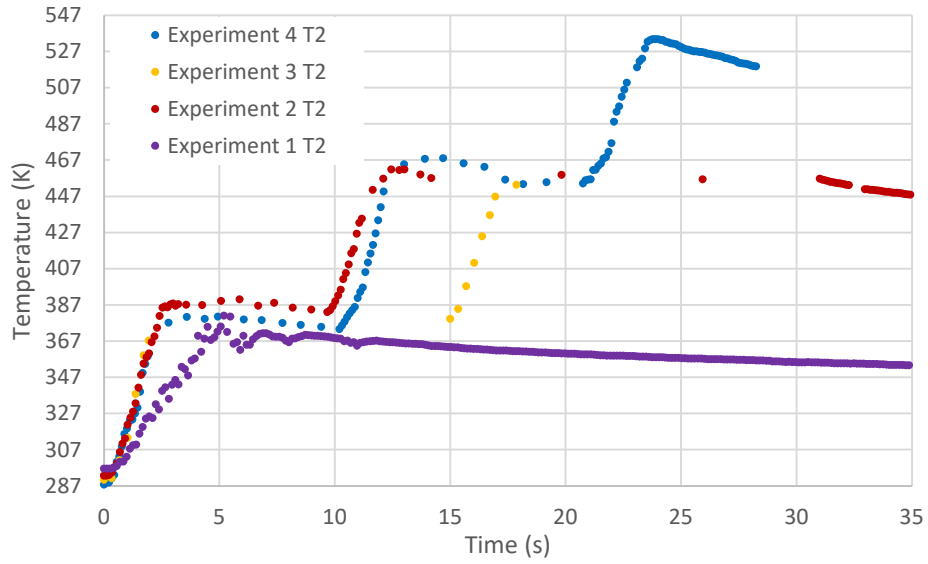


Figure G. 1: Transient temperature at .0508 m.

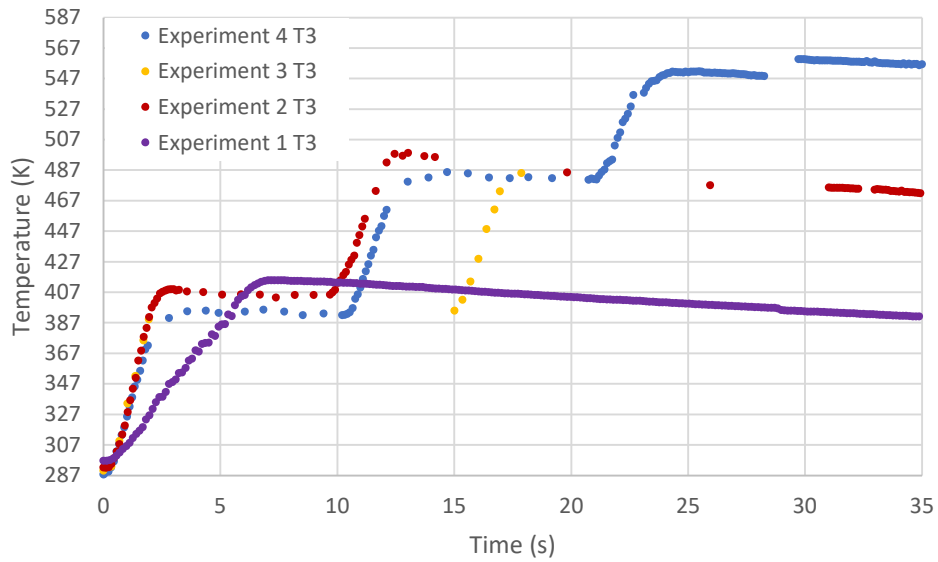


Figure G. 2: Transient temperature at .0762 m.

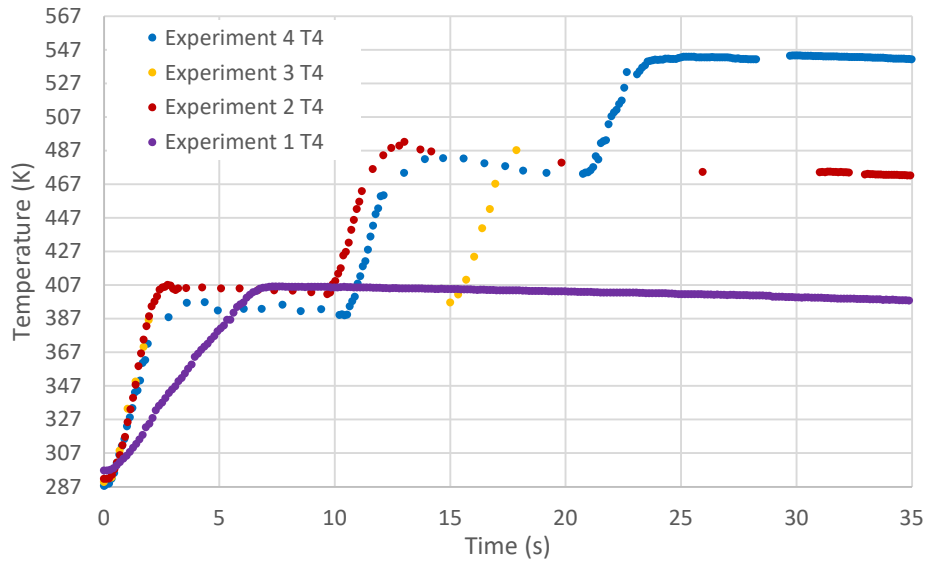


Figure G. 3: Transient temperature at .1016 m.

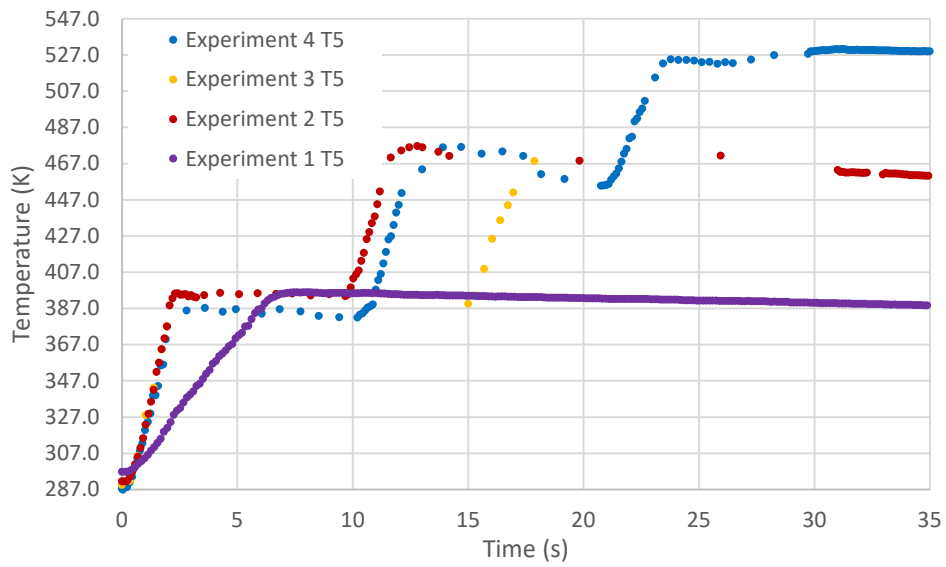


Figure G. 4: Transient temperature at .127 m.

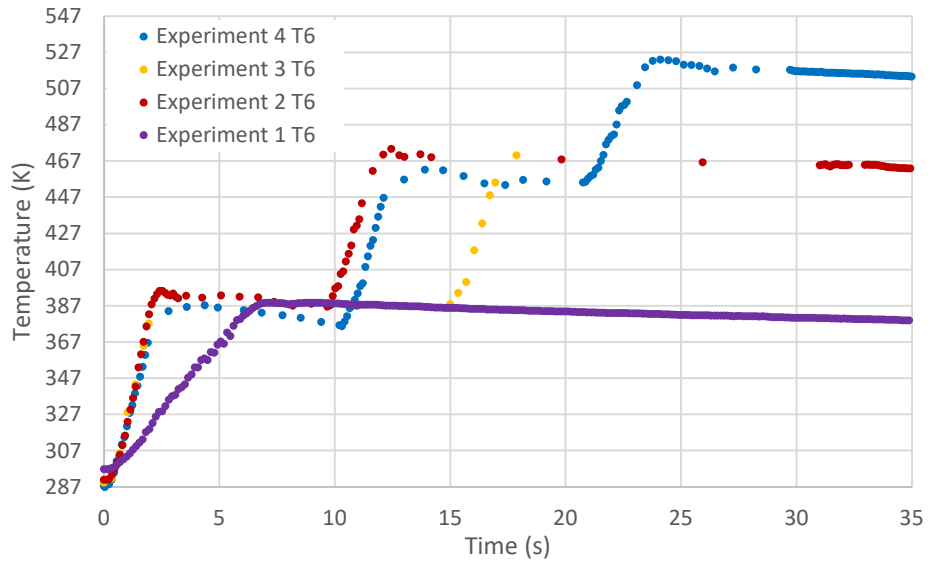


Figure G. 5: Transient temperature at .1524 m.

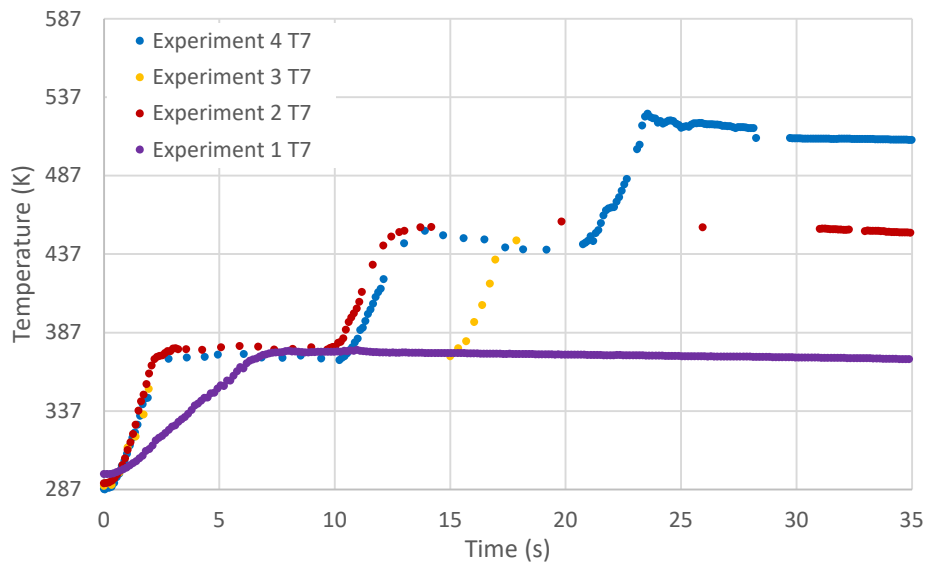


Figure G. 6: Transient temperature at .1778 m.

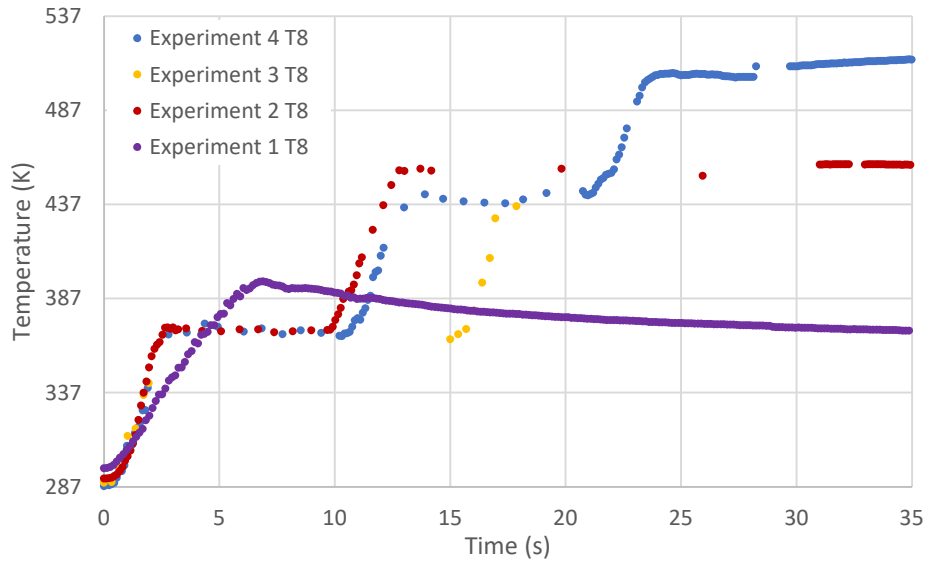


Figure G. 7: Transient temperature at .2032 m.

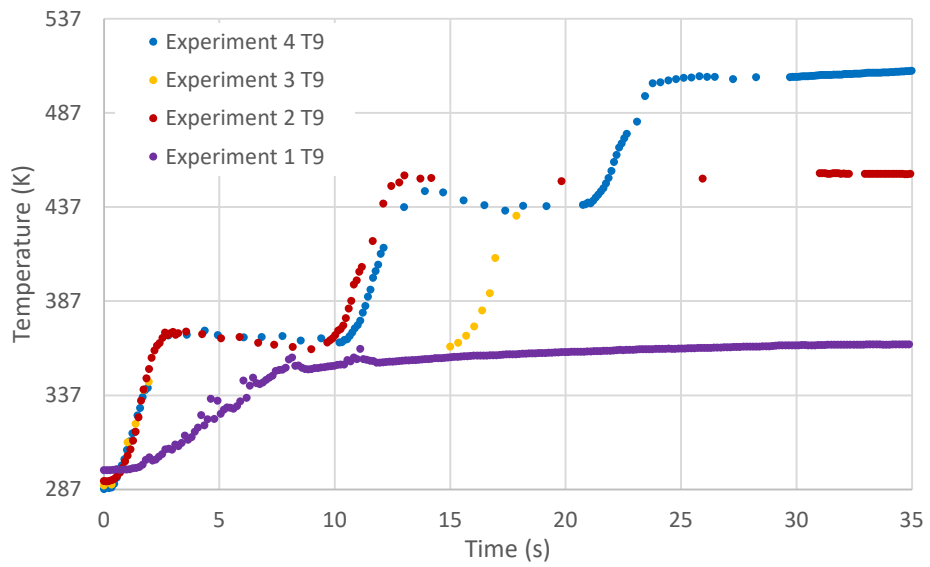


Figure G. 8: Transient temperature at .2286 m.

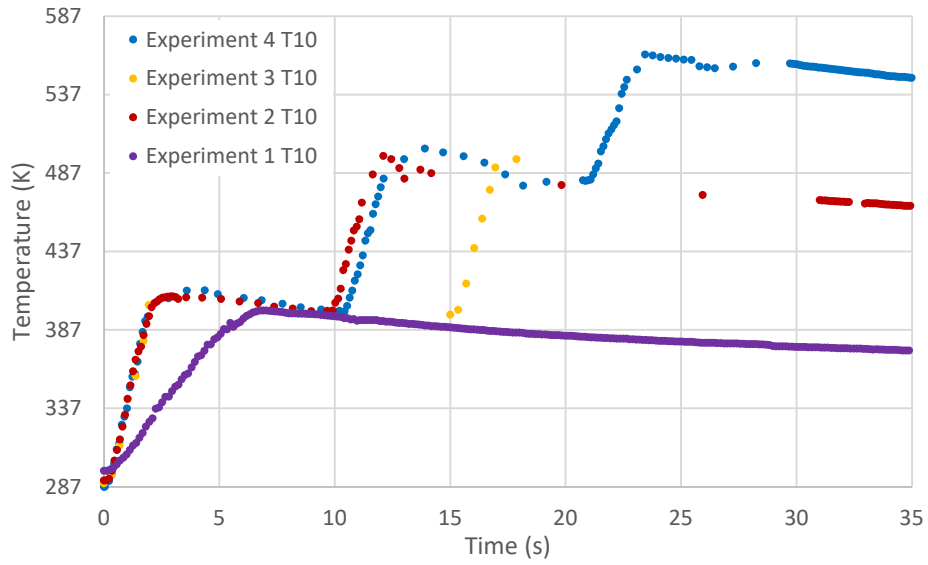


Figure G. 9: Transient temperature at .254 m.

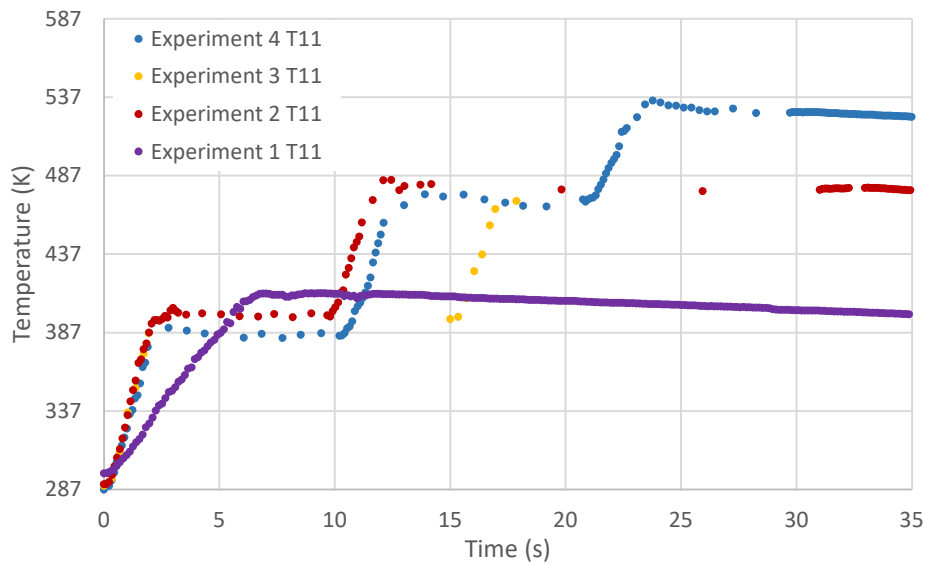


Figure G. 10: Transient temperature at .2794 m.

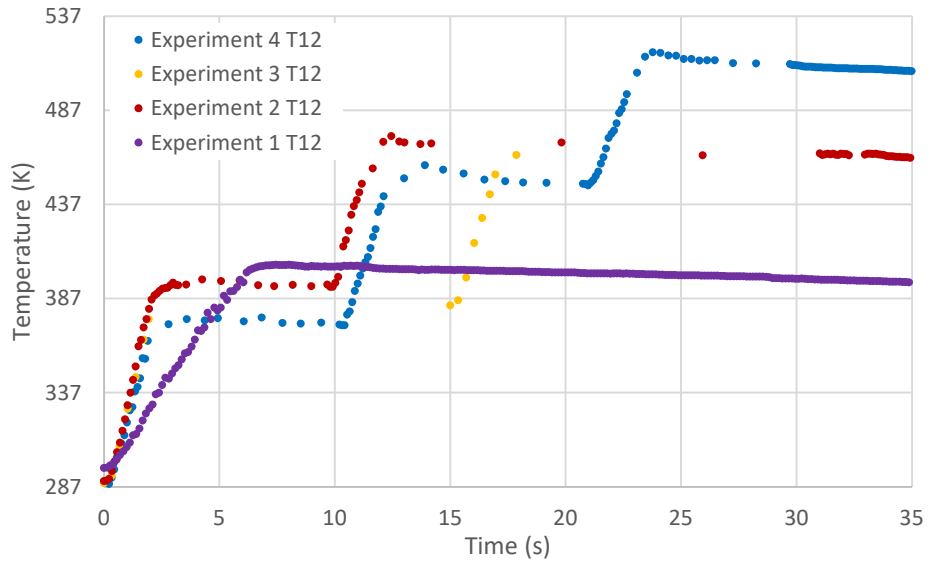


Figure G. 11: Transient temperature at .3048 m.

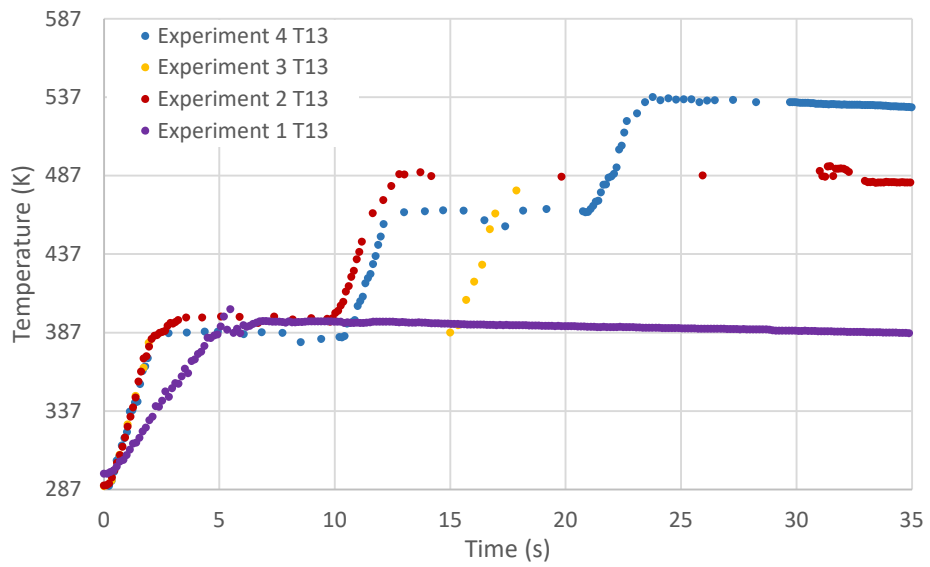


Figure G. 12: Transient temperature at .3302 m.

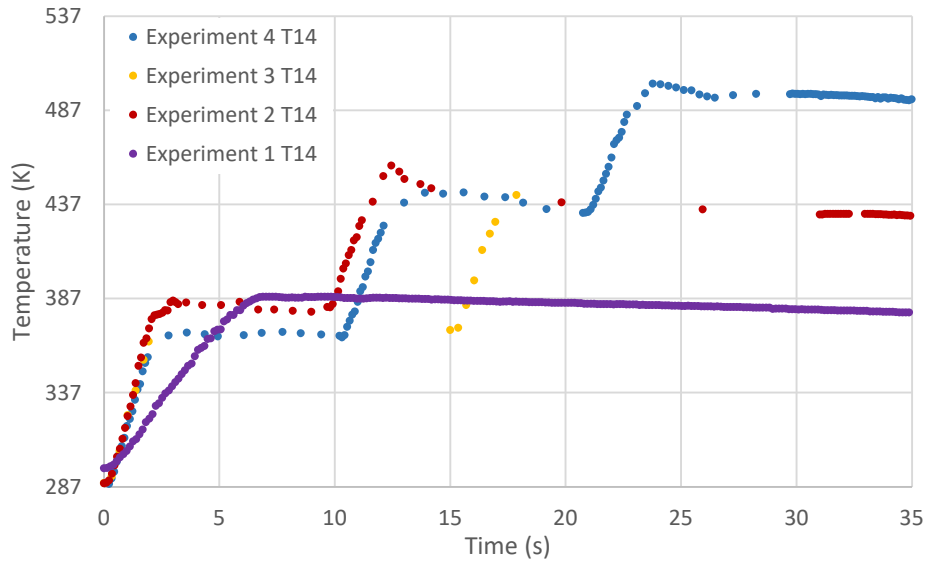


Figure G. 13: Transient temperature at .3556 m.

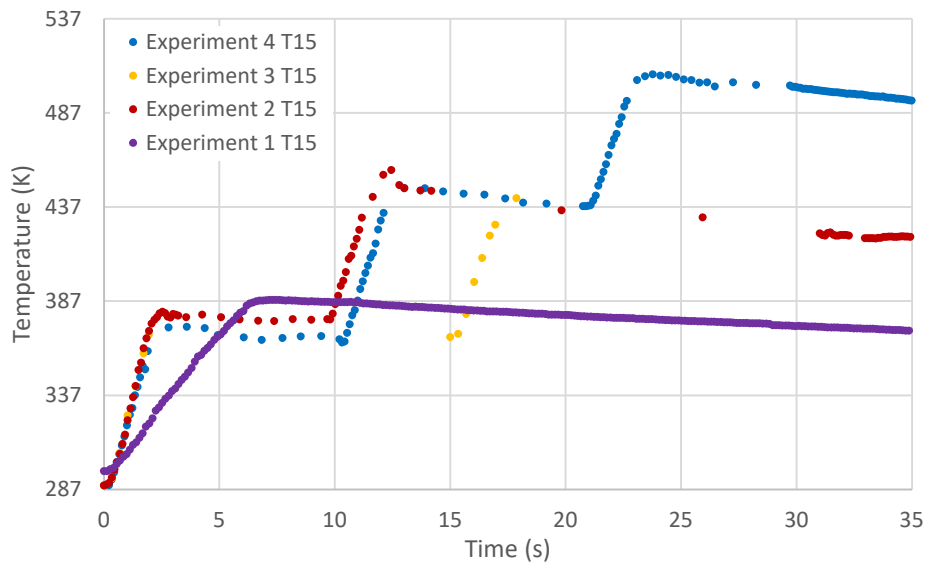


Figure G. 14: Transient temperature at .381 m.

## APPENDIX H. VERIFICATION RESULTS

### H.1.1 Mesh independence

Table H. 1: Maximum external temperature for T2 – T8 for various element sizes.

Element Size (m)	T2 (m)	T3 (m)	T4 (m)	T5 (m)	T6 (m)	T7 (m)	T8 (m)
0.0508	0.0508	0.0762	0.1016	0.127	0.1524	0.1778	0.2032
.002540	400.6	412.7	412.3	406.4	402.8	378.6	367.5
.001270	405.8	420.5	418.2	410.4	405.4	379.5	369.0
.000635	400.4	415.1	413.1	405.8	401.0	375.4	365.6

Table H. 2: Maximum external temperature for T9 - T15 for various element sizes.

Element Size (m)	T9 (m)	T10 (m)	T11 (m)	T12 (m)	T13 (m)	T14 (m)	T15 (m)
0.2286	0.2286	0.2540	0.2794	0.3048	0.3302	0.3556	0.3810
.002540	373.9	425.8	423.2	420.5	413.5	412.3	408.3
.001270	373.4	426.9	424.9	422.8	415.7	415.2	411.4
.000635	371.0	420.7	418.7	416.4	410.5	409.1	405.6

### H.2.1 Transient Discretization

Table H. 3: Maximum external temperature for T2 - T8 for various time steps.

Number of Time Steps	T2 (m)	T3 (m)	T4 (m)	T5 (m)	T6 (m)	T7 (m)	T8 (m)
0.0508	0.0508	0.0762	0.1016	0.127	0.1524	0.1778	0.2032
200	405.2	416.9	413.1	409.1	403.6	376.8	366.8
150	402.7	415.0	411.5	407.1	401.1	374.3	365.2
120	402.4	414.5	410.5	405.8	400.1	373.6	364.5
75	405.8	420.5	418.2	410.4	405.4	379.5	369.0
50	399.2	410.6	407.4	399.6	400.2	379.8	365.0
30	392.8	400.7	394.6	383.5	383.5	366.4	357.2

Table H. 4: Maximum external temperature for T9 - T15 for various time steps.

Number of Time Steps	T9 (m)	T10 (m)	T11 (m)	T12 (m)	T13 (m)	T14 (m)	T15 (m)
200	368.7	416.0	412.6	411.4	409.9	409.2	405.0
150	367.7	412.6	410.1	410.0	407.6	406.2	402.6
120	366.8	411.1	407.5	406.0	401.7	399.2	395.2
75	373.4	426.9	424.9	422.8	415.7	415.2	411.4
50	368.1	419.0	418.2	415.9	402.8	402.4	406.3
30	368.0	406.7	392.1	399.5	407.0	415.5	401.6

### H.3.1 Axial Discretization

Table H. 5: Maximum external temperature for T2 – T8 for various axial steps.

Number of Axial Steps	T2 (m)	T3 (m)	T4 (m)	T5 (m)	T6 (m)	T7 (m)	T8 (m)
64	399.5	417.6	414.1	410.4	403.5	376.9	367.1
32	403.1	417.1	413.1	407.8	402.9	375.7	367.6
16	405.2	416.9	413.1	409.1	403.6	376.8	366.8
8	403.1	414.6	410.2	406.3	400.2	374.0	365.5

Table H. 6: Maximum external temperature for T9 – T15 for various axial steps.

Number of Axial Steps	T9 (m)	T10 (m)	T11 (m)	T12 (m)	T13 (m)	T14 (m)	T15 (m)
64	369.7	415.4	412.3	411.6	410.5	408.1	405.1
32	369.3	415.7	412.7	411.0	410.1	408.1	406.6
16	368.7	416.0	412.6	411.4	409.9	409.2	405.0
8	366.8	413.5	410.4	409.4	408.0	407.6	403.7

### H.4.1 Simulation Statistics

This section aims to provide insight on simulation times and file sizes of the simulations.

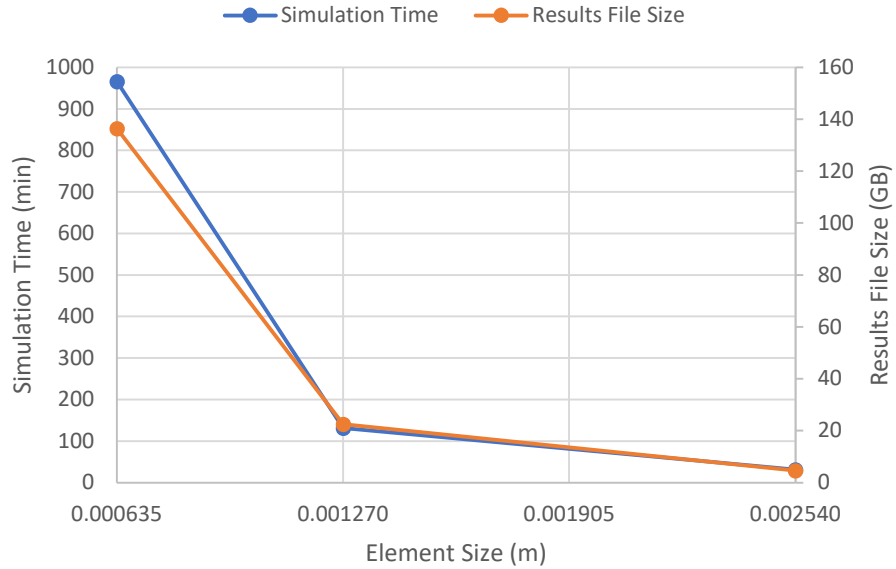


Figure H. 1: Mesh independence simulation statistics.

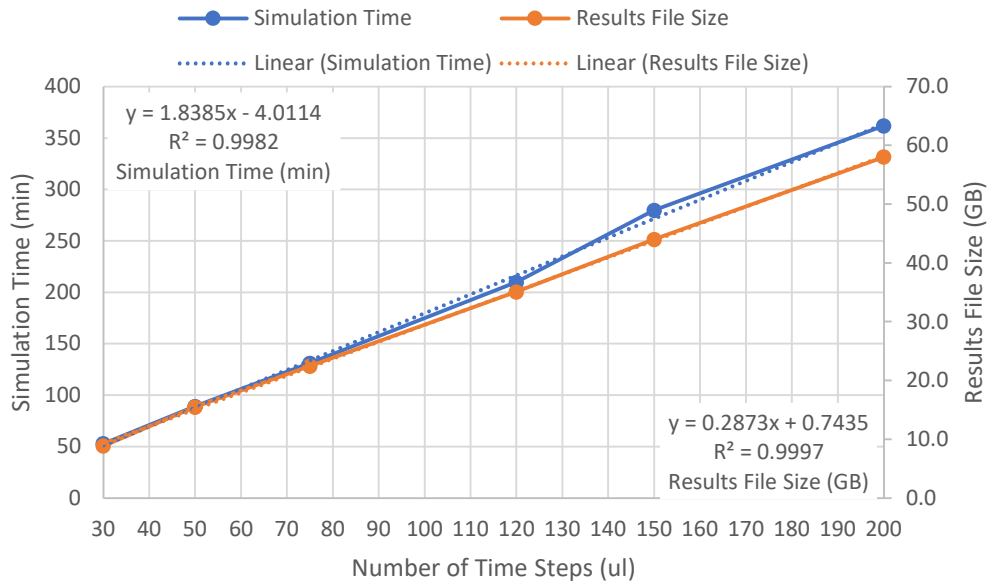


Figure H. 2: Transient discretization simulation statistics.

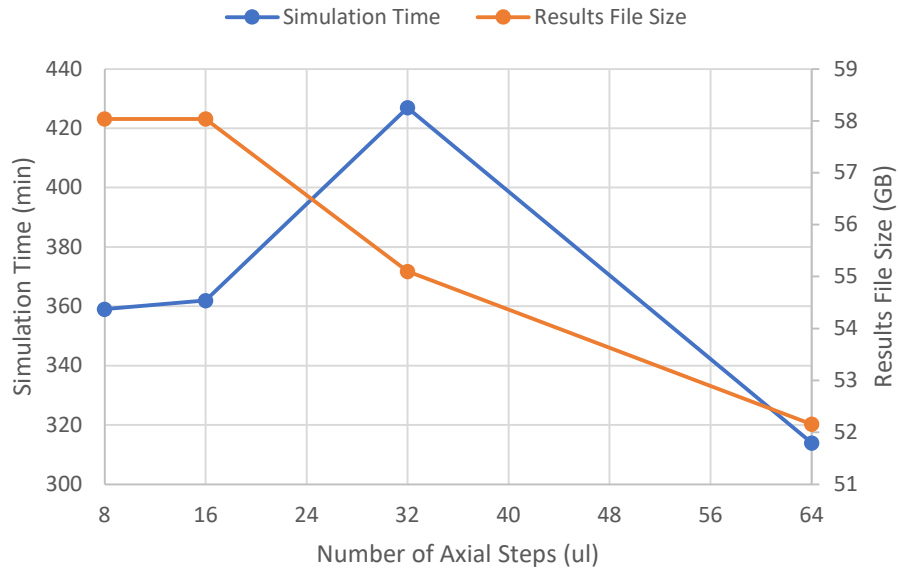


Figure H. 3: Axial discretization simulation statistics.

Table H. 7: Combined statistics for verification simulations.

Element Size (m)	Number of Time Steps	Number of Axial Steps	Number of Nodes	Number of Elements	Simulation Time (min)	Memory Used (GB)	Results File Size (GB)
0.002540	75	16	20177	6416	31.4	0.63	4.66
0.001270	75	16	97196	36632	131	1.052	22.48
0.000635	75	16	626419	266154	966	6.45	136.47
0.001270	30	16	97196	36632	52.98	1.047	8.9
0.001270	50	16	97196	36632	89	1.05	15.47
0.001270	120	16	97196	36632	210	1.056	35.11
0.001270	150	16	97196	36632	280	1.057	44
0.001270	200	16	97196	36632	362	1.062	58.04
0.001270	200	64	83582	33709	314	1.051	52.16
0.001270	200	32	90286	35155	427	1.046	55.1
0.001270	200	8	97196	36632	359	1.054	58.04

# APPENDIX I. 30 AND 60 ROUND VALIDATION

## I.1.1 30 Round Experiment Validation

The maximum percent error was calculated to be 4.9% at T2, .0508 m, with 4.4% error at locations T11 and T13.

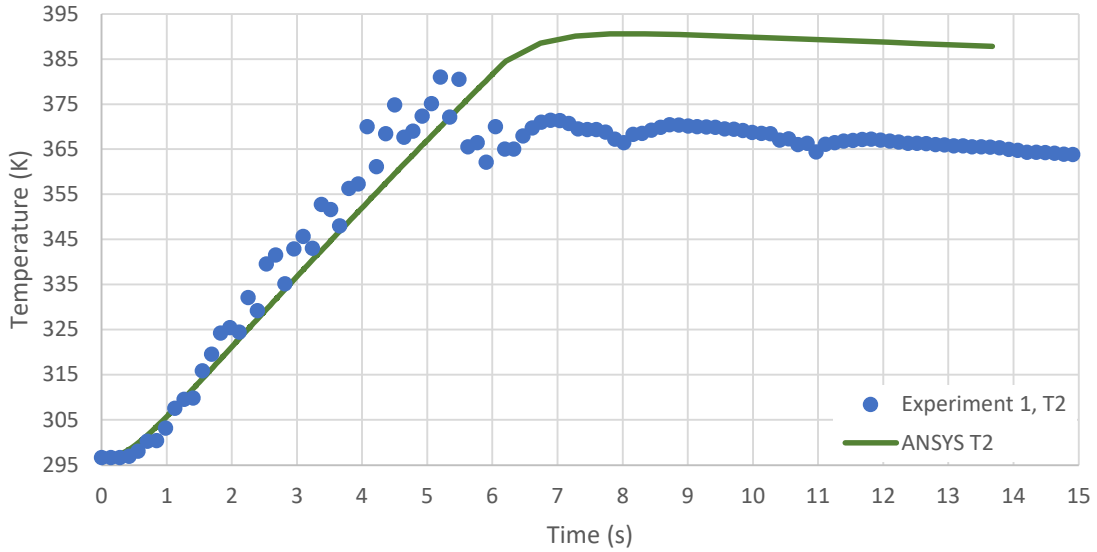


Figure I. 1: Validation of transient temperature response at T2 for experiment 1.

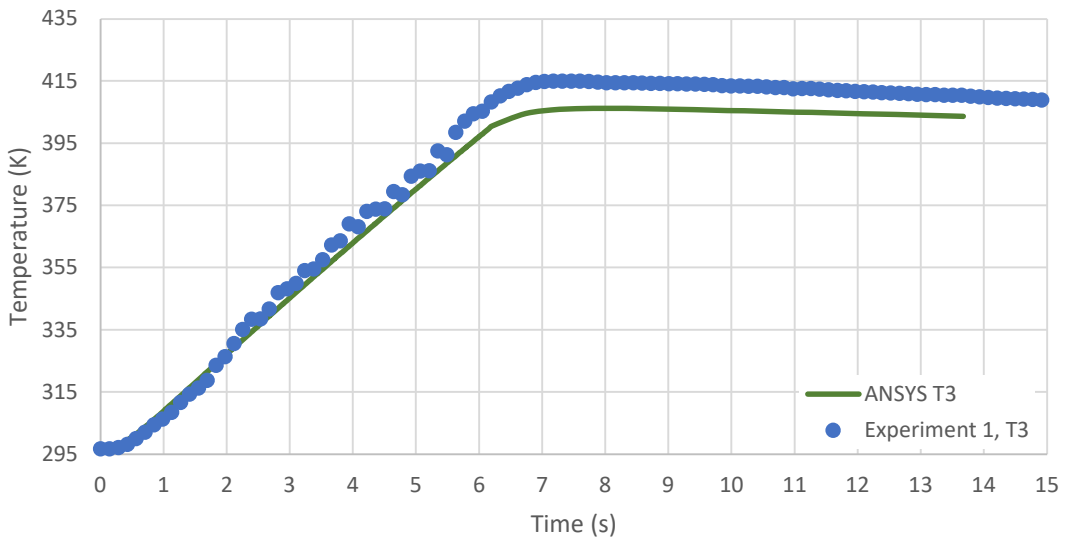


Figure I. 2: Validation of transient temperature response at T3 for experiment 1.

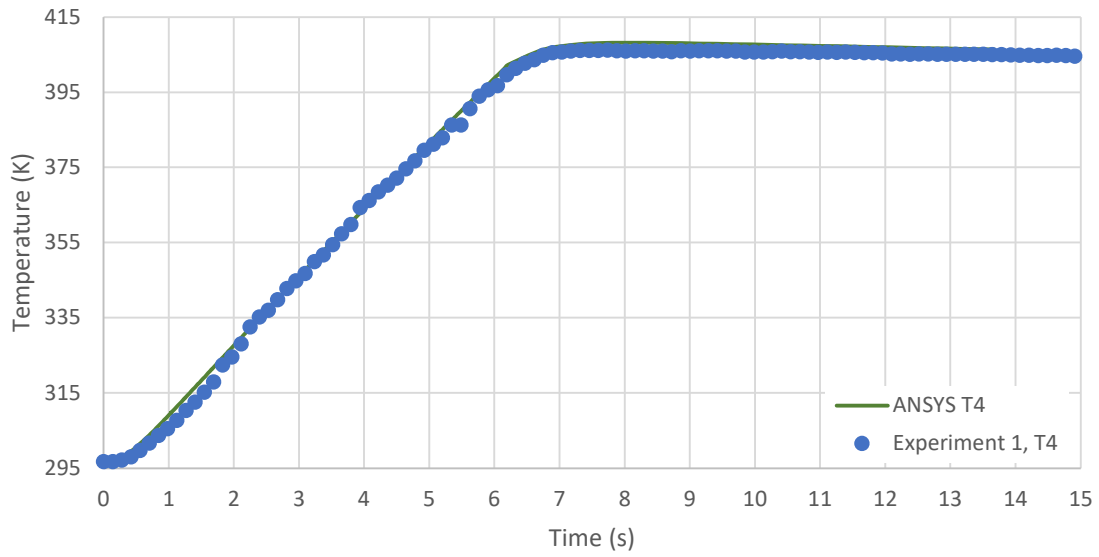


Figure I. 3: Validation of transient temperature response at T4 for experiment 1.

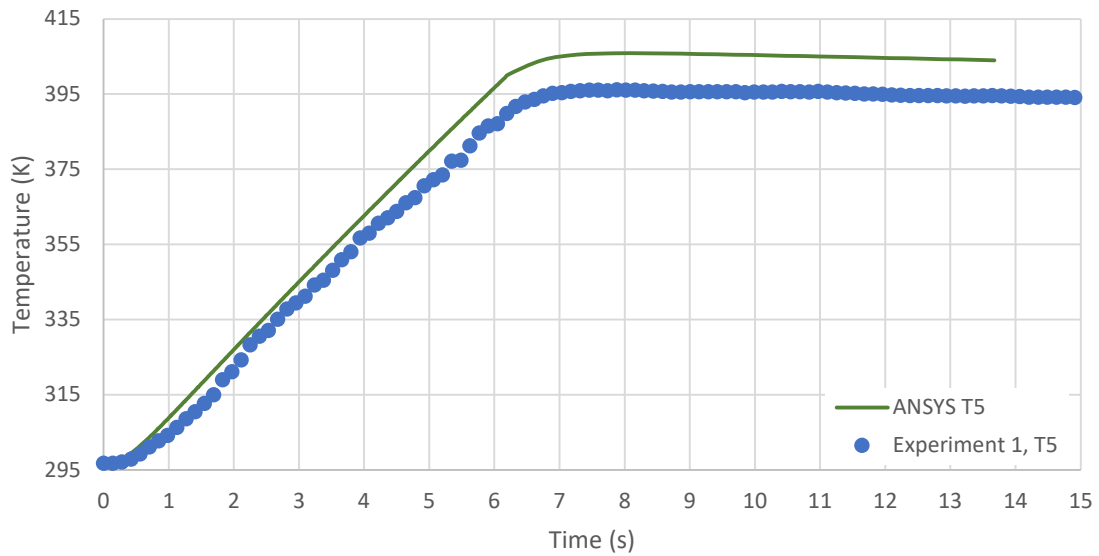


Figure I. 4: Validation of transient temperature response at T5 for experiment 1.

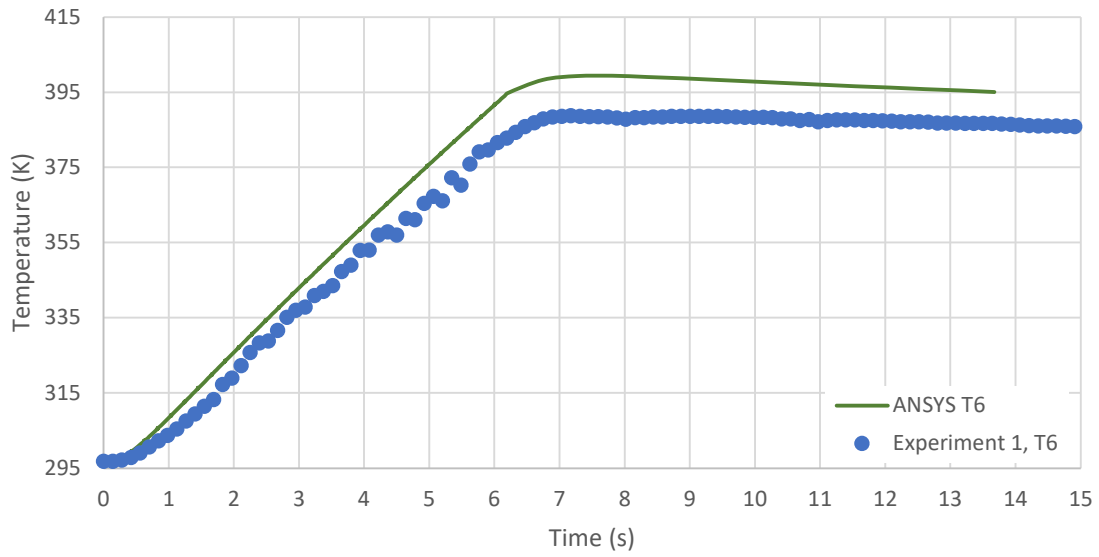


Figure I. 5: Validation of transient temperature response at T6 for experiment 1.

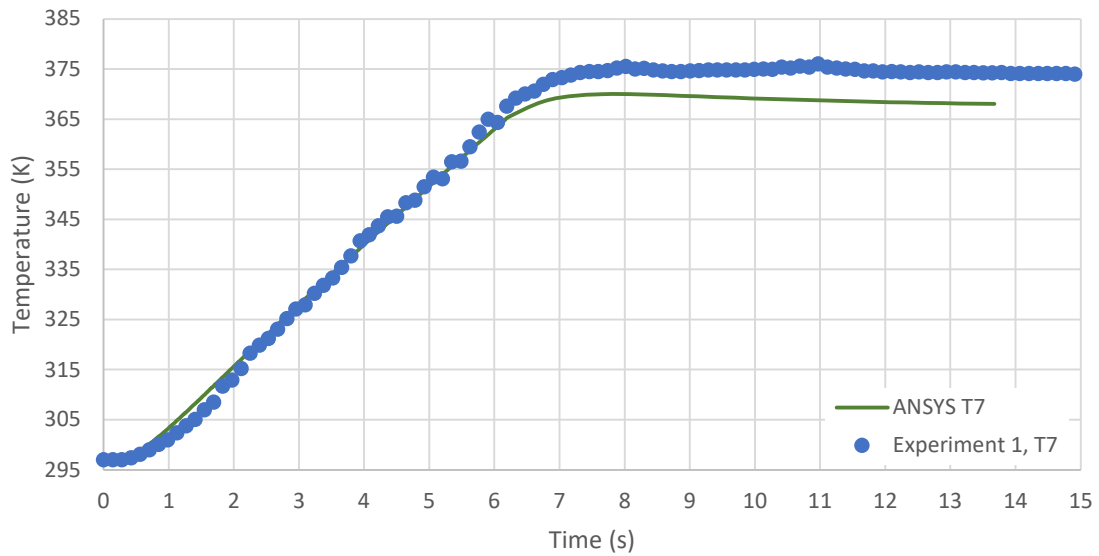


Figure I. 6: Validation of transient temperature response at T7 for experiment 1.

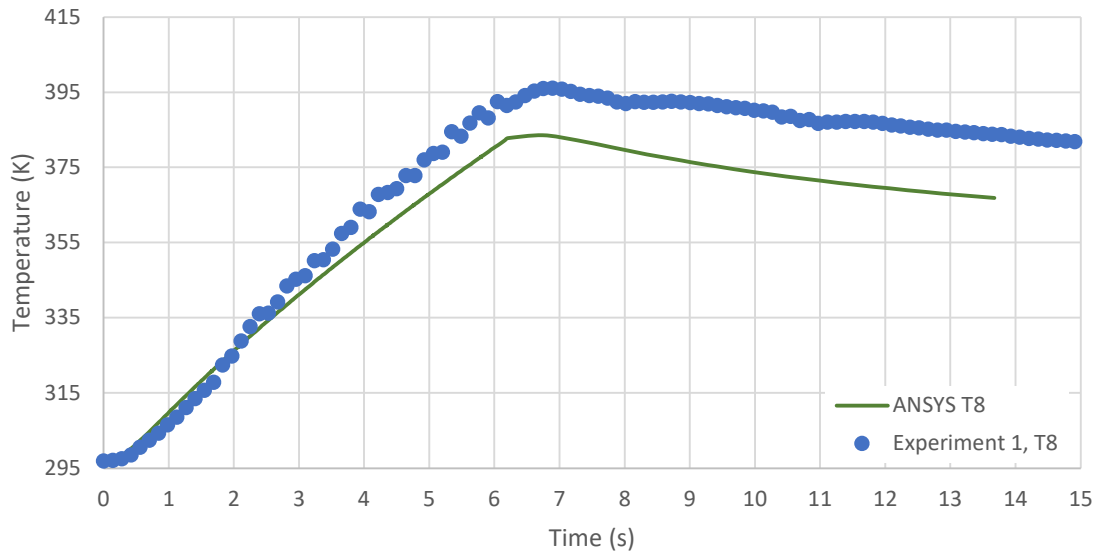


Figure I. 7: Validation of transient temperature response at T8 for experiment 1.

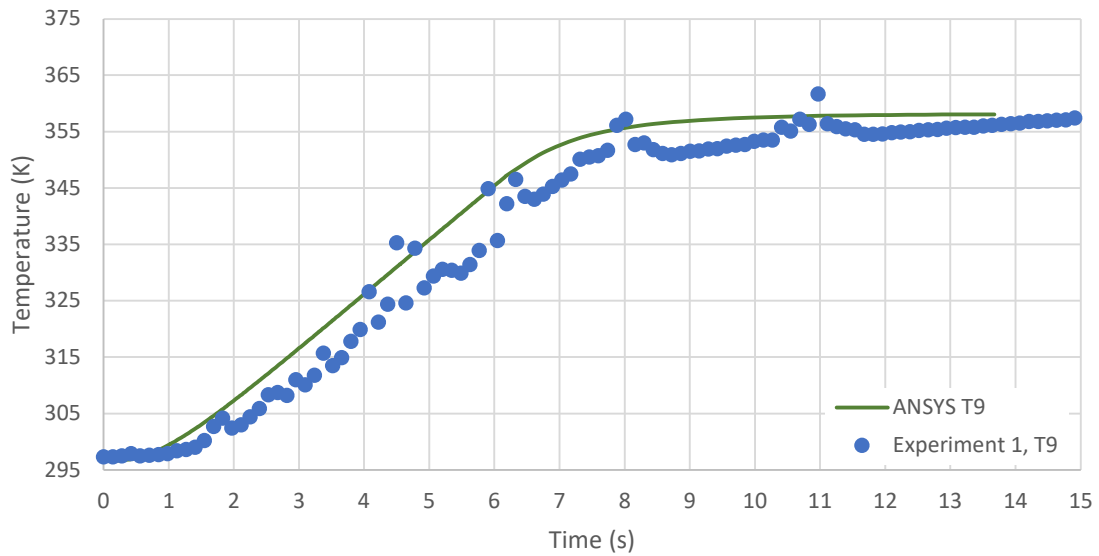


Figure I. 8: Validation of transient temperature response at T9 for experiment 1.

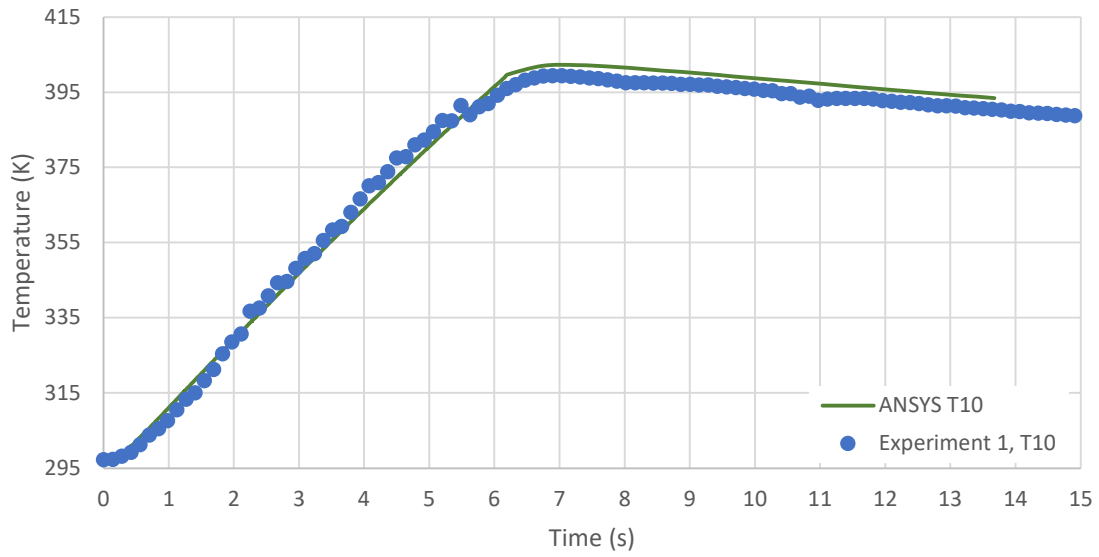


Figure I. 9: Validation of transient temperature response at T10 for experiment 1.

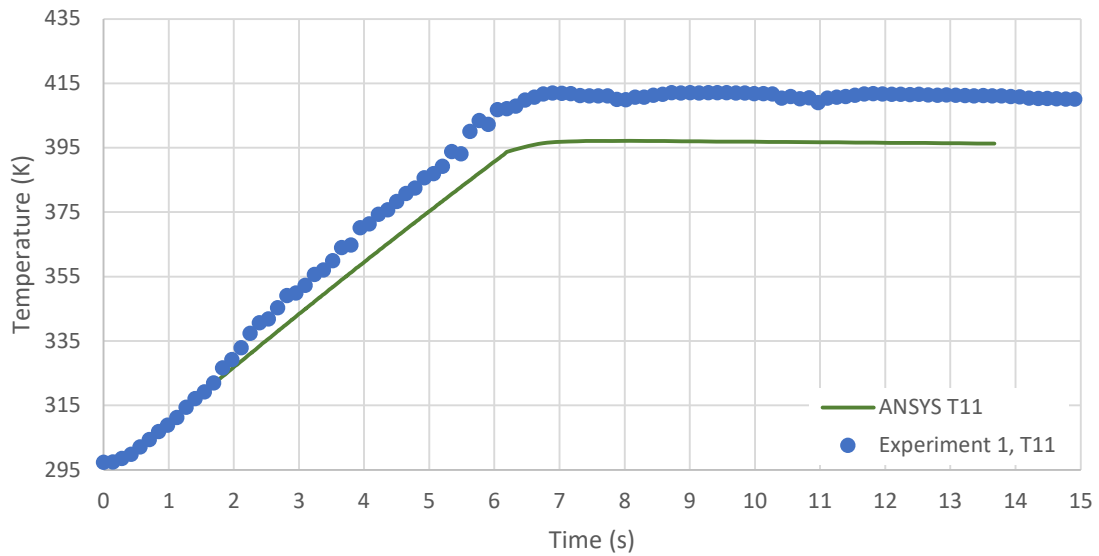


Figure I. 10: Validation of transient temperature response at T11 for experiment 1.

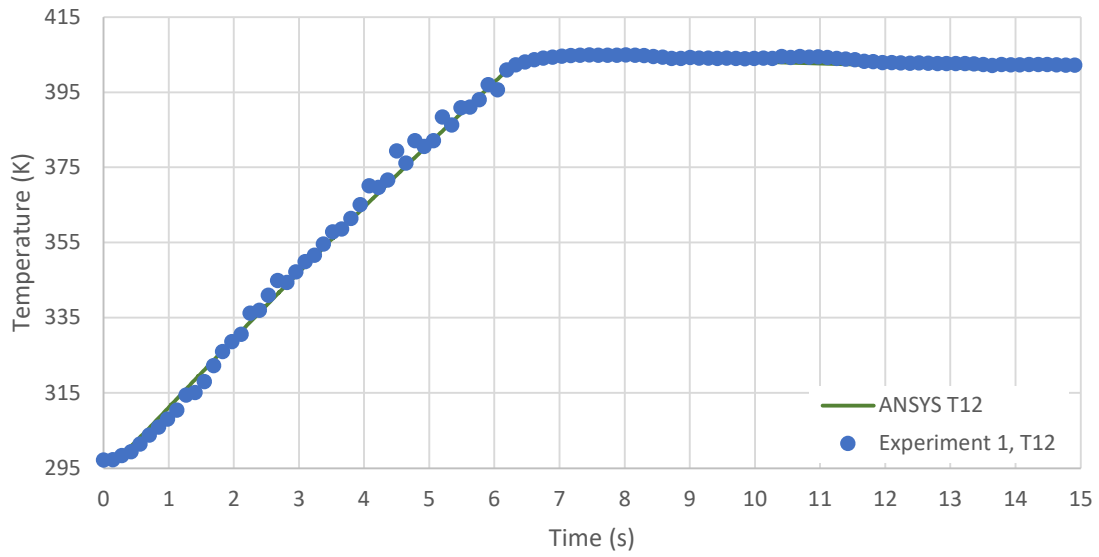


Figure I. 11: Validation of transient temperature response at T12 for experiment 1.

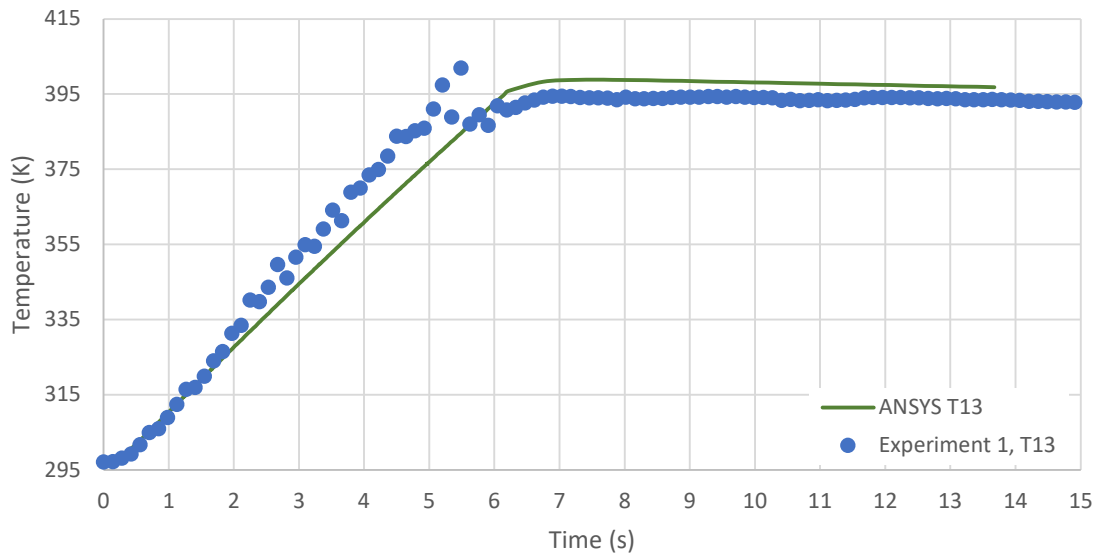


Figure I. 12: Validation of transient temperature response at T13 for experiment 1.

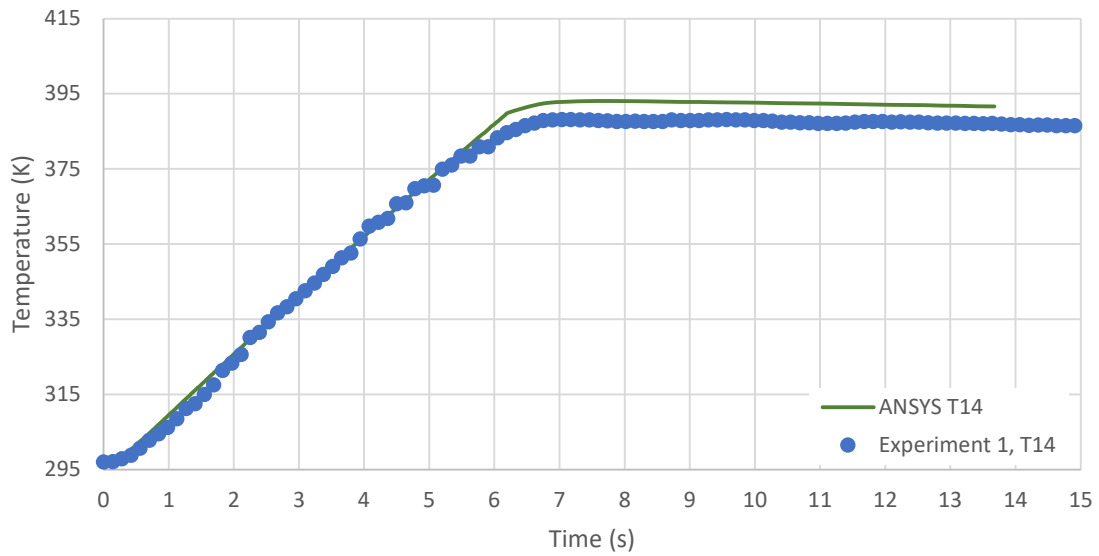


Figure I. 13: Validation of transient temperature response at T4 for experiment 1.

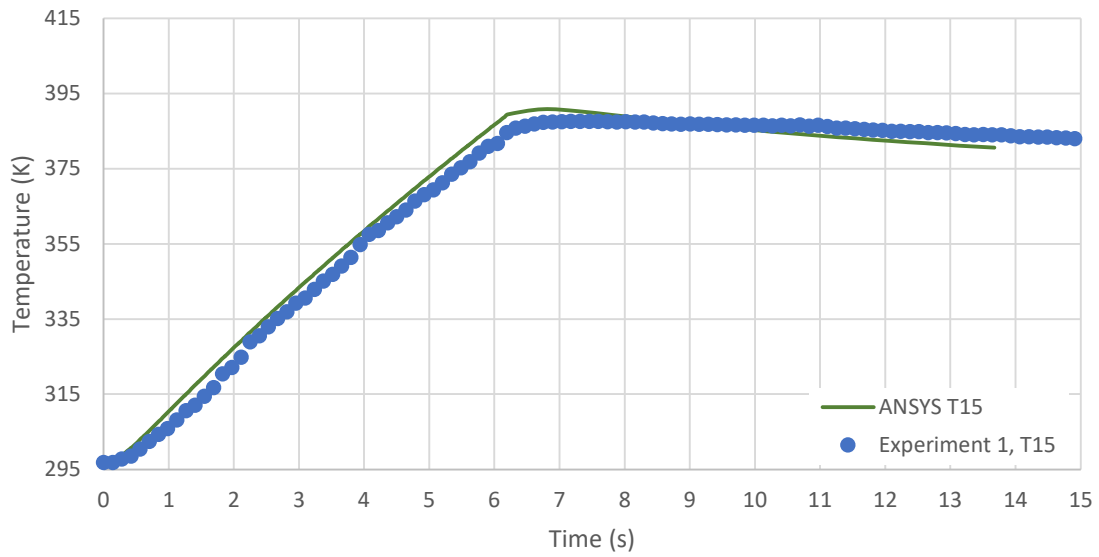


Figure I. 14: Validation of transient temperature response at T15 for experiment 1.

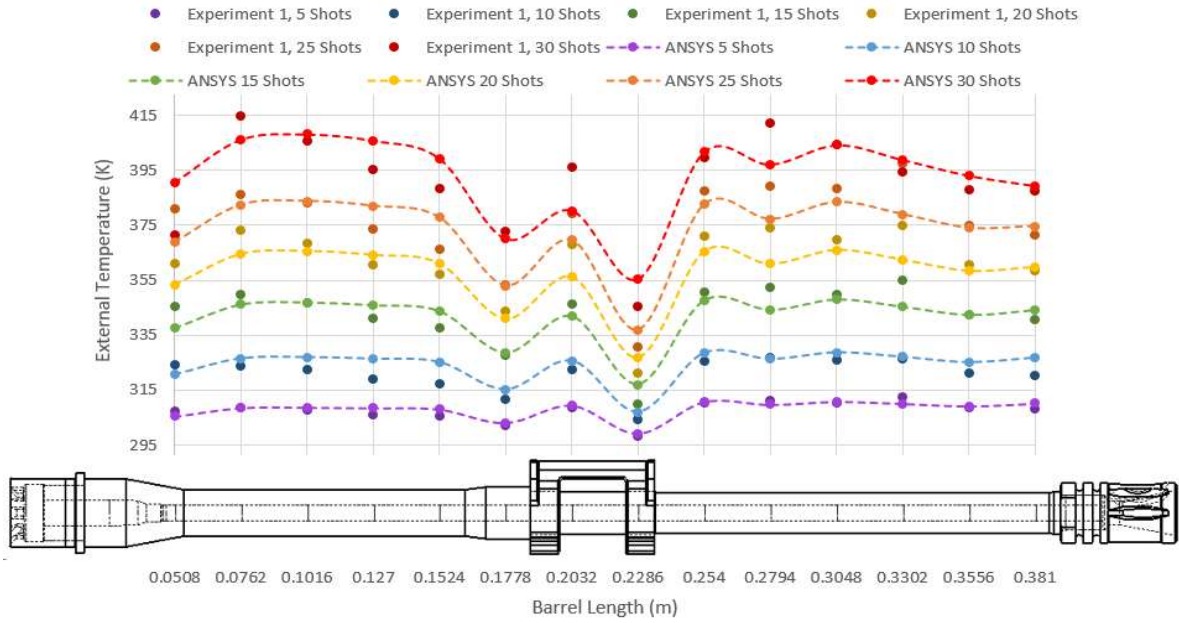


Figure I. 15: Axial temperature distribution after 30 shots at 290 rpm.

Table I. 1: Simulation results for experiment 1 validation.

Number of Shots	T2 (K)	T3 (K)	T4 (K)	T5 (K)	T6 (K)	T7 (K)	T8 (K)
	0.0508 (m)	0.0762 (m)	0.1016 (m)	0.1270 (m)	0.1524 (m)	0.1778 (m)	0.2032 (m)
5	305.5	308.6	308.8	308.6	308.1	303.2	309.5
10	321.5	327.5	328.0	327.4	326.2	315.9	326.6
15	337.6	346.2	347.0	346.0	343.9	328.7	342.0
20	353.3	364.5	365.6	364.2	361.1	341.0	356.2
25	368.8	382.4	383.7	382.0	377.8	353.0	369.6
30	390.6	406.2	408.2	405.9	399.4	370.0	383.6

Number of Shots	T9 (K)	T10 (K)	T11 (K)	T12 (K)	T13 (K)	T14 (K)	T15 (K)
	0.0508 (m)	0.0762 (m)	0.1016 (m)	0.1270 (m)	0.1524 (m)	0.1778 (m)	0.2032 (m)
5	299.4	310.8	309.8	310.9	310.2	309.3	310.2
10	307.5	329.6	327.3	329.8	328.0	326.1	327.7
15	317.1	347.8	344.3	348.1	345.4	342.4	344.2
20	327.0	365.5	361.0	366.0	362.4	358.4	359.8
25	337.0	382.6	377.2	383.4	378.9	374.0	374.7
30	358.1	402.3	397.2	404.3	398.8	393.1	390.9

Table I. 2: Percent error from experiment 1.

	T2 (K)	T3 (K)	T4 (K)	T5 (K)	T6 (K)	T7 (K)	T8 (K)
Number of Shots	.0508 (m)	.0762 (m)	.1016 (m)	.1270 (m)	.1524 (m)	.1778 (m)	.2032 (m)
5	0.7%	0.0%	-0.3%	-0.7%	-0.9%	-0.3%	-0.3%
10	0.9%	-1.2%	-1.7%	-2.6%	-2.7%	-1.3%	-1.2%
15	2.4%	1.1%	0.0%	-1.4%	-1.7%	-0.2%	1.3%
20	4.3%	2.6%	1.3%	-0.6%	-0.9%	1.3%	3.4%
25	0.9%	2.7%	0.7%	-1.3%	-1.5%	1.0%	4.1%
30	-4.9%	2.1%	-0.6%	-2.6%	-2.7%	0.8%	3.3%

	T9 (K)	T10 (K)	T11 (K)	T12 (K)	T13 (K)	T14 (K)	T15 (K)
Number of Shots	.0508 (m)	.0762 (m)	.1016 (m)	.1270 (m)	.1524 (m)	.1778 (m)	.2032 (m)
5	-0.3%	-0.1%	0.5%	-0.1%	0.7%	-0.3%	-0.6%
10	-1.1%	-1.2%	-0.2%	-1.1%	-0.5%	-1.4%	-2.2%
15	-2.2%	0.9%	2.3%	0.5%	2.7%	0.0%	-1.0%
20	-0.8%	2.3%	4.1%	1.6%	4.4%	0.9%	0.2%
25	-2.0%	1.3%	4.4%	0.8%	2.6%	0.5%	-0.3%
30	-3.6%	-0.7%	3.7%	0.0%	-1.1%	-1.3%	-0.9%

### I.2.1 60 Round Experiment Validation

Figures I.16 thru I.31 display the results of transient axial barrel temperature for 60 shots fired at 918 rpm. The maximum percent error was 12.5% at T8, .2023 m.

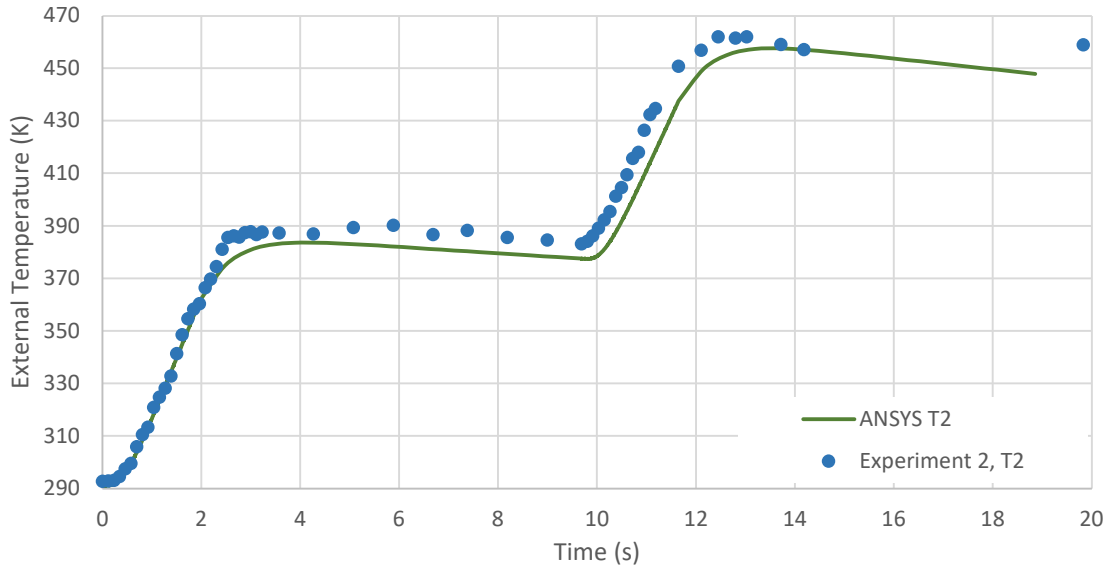


Figure I. 16: Validation of transient temperature response at T2 for experiment 2.

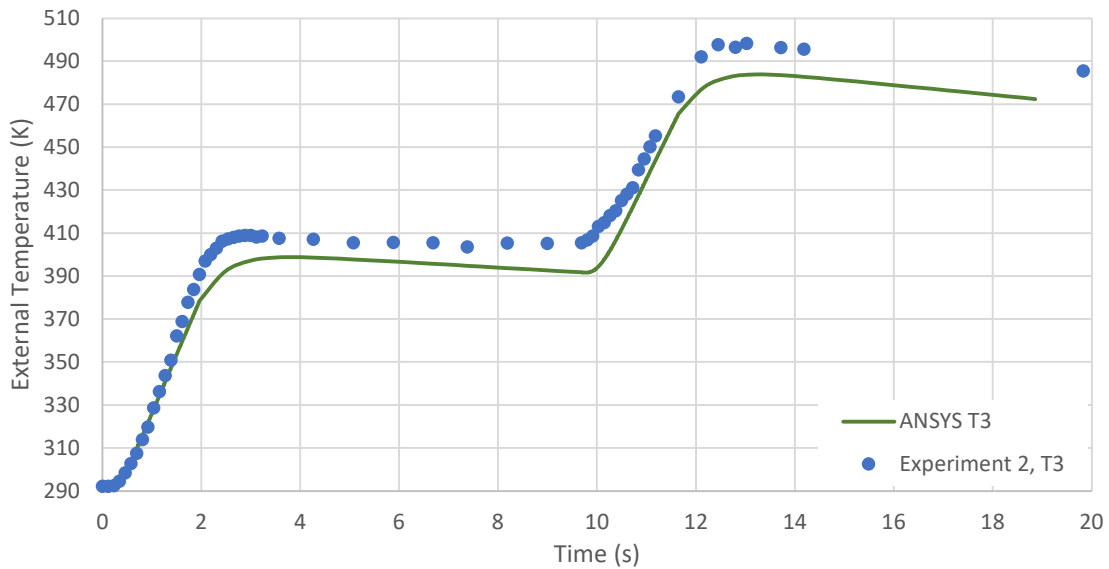


Figure I. 17: Validation of transient temperature response at T3 for experiment 2.

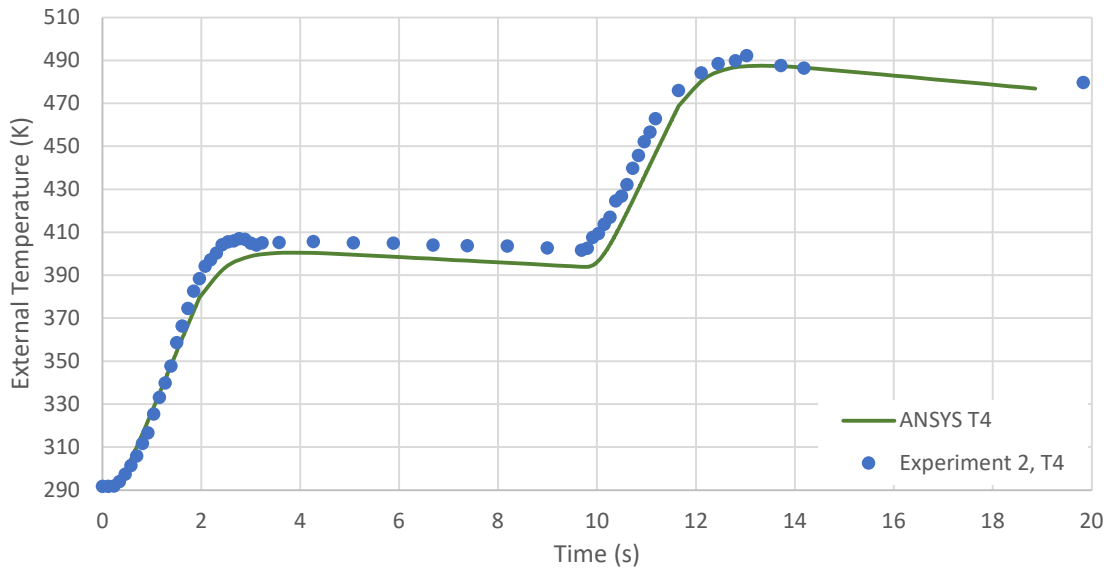


Figure I. 18: Validation of transient temperature response at T4 for experiment 2.

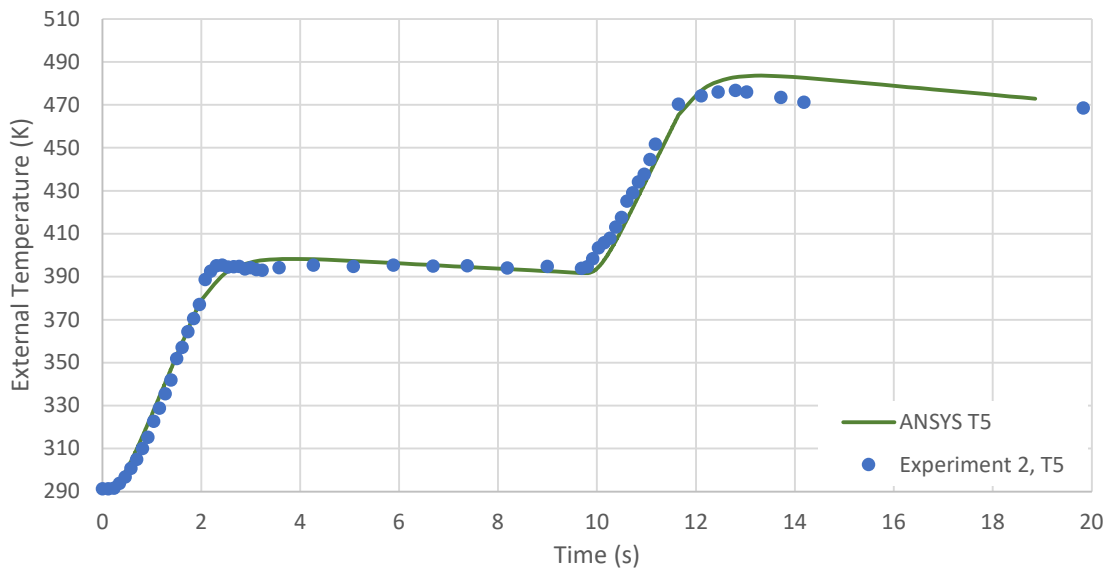


Figure I. 19: Validation of transient temperature response at T5 for experiment 2.

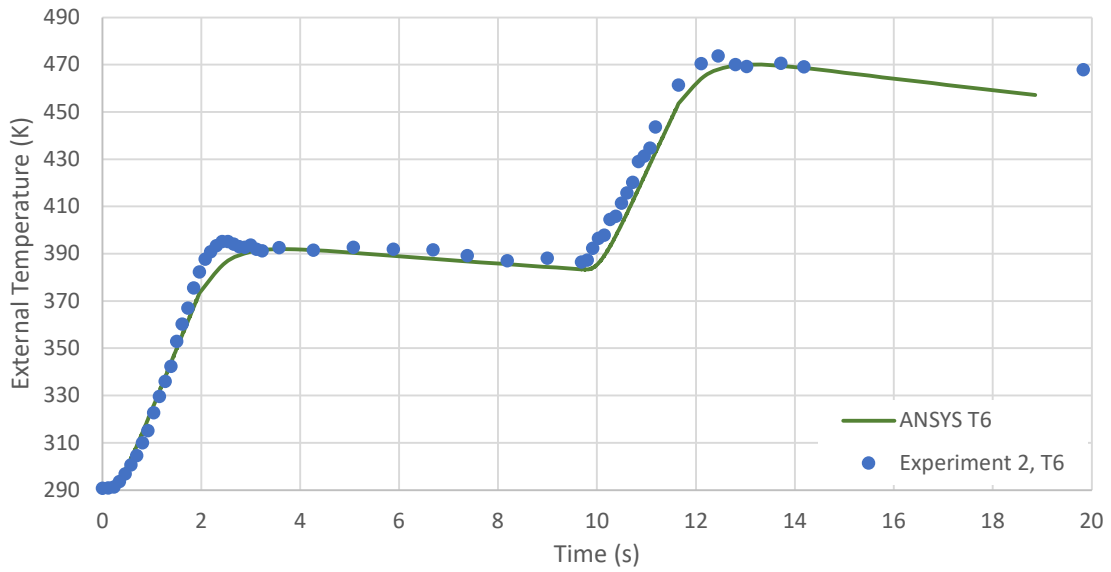


Figure I. 20: Validation of transient temperature response at T6 for experiment 2.

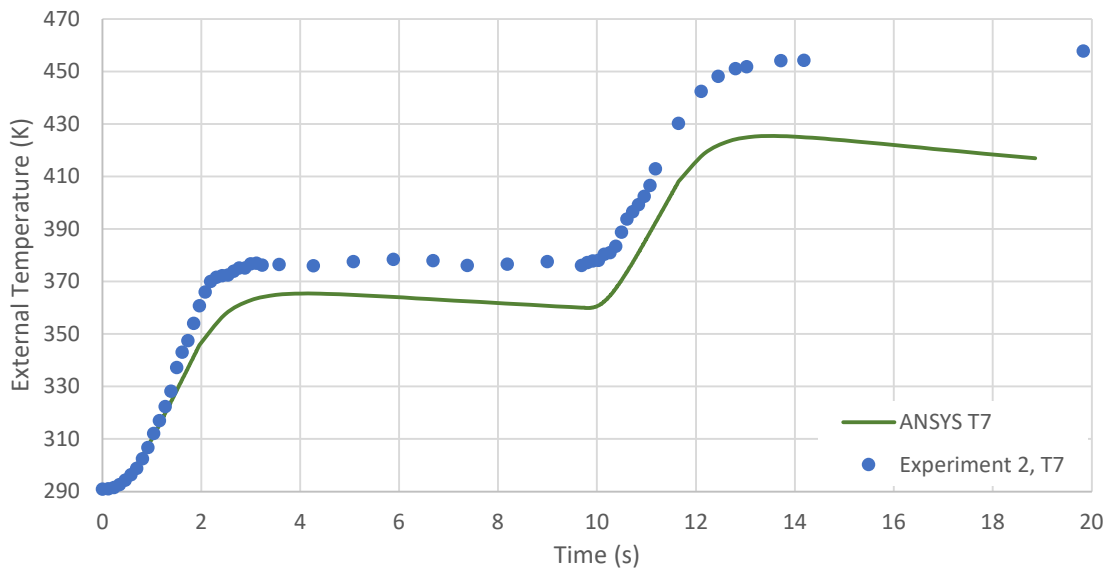


Figure I. 21: Validation of transient temperature response at T7 for experiment 2.

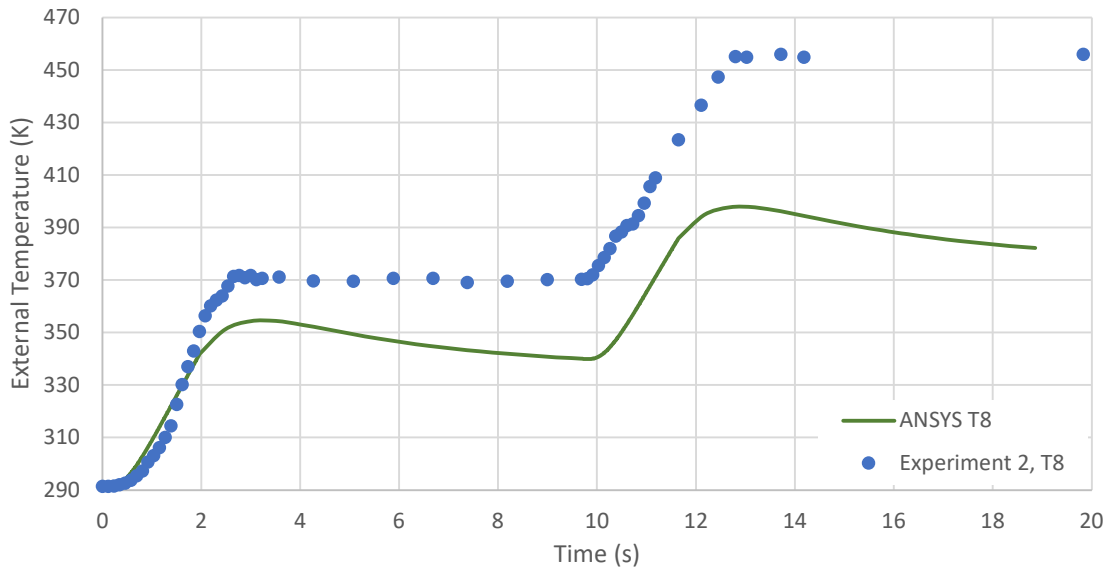


Figure I. 22: Validation of transient temperature response at T8 for experiment 2.

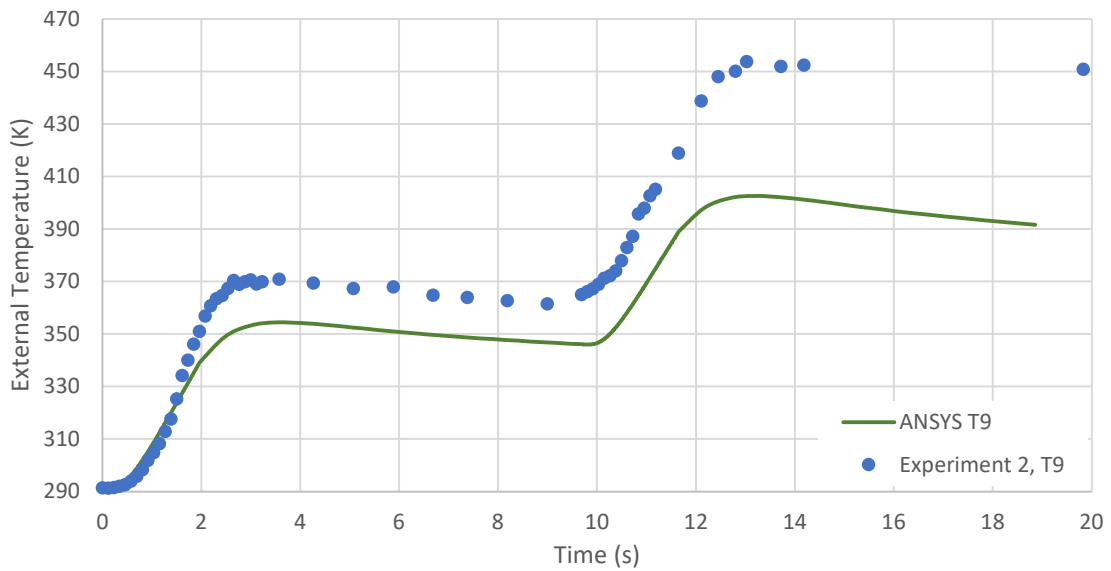


Figure I. 23: Validation of transient temperature response at T9 for experiment 2.

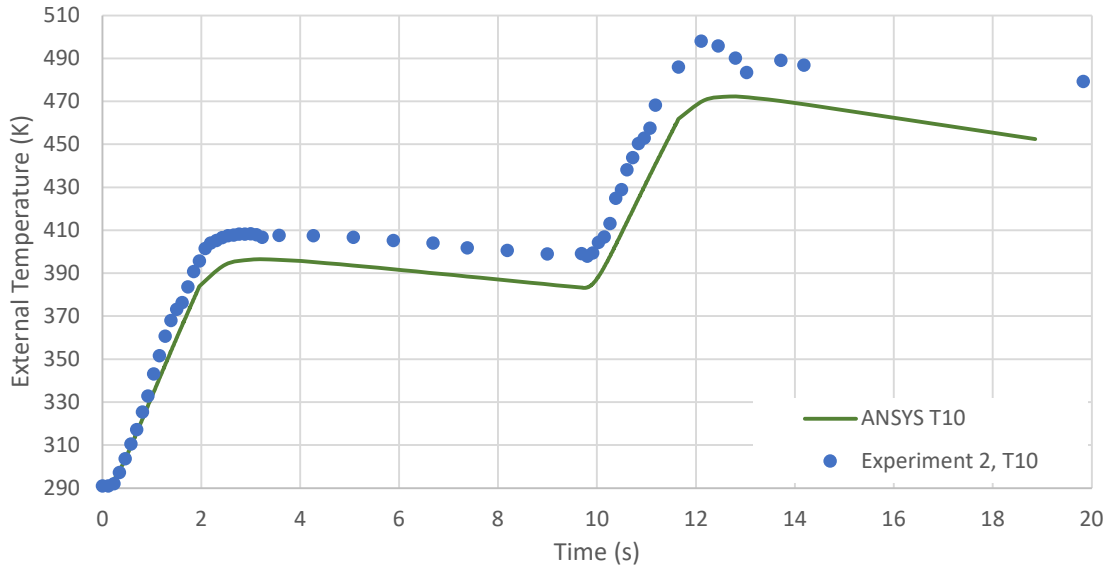


Figure I. 24: Validation of transient temperature response at T10 for experiment 2.

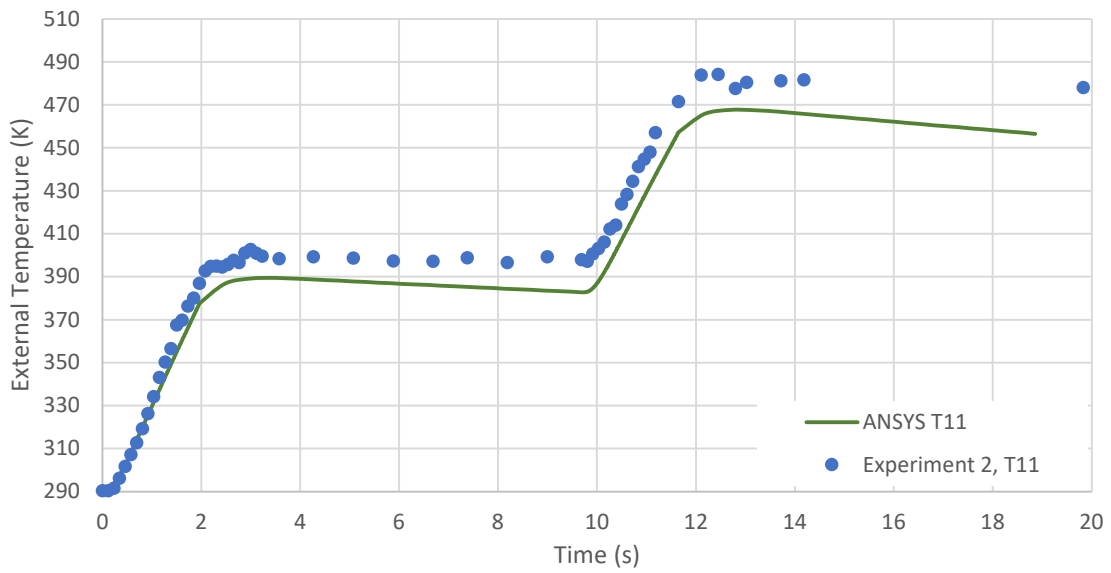


Figure I. 25: Validation of transient temperature response at T11 for experiment 2.

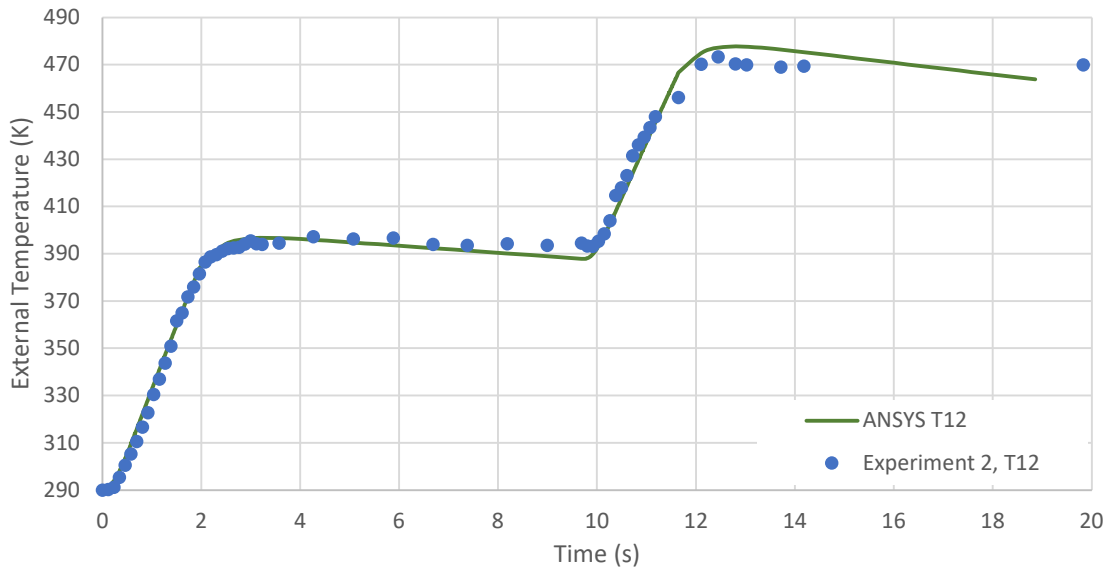


Figure I. 26: Validation of transient temperature response at T12 for experiment 2.

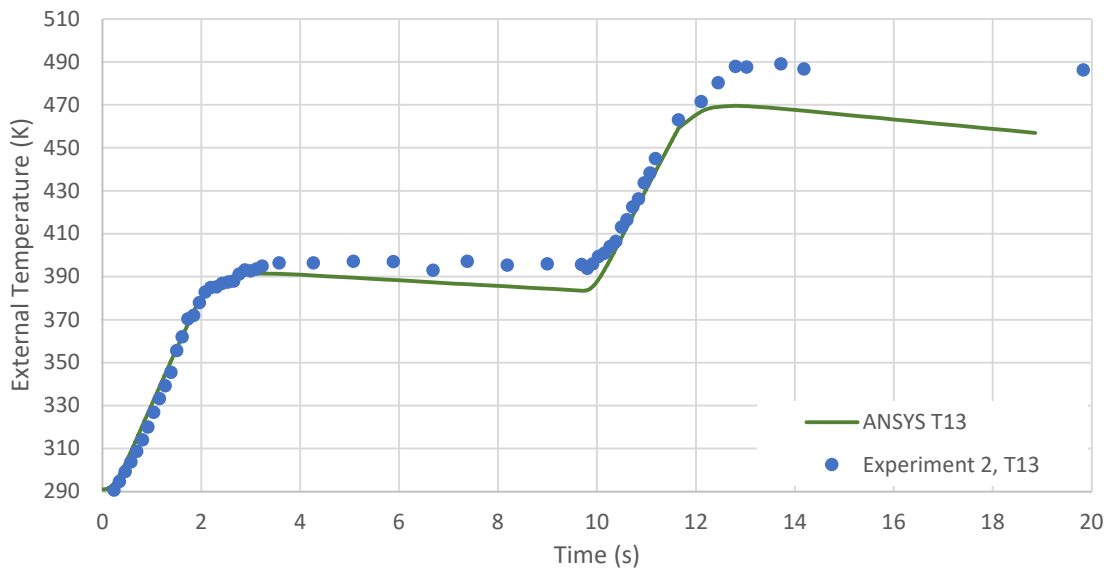


Figure I. 27: Validation of transient temperature response at T13 for experiment 2.

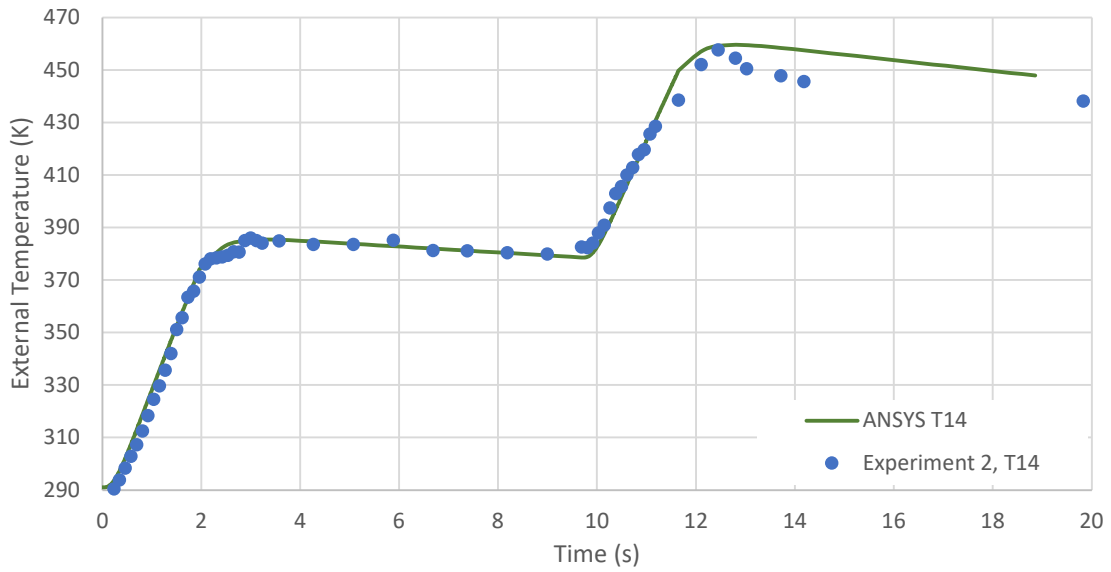


Figure I. 28: Validation of transient temperature response at T14 for experiment 2.

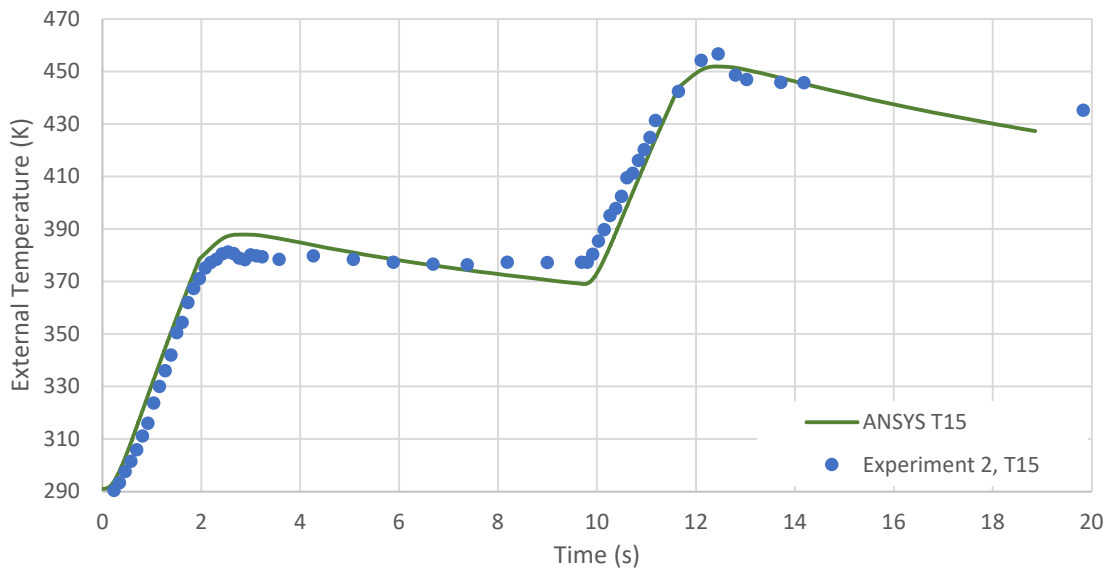


Figure I. 29: Validation of transient temperature response at T15 for experiment 2.

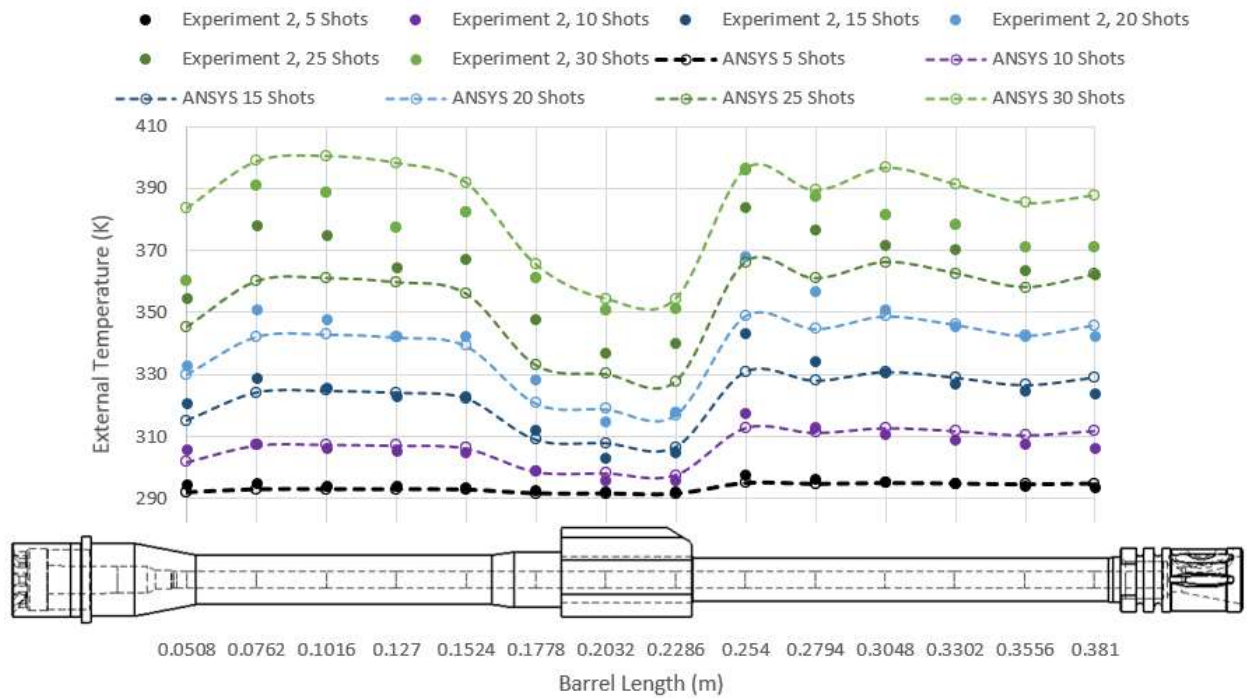


Figure I. 30: Axial temperature distribution after 30 shots at 918 rpm.

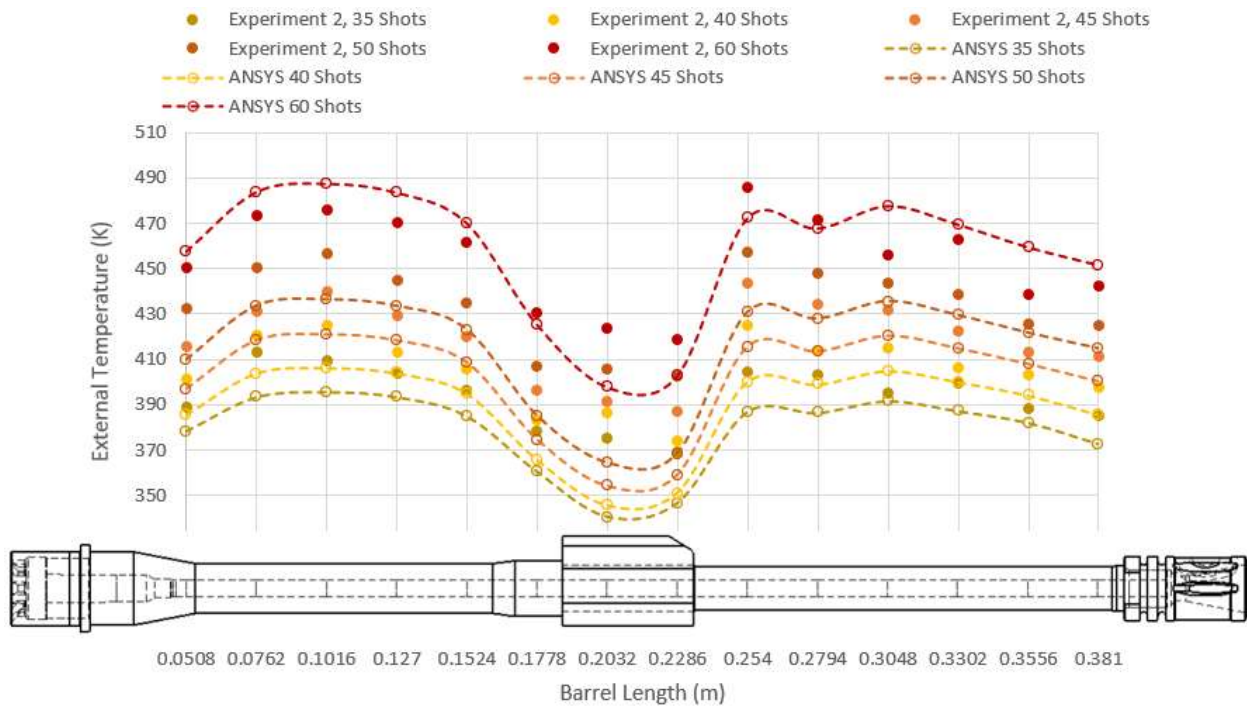


Figure I. 31: Axial temperature distribution after 60 shots at 918 rpm.

Table I. 3: Simulation results for experiment 2 validation.

	T2 (K)	T3 (K)	T4 (K)	T5 (K)	T6 (K)	T7 (K)	T8 (K)
Number of Shots	0.0508 (m)	0.0762 (m)	0.1016 (m)	0.1270 (m)	0.1524 (m)	0.1778 (m)	0.2032 (m)
5	292.7	294.2	294.2	294.2	294.0	292.1	292.0
10	301.8	307.2	307.4	307.1	306.2	298.6	298.1
15	315.2	324.2	324.7	324.1	322.3	308.9	307.9
20	330.1	342.1	342.9	341.9	339.2	320.8	318.9
25	345.3	360.0	361.0	359.7	356.0	333.0	330.1
30	383.7	398.8	400.5	398.3	392.0	365.5	354.4
35	378.3	393.5	395.8	393.6	385.1	360.5	340.4
40	385.5	403.8	406.3	403.9	394.9	365.7	345.5
45	396.9	418.2	420.8	418.2	408.6	374.7	354.2
50	409.7	433.5	436.3	433.5	423.1	385.2	364.3
55	423.0	449.0	451.9	448.8	437.8	396.1	374.7
60	457.6	483.8	487.5	483.6	470.1	425.4	397.8

	T9 (K)	T10 (K)	T11 (K)	T12 (K)	T13 (K)	T14 (K)	T15 (K)
Number of Shots	0.0508 (m)	0.0762 (m)	0.1016 (m)	0.1270 (m)	0.1524 (m)	0.1778 (m)	0.2032 (m)
5	291.9	296.8	296.4	296.8	296.6	296.2	296.6
10	297.6	312.9	311.3	312.9	311.9	310.5	312.0
15	306.6	330.9	328.0	330.8	329.0	326.5	329.0
20	317.0	348.7	344.7	348.7	346.0	342.5	345.9
25	327.8	366.2	360.9	366.2	362.6	358.1	362.2
30	354.5	396.4	389.5	396.7	391.4	385.4	387.9
35	346.5	387.0	386.5	391.7	387.3	382.1	372.8
40	351.1	400.1	398.9	404.9	400.0	394.0	385.5
45	359.0	415.4	413.3	420.2	414.6	407.8	400.2
50	368.4	430.7	427.8	435.6	429.4	421.6	414.7
55	378.2	445.8	442.1	450.6	443.8	435.2	428.9
60	402.7	472.3	467.7	477.7	469.5	459.5	451.7

Table I. 4: Percent error from experiment 2.

Number of Shots	T2 (K)	T3 (K)	T4 (K)	T5 (K)	T6 (K)	T7 (K)	T8 (K)
	0.0508 (m)	0.0762 (m)	0.1016 (m)	0.1270 (m)	0.1524 (m)	0.1778 (m)	0.2032 (m)
5	0.6%	0.2%	0.0%	-0.1%	-0.1%	0.2%	0.0%
10	1.3%	0.1%	-0.5%	-0.7%	-0.5%	0.1%	-0.9%
15	1.8%	1.4%	0.2%	-0.4%	0.2%	1.1%	-1.5%
20	0.8%	2.6%	1.4%	0.0%	1.0%	2.4%	-1.3%
25	2.7%	5.0%	3.8%	1.4%	3.1%	4.4%	2.1%
30	1.1%	2.6%	1.1%	-1.0%	0.5%	3.1%	4.9%
35	2.9%	5.0%	3.5%	2.5%	3.0%	4.9%	10.3%
40	4.1%	4.1%	4.6%	2.3%	2.8%	4.9%	11.9%
45	4.7%	3.1%	4.5%	2.6%	2.9%	5.9%	10.5%
50	5.5%	3.9%	4.7%	2.6%	2.8%	5.6%	11.4%
60	1.0%	2.9%	0.2%	-1.5%	0.8%	5.4%	12.5%

Number of Shots	T9 (K)	T10 (K)	T11 (K)	T12 (K)	T13 (K)	T14 (K)	T15 (K)
	0.0508 (m)	0.0762 (m)	0.1016 (m)	0.1270 (m)	0.1524 (m)	0.1778 (m)	0.2032 (m)
5	0.1%	0.2%	0.0%	-0.4%	-0.6%	-0.7%	-1.0%
10	-0.6%	1.4%	0.5%	-0.7%	-1.0%	-1.0%	-1.9%
15	-0.6%	3.8%	1.9%	-0.1%	-0.6%	-0.6%	-1.6%
20	0.2%	5.6%	3.5%	0.7%	-0.1%	-0.1%	-1.1%
25	3.8%	4.8%	4.3%	1.5%	2.2%	1.5%	0.0%
30	4.6%	3.1%	3.4%	-0.3%	0.4%	0.2%	-1.9%
35	6.5%	4.5%	4.3%	0.9%	3.1%	1.6%	3.4%
40	6.6%	6.2%	3.8%	2.4%	1.7%	2.3%	3.2%
45	7.9%	6.9%	5.1%	2.7%	1.9%	1.3%	2.8%
50	9.3%	6.2%	4.8%	1.8%	2.1%	1.0%	2.5%
60	11.3%	5.0%	3.5%	-0.9%	2.3%	-0.4%	1.1%

### I.3.1 90 Round Experiment Validation

Table I. 5: Simulation results for experiment 4 validation.

Number of Shots	T2 (K)	T3 (K)	T4 (K)	T5 (K)	T6 (K)	T7 (K)	T8 (K)
	0.0508 (m)	0.0762 (m)	0.1016 (m)	0.1270 (m)	0.1524 (m)	0.1778 (m)	0.2032 (m)
5	288.7	289.9	290.3	290.2	290.1	288.2	288.2
10	296.6	301.3	303.4	303.1	302.2	294.6	294.2
15	308.7	316.4	320.8	320.2	318.3	304.9	304.0
20	322.1	332.5	339.2	338.2	335.5	316.8	315.1
25	335.9	348.6	357.6	356.3	352.6	329.3	326.7
30	349.8	364.4	375.8	374.1	369.5	341.8	338.1
35	371.8	386.9	399.8	398.4	389.0	362.7	342.6
40	379.5	397.9	410.5	409.0	399.1	368.1	347.9
45	391.3	412.8	425.3	423.5	413.0	377.3	356.7
50	404.6	428.7	441.1	439.1	427.8	388.0	367.0
55	418.4	444.7	457.0	454.8	442.8	399.1	377.7
60	432.2	460.5	472.7	470.2	457.5	410.4	388.3
65	452.6	480.9	492.4	489.9	471.8	427.9	394.1
70	458.6	489.6	501.0	498.3	480.0	432.4	398.9
75	468.7	502.3	513.6	510.7	491.9	440.4	407.0
80	480.3	516.2	527.5	524.4	505.0	449.9	416.5
85	492.5	530.5	541.7	538.4	518.4	460.0	426.4
90	505.5	545.3	556.6	553.0	532.4	470.8	436.8

Table I. 6: Simulation results for experiment 4 validation.

Number of Shots	T9 (K) 0.0508 (m)	T10 (K) 0.0762 (m)	T11 (K) 0.1016 (m)	T12 (K) 0.1270 (m)	T13 (K) 0.1524 (m)	T14 (K) 0.1778 (m)	T15 (K) 0.2032 (m)
5	288.1	292.9	292.5	292.9	292.7	292.3	292.7
10	293.6	309.0	307.4	309.0	308.0	306.6	308.1
15	302.7	327.2	324.3	327.1	325.3	322.9	325.4
20	313.3	345.4	341.3	345.3	342.6	339.1	342.5
25	324.3	363.2	357.9	363.2	359.6	355.0	359.2
30	335.4	380.6	374.2	380.6	376.2	370.6	375.3
35	350.3	392.2	392.3	397.9	393.1	387.5	376.4
40	355.2	405.6	405.0	411.4	406.1	399.7	389.6
45	363.4	421.2	419.7	427.1	421.0	413.7	404.6
50	373.2	436.8	434.6	442.8	436.0	427.9	419.5
55	383.4	452.3	449.2	458.3	450.8	441.8	434.1
60	393.7	467.4	463.5	473.4	465.3	455.5	448.1
65	406.2	470.5	477.6	485.0	477.8	467.6	443.3
70	410.4	481.8	488.3	496.3	488.7	477.9	454.6
75	417.8	495.4	501.1	509.9	501.6	490.1	467.9
80	426.6	509.3	514.2	523.7	514.9	502.5	481.3
85	436.0	523.1	527.1	537.5	528.0	514.8	494.3
90	445.9	537.4	540.5	551.6	541.5	527.6	507.6

Table I. 7: Percent error from experiment 4.

Number of Shots	T2 (K)	T3 (K)	T4 (K)	T5 (K)	T6 (K)	T7 (K)	T8 (K)
	0.0508 (m)	0.0762 (m)	0.1016 (m)	0.1270 (m)	0.1524 (m)	0.1778 (m)	0.2032 (m)
5	0.9%	0.8%	0.5%	0.2%	0.3%	0.2%	0.1%
10	2.3%	2.1%	0.9%	0.4%	0.6%	0.9%	0.6%
15	3.2%	2.9%	0.7%	-0.1%	0.7%	1.6%	1.6%
20	1.5%	3.9%	1.2%	0.3%	1.0%	2.1%	0.1%
25	4.1%	3.9%	0.9%	-0.2%	0.2%	3.7%	0.3%
30	2.6%	2.2%	-0.9%	-1.1%	-0.8%	1.1%	0.4%
35	2.3%	1.8%	-2.6%	-3.1%	-2.0%	3.1%	7.6%
40	1.7%	2.0%	-2.5%	-4.8%	-2.2%	3.4%	7.9%
45	1.4%	1.9%	-1.6%	-4.1%	-3.3%	3.4%	6.4%
50	2.7%	1.4%	-1.1%	-3.2%	-1.8%	3.6%	5.9%
55	3.7%	1.3%	-0.9%	-3.2%	-1.5%	3.4%	6.4%
60	4.1%	0.1%	-2.6%	-4.1%	-2.3%	2.6%	6.7%
65	0.9%	0.0%	-3.5%	-7.0%	-2.8%	4.8%	12.3%
70	1.1%	-0.4%	-3.8%	-7.4%	-3.5%	4.6%	12.3%
75	0.0%	-1.6%	-3.9%	-7.5%	-3.2%	5.6%	11.3%
80	1.7%	-0.9%	-3.4%	-8.1%	-4.6%	3.8%	9.4%
85	1.9%	-1.2%	-4.6%	-8.0%	-4.1%	3.8%	9.6%
90	0.9%	-1.6%	-4.1%	-9.3%	-6.1%	3.0%	9.3%

Table I. 8: Percent error from experiment 4.

	T9 (K)	T10 (K)	T11 (K)	T12 (K)	T13 (K)	T14 (K)	T15 (K)
Number of Shots	0.0508 (m)	0.0762 (m)	0.1016 (m)	0.1270 (m)	0.1524 (m)	0.1778 (m)	0.2032 (m)
5	0.0%	0.8%	0.1%	-0.4%	-0.1%	-0.3%	-0.2%
10	0.9%	1.9%	0.6%	-0.9%	0.1%	-0.7%	-0.7%
15	1.8%	3.0%	0.5%	-1.8%	-0.5%	-1.1%	-1.3%
20	1.4%	4.0%	1.1%	-2.2%	0.0%	-1.7%	-1.6%
25	3.6%	6.2%	2.0%	-2.1%	0.8%	-1.9%	-1.8%
30	1.7%	3.9%	1.0%	-4.2%	-1.5%	-4.0%	-3.9%
35	4.7%	2.6%	-0.7%	-4.9%	-0.1%	-4.0%	-1.7%
40	4.9%	3.2%	-1.1%	-4.9%	-2.7%	-4.9%	-1.8%
45	4.8%	3.2%	-2.5%	-5.6%	-2.6%	-5.0%	-1.7%
50	5.4%	3.1%	-2.8%	-6.5%	-2.7%	-5.0%	-2.2%
55	6.0%	4.4%	-1.1%	-5.5%	-1.7%	-5.2%	-2.1%
60	5.5%	3.4%	-1.4%	-6.7%	-2.0%	-6.5%	-3.2%
65	8.1%	2.7%	-1.0%	-7.5%	-2.5%	-7.1%	-1.2%
70	8.1%	2.3%	-2.0%	-8.4%	-3.6%	-7.1%	-1.3%
75	7.6%	2.7%	-2.5%	-8.4%	-4.0%	-7.5%	-1.7%
80	8.1%	1.6%	-3.2%	-9.1%	-5.2%	-6.6%	-1.7%
85	8.0%	2.8%	-2.3%	-9.3%	-4.1%	-7.6%	-1.9%
90	6.7%	1.7%	-4.3%	-10.2%	-3.6%	-8.1%	-2.8%

## APPENDIX J. EFFECTS OF COOLING TIME BETWEEN BURSTS RESULTS

Table J. 1: External temperatures for 3.052 seconds between bursts.

Time Between Bursts: 3.052 seconds				
Cartridges Fired	T1	T2	T3	T4
	0.0508 (m)	0.1016 (m)	0.1397 (m)	0.2794 (m)
30	406.2	435.6	439.8	394.9
60	490.5	542.5	544.0	468.5
90	566.6	635.2	631.2	530.2
120	640.2	723.4	713.3	590.0
150	707.0	804.8	788.6	644.7
180	768.5	878.9	857.6	694.2
210	825.3	938.3	917.3	739.9
240	876.9	981.4	961.2	780.7
270	923.7	1015.3	997.1	821.8

Table J. 2: External temperatures and relative temperature change.

Time Between Bursts: 6 seconds								
Cartridges Fired	T1	T1	T2	T2	T3	T3	T4	T4
	0.0508 (m)	Relative Change	0.1016 (m)	Relative Change	0.1397 (m)	Relative Change	0.2794 (m)	Relative Change
30	409.9	0.9%	437.2	0.4%	440.4	0.1%	393.6	-0.3%
60	495.5	1.0%	545.5	0.5%	543.9	0.0%	467.6	-0.2%
90	565.8	-0.1%	632.4	-0.4%	622.9	-1.3%	525.0	-1.0%
120	636.9	-0.5%	718.4	-0.7%	701.0	-1.7%	582.6	-1.3%
150	701.0	-0.9%	797.2	-0.9%	772.5	-2.0%	635.3	-1.5%
180	759.6	-1.2%	869.0	-1.1%	837.9	-2.3%	682.8	-1.6%
210	813.6	-1.4%	928.1	-1.1%	897.0	-2.2%	726.5	-1.8%
240	862.3	-1.7%	971.3	-1.0%	941.8	-2.0%	765.1	-2.0%
270	908.8	-1.6%	1005.7	-0.9%	978.9	-1.8%	804.3	-2.1%

Table J. 3: External temperatures and relative temperature change.

Cartridges Fired	Reload Time: 10 sec							
	T1 0.0508 (m)	T1 Relative Change	T2 0.1016 (m)	T2 Relative Change	T3 0.1397 (m)	T3 Relative Change	T4 0.2794 (m)	T4 Relative Change
30	409.8	0.9%	437.2	0.4%	438.8	-0.2%	391.5	-0.9%
60	496.1	1.2%	546.8	0.8%	542.1	-0.3%	466.2	-0.5%
90	560.3	-1.1%	628.4	-1.1%	614.3	-2.7%	520.2	-1.9%
120	627.9	-1.9%	711.3	-1.7%	688.7	-3.5%	575.6	-2.4%
150	688.3	-2.7%	786.3	-2.3%	756.4	-4.1%	626.0	-2.9%
180	743.2	-3.3%	854.5	-2.8%	817.9	-4.6%	671.3	-3.3%
210	793.9	-3.8%	912.7	-2.7%	874.8	-4.6%	712.6	-3.7%
240	839.0	-4.3%	955.9	-2.6%	920.1	-4.3%	748.9	-4.1%
270	884.4	-4.3%	990.8	-2.4%	958.3	-3.9%	785.9	-4.4%